Surface and Interface Studies of Molecular Heterostructures on Weakly Interacting Substrates

Dissertation

der Mathematisch-Naturwissenschaftlichen Fakultät
der Eberhard Karls Universität Tübingen
zur Erlangung des Grades eines
Doktors der Naturwissenschaften
(Dr. rer. nat.)

vorgelegt von
Qi Wang
aus Shandong, China

Tübingen
2020

Gedruckt mit Genehmigung der Mathematisch-Naturwissenschaftlichen Fakultät
der Eberhard Karls Universität Tübingen.

Tag der mündlichen Qualifikation:	23.10.2020
Stellvertretender Dekan:	Prof. Dr. József Fortágh
1. Berichterstatter:	Prof. Dr. Frank Schreiber
2. Berichterstatter:	PD Dr. Fajun Zhang

ABSTRACT

Organic conjugated molecules have become one of the fundamental materials in the semiconductor community in recent years. Devices made by organic semiconductor (OSC) materials, like organic light emitting diodes (OLED), organic photovoltaic cells (OPV) and organic field effect transistors (OFET), exhibit comparable efficiencies compared with that of inorganic counterparts, moreover with superior properties in terms of light weight, mechanical flexibility and low cost, showing excellent application potential in the commercial market. To further promote the OSC device efficiency, a comprehensive understanding of the heterojunction interfaces comprised by different OSC materials from crystal structure to electronic structure is rather essential, as these inevitable interfaces play a crucial role in the charge carrier transportation process.

In order to obtain the information of the structural property (molecular adsorption height and stacking arrangement) and electronic structure of heterostructures, X-ray standing wave (XSW), low-energy electron diffraction (LEED), high-resolution X-ray photoelectron spectroscopy (HR-XPS) and ultraviolet photoelectron spectroscopy (UPS) are employed in this work. Coinage metals are commonly used as electrodes at applied devices due to their favourable conductivity. For prototypical studies here, atomic clean-coinage metal crystals are used, as their surfaces are flat and ordered, meanwhile the surface chemical activity can change from inert [Au (111)] to active [Cu (111)], which can further affect the coupling strength with the subsequent deposited OSC molecules. In the beginning of this work, copper-hexadecafluorophthalocyanine (F_{16}CuPc)-derived bilayers, with intermediate layers of 5,7,12,14-pentacenetetrone (P4O) and perylene-3,4,9,10-tetracarboxylic diimide (PTCDI), are built on Au(111) to explore the influence of the organic-metal interaction strength. It has been found that the bilayers are well formed and the F_{16}CuPc exhibits an inverted intramolecular distortion compared to its monolayer structure. Secondly, a donor-acceptor (D-A) counterpart, pentacene-perfluoropentacene (PEN-PFP), is taking to further study the bilayer formation on the same substrate. It has been proven, however, that the molecular mixture occurs

despite of the weakly interacting substrate. Finally, a more complicated heterostructure, the trilayer, has been employed on Ag(111), consisting of a zero-net-dipole titanyl-phthalocyanine (TiOPc) bilayer and then a third organic molecular layer (F_{16}CuPc, P4O) adsorbs on top of it. We found that none of the intramolecular distortion or molecular exchange have been observed, implying that an ideal organic-organic interface was formed. By utilizing the powerful XSW, HR-XPS and UPS techniques, we have accessed the electronic and structural information of several heterostructures on the coinage metal substrates, which could inspire or promote more researches on the OSC-based fundamental and application field.

Key words: heterostructure, adsorption property, electronic characteristic, X-ray standing wave, X-ray photoelectron spectroscopy, ultraviolet photoelectron spectroscopy

CONTENTS

Part I

Introduction

1. MOTIVATION AND OUTLINE

1.1 Motivation

In the last decades, organic semiconductors (OSCs) have drawn a great deal of attention from the scientific community as an emerging class of materials for (opto)electronics applications, compared with their inorganic counterparts. OSCs have shown numerous advantages when fabricating electronic devices, such as low cost, light weight, mechanical flexibility and facile large-scale-production [1-7]. Commercial applications of OSCs include organic light emitting diodes (OLED), organic photovoltaic cells (OPV) and organic field effect transistors (OFET) and so on. Besides that, the physical properties of OSC materials can be easily tuned by altering their chemical structure, in order to meet certain requirements of devices during performance optimization [8-11]. Thereof, weak interaction caused by van der Waals force or dipole moment in the OSC-based (opto)electronic devices can be generally observed. However, the devices do have several drawbacks resulting from the weak interaction strength between neighbouring molecules, such as the low crystallinity [12, 13] and low charge-carrier mobility [14, 15], which dramatically affect the injection and extraction properties at heterostructure interfaces, and transportation (inside OSC thin films) processes of charge carriers. Thus, fundamental researches on the electronic structure and crystal structure of the OSC thin films and the OSC-constituted heterojunction interfaces are indispensable to further improve and optimize the performance of OSC-based devices [16-18].

So far, organic-inorganic (Org.-Inorg.) heterojunction interfaces, especially organic molecules on metal electrodes, have been well studied and characterized by employing surface-sensitive probing techniques [19-22]. However, inside devices (OLED or OPV), the interfaces between organic and organic semiconductors are also quite common to be seen [23-25]. The energetic levels at the interface will definitely influence the extraction/injection and recombination/separation processes of charge carriers. Furthermore, it has also been reported that, in the bilayer structures, the latter deposited organic molecules can push out the former deposited

organic monolayer and directly attach to the metal electrode due to the stronger coupling strength between the latter molecules and the metal electrode compared with that of the former molecules [26-29]. This means the bottom metal substrate can still affect the subsequent deposited second organic molecular layer, making more complicated to understand the properties of the interface and to control/tune them. Thus, in order to get a clear understanding of Org.-Inorg. systems and organic-organic (Org.-Org.) systems (organic molecular heterostructure), both the electronic property and structural information should be comprehensively investigated. Such fundamental understanding will help to provide guidelines to select the proper organic semiconductor combinations to form a well-ordered interface and match the corresponding energy levels that can decrease the injection or transport barriers of charge carriers in a controllable manner, which will eventually benefit the development and optimization of OSC-based devices.

1.2 Outline

In this work, several prototypical OSCs have been deposited on coinage metal substrates. Such heterostructures represent model systems commonly present inside the real devices. The main purpose is to investigate the electronic properties and the structural information of molecular heterostructures. The specific adsorption distances (d_H), energy level alignment (ELA), possible charge transfer (CT), molecule dipole moment of these heterostructures prepared under the ultra-high vacuum (UHV) condition have been studied. Angle-resolved ultraviolet photoelectron spectroscopy (ARUPS), X-ray photoelectron spectroscopy (XPS), normal-incidence X-ray standing wave (NIXSW) and low-energy electron diffraction (LEED) are mainly used as probing techniques.

In Chapter 2, a brief introduction of concepts in OSCs related to the surface and interface properties is presented, i.e., electronic structure, energy levels, a standard indicator to predict possible molecular exchange and basic information about the organic molecules and coinage crystal substrates used in this thesis.

In Chapter 3, an introduction of experimental techniques is given. By performing ARUPS, we can obtain valence band properties, work function and

ionization energy at the surface. From XPS, we can obtain the information about the chemical compositions, chemical states and possible chemical shifts of the probed sample. By employing the XSW technique, precise information about the adsorption distance of the constituting atoms in the molecule can be determined and possible bending of the molecular backbone or functional group can be identified. Moreover, LEED can provide information about the crystal structure of the sample surface covered by organic molecules. With the combination of all techniques, a three dimensional (3D) picture of the bilayer and trilayer systems studied here can be obtained. In the last, an entire introduction of different π-conjugated organic materials and metal single crystals used in this work is provided, includes the standard parameters to investigate the molecular properties.

In Chapter 4, by exploring the influence of the organic-metal interaction strength in bilayer systems, we determine the molecular arrangement in the physisorptive regime for copper-hexadecafluorophthalocyanine (F_{16}CuPc) on Au(111) with intermediate layers of 5,7,12,14-pentacenetetrone (P4O) and perylene-3,4,9,10-tetracarboxylic diimide (PTCDI). By using UPS, XPS, LEED and XSW techniques, it shows that these two bilayers are well-ordered and follow the original deposition sequence. Surprisingly, F_{16}CuPc as the second layer within the heterostructures exhibits an inverted intramolecular distortion compared to its monolayer structure.

In Chapter 5, we present a comprehensive study on the properties of the donor-acceptor (D-A) bilayer structures using the above-mentioned techniques. Accordingly, a donor material-pentacene (PEN) and an acceptor material-perfluoropentacene (PFP) are chosen to build bilayer structures. PFP/PEN bilayers have been grown on Au(111) substrates with different deposition orders, i.e., PFP on PEN layer and PEN on PFP layer, respectively. By comparing the adsorption behavior of PEN and its perfluorinated counterpart, we find that: i) on Au(111), the first layer (whether PEN or PFP) is physisorbed, ii) the final bilayer structure is almost independent from the deposition sequence and iii) in both cases a mixed bilayer is formed.

In Chapter 6, in order to avoid the possible molecular exchange or mixture reactions in molecular bilayers as they have been observed on the chemically active

Ag(111) surface as well as on the weakly interacting substrate Au(111), we employ a more elaborate method by growing **0** net dipole titanyl-phthalocyanine (TiOPc) bilayers on Ag(111). Further deposition of the third molecular layer (F_{16}CuPc or P4O) on the dipole bilayer has shown a non-interaction behavior of the third molecular layer on the chemisorptive substrate.

Finally, Chapter 7 summarizes the whole work and gives an outlook on the future work based on the current results.

2. FUNDAMENTALS

2.1 Surface and Interface Properties

In recent years, organic optoelectronics has drawn increasing research attentions. Inside these organic optoelectronic devices, their interface properties are of crucial, which is the fundamental knowledge that needs to be studied and discovered in order to improve the device performances. Thus, interface studies between organic materials and metal crystals, or organic and organic materials, are of comprehensive interests [22, 30-35].

The work function (WF or Φ), electron affinity (EA), ionization energy (IE), and adsorption distances (d_H) are considered as the parameters to describe the interface between two solids [36-39], especially in this work. The following parts will give a basic introduction of some concepts related to solid surfaces and interfaces.

2.1.1 Molecular Electronic Structures and Energy Levels

For a finite sample, its vacuum level (VL, $E_{vac}[s]$), see Fig. 2.1(a), is defined as the electron energy of the solid-state element surfaces. However, during the measurement of work function (WF or Φ), the vacuum level is defined as the energy of electrons moving outside the surface of a solid [40-43]. For metals, it is a distance that is out of the effect by mirror force [44], where the mirror force is zero. The vacuum level, as a property of surfaces, depends on the electronic structures formed by the electron dipoles in the outer layer of the atoms.

For an infinite sample, the vacuum level (VL, $E_{vac}[\infty]$), see Fig. 2.1(a), is defined as the energy of an electron located at infinite distance from the surface, which also implies that such energy is constant. However, this situation represents an ideal condition and cannot be measured in reality [40, 45].

For an electrical system under thermodynamic equilibrium condition, the Fermi level (E_F) of the whole system is constant throughout the sample and is usually taken as the reference level for other energetic levels.

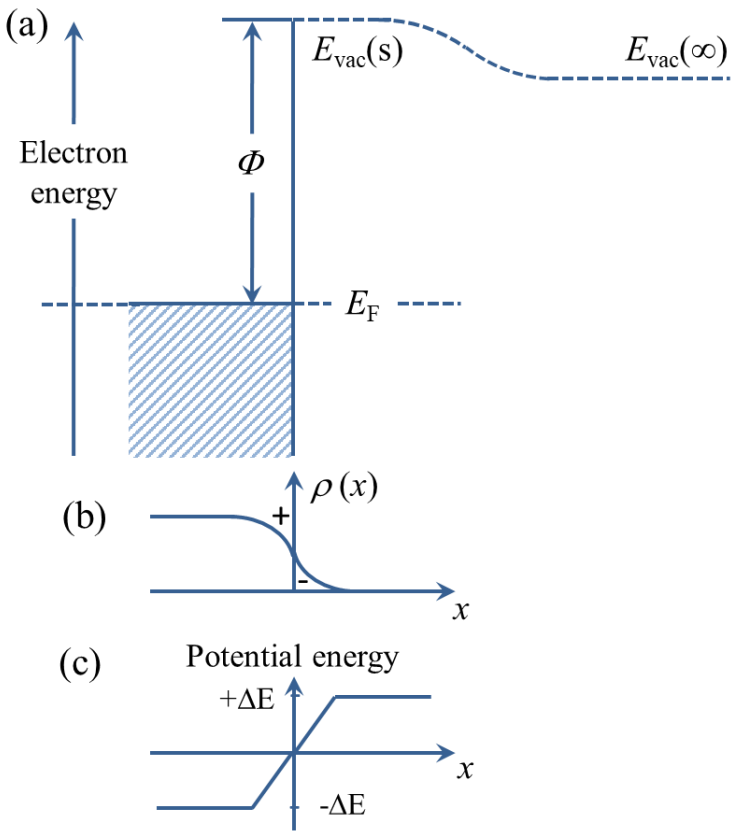

Figure 2.1: (a) Solid surface vacuum level (E_{vac}), work function (WF or Φ) and vacuum level at infinite distance [$E_{vac}(\infty)$]; (b) electron density; (c) electron potential energy, 2ΔE as determined from interface dipole. In the figures, x-axis indicates the perpendicular direction to the sample surface. Figure adapted from Ref. [40].

The energy difference between the vacuum level and the Fermi level is defined as the work function (WF, Φ). For an atomically clean metal, due to the spilling out of the electrons from the surface, the vacuum level will slightly increase resulting from the induced surface dipole where the negative charges stay outside of the metal surface, leaving positive charges inside (Fig. 2.1b). When an electron crosses through the surface dipole and leaves the solid (metal), the barrier will be increased by the same amount of static dipole (Fig. 2.1c). When the electron is far away from the surface and in an infinite distance, its potential will decrease, as shown in Fig. 2.1(a).

By performing UPS measurements (Fig. 2.2), the work function (Φ) can be obtained by measuring the secondary electron cut-off (SECO) spectra on the surface

of a metal sample. SECO (to determine the vacuum level) is measured in normal emission with a biased potential of a known value, which is always – 3 V in this work. As the photo energy ($h\upsilon$) of the incoming ultraviolet radiation is known and the kinetic energy of the photoelectrons is detected by the analyzer, the WF (Φ) of the solid sample can be calculated by the following formula:

$$\Phi = \mathrm{E_K^{min}} + h\upsilon - \mathrm{E_K^{max}} \text{ [40]}$$

where $\mathrm{E_K^{min}}$ is the minimum of the photoemission energy and $\mathrm{E_K^{max}}$ is the maximum of photoemission energy, as shown in Fig. 2.2.

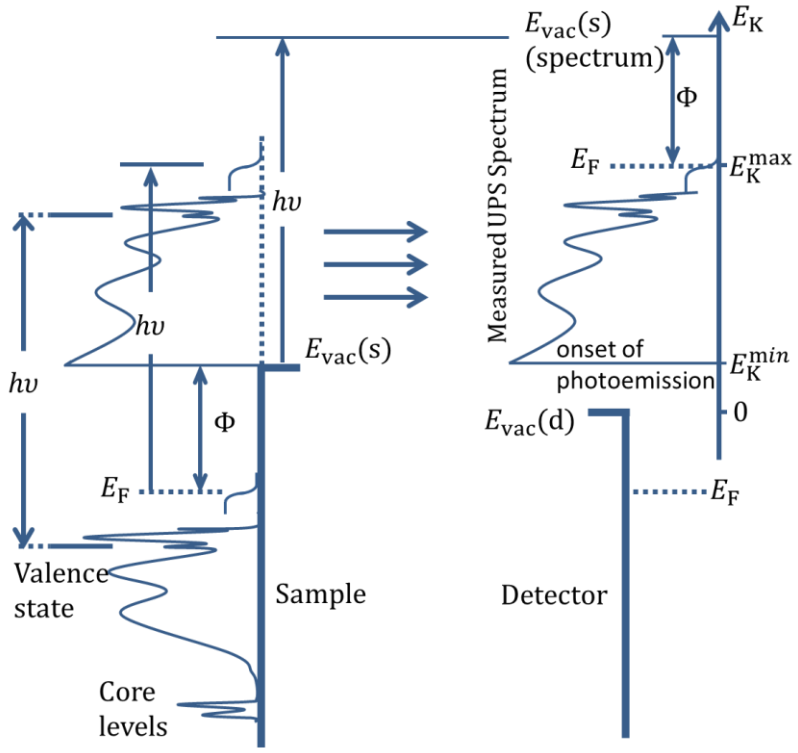

Figure 2.2: Photoelectric effect and UPS spectra of a metal surface. Lower left: valence band and core-levels, solid vacuum level and Fermi-level. Upper left and right: kinetic energy (E_K) of the photoemission electrons detected by the analyzer. This figure is adapted from Ref. [40].

2.1.2 Energy Level Alignment

The energy level alignment at the interface is displayed in Fig. 2.3. When the metal and organic molecule (Org. in Fig. 2.3) are far away from each other, their vacuum levels are aligned with the $E_{vac}[\infty]$ (Fig. 2.3a). When they are contacted, Fermi levels of the metal and organic solid are aligned, and an interface dipole is

formed with a very thin energy-offset at the interface between them (Fig. 2.3b) [46]. Fig. 2.3(c) and (d) are usually used as simplified models for Fig. 2.3(a) and (b) to represent an energy level diagram at interfaces. In Fig. 2.3(c, d), HOMO is abbreviation for the highest occupied molecular orbitals and LUMO for the lowest unoccupied molecular orbitals. Φ_m is the work function of the metal, EIB and HIB are referred to the electron and hole injection barriers, E_g is the band gap. IE represents the ionization energy and EA the electron affinity [47, 48].

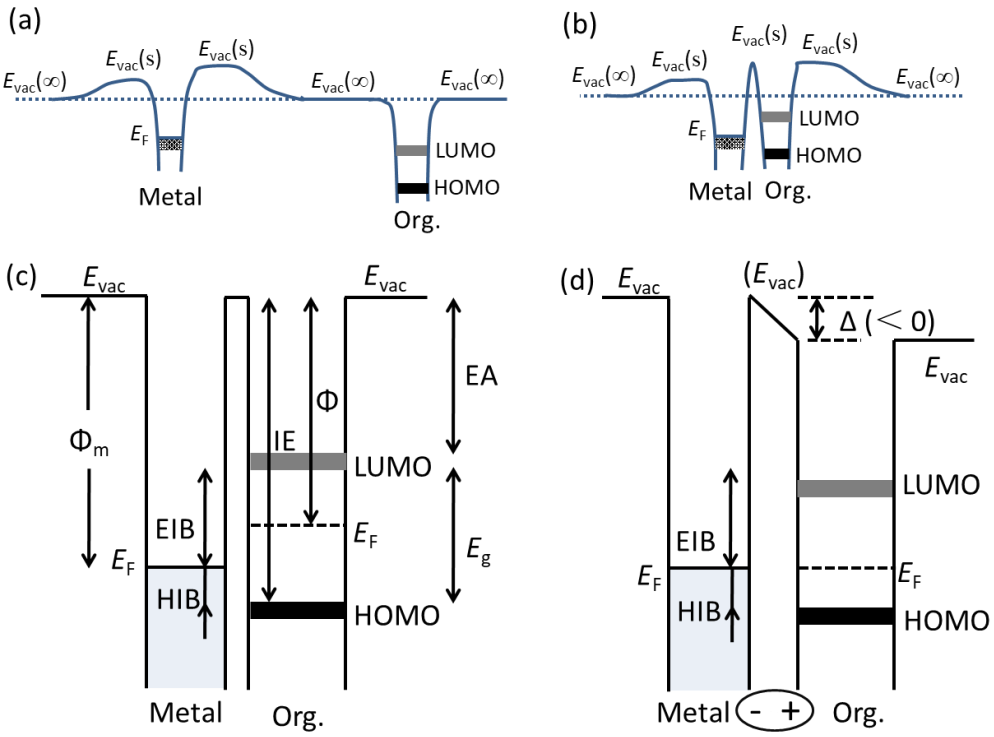

Figure 2.3: (a) The interface electronic structure of a metal and an organic solid at an infinite distance. (b) The contact layer between metal and organic thin film. (c) The energy level diagram of the metal and an organic solid at an infinite distance. (d) The energy level diagram between the metal and an organic solid in proximity of the contact layer. Based on Ref. [46].

The electronic structure at the interface can be determined by growing thin films in an ultra-high vacuum chamber (around 5×10^{-9} mbar) [49-52]. Nevertheless, the limitation of photoelectron mean free path (see Chapter 3) by surface sensitive techniques only allows to measure monolayer or few layers of thin films on the substrate, less works have been carried out to study thicker organic films [26, 53-56].

2.1.3 Interface Dipole

Here we discuss the information of the interface dipole, which is a fundamental concept when discussing interfaces between metals and conjugated organic materials (COMs)/OSCs. The different mechanisms of an interface dipole are shown below:

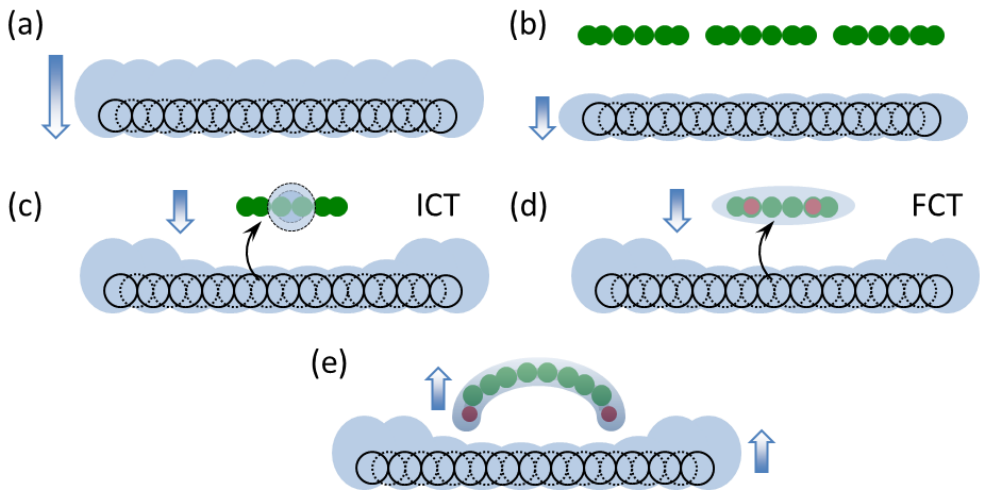

Figure 2.4: Different formation mechanisms of interface dipoles. Figure based on Ref. [39].

There are mainly three regimes of interface dipole, as schematically shown in Fig. 2.4(a-e). For the first case, the interface dipole is caused by the push-back effect due to the Pauli repulsion between the electrons of the adsorbate and the metal [37]. Without contacting, in Fig. 2.4(a), the free electrons spilling out of a clean metal surface give rise to a surface dipole. With COMs contacting on the metal substrate, the electrons of the metal are "pushed back" closer to the surface and thus the surface dipole is weakened as depicted in Fig. 2.4(b). These phenomena can be observed, e.g. in weakly interacting systems, such as organic molecules on the Au substrate (Chapter 4 and Chapter 5) [26].

The second mechanism resulting in an interface dipole is charge transfer (CT), shown in Fig. 2.4(c, d), where the integer or fractional charge transfer (ICT, FCT, respectively) are depicted. Electrons are transferred from the substrate to the conduction band minimum (CBM) (or LUMO) of the adsorbate. FCT is usually

related to chemical bond formation, while ICT can occur for weakly interacting systems leading to the Fermi level pinning [57, 58].

The last mechanism is the chemical interaction between the adsorbate and the substrate, instead of the charge transfer (Fig. 2.4e). There exist multiple interactions at the interface along with the formation of new chemical bonds. This kind of chemical interaction is well known as in the case of CO or benzene rings on clean metal surfaces.

Note that these mentioned cases are overall nonpolar molecules. For polar organic molecules, i.e. molecules with a net dipole moment, they form interface dipoles on the surface parallel to the direction of the molecular dipole moment (Fig. 2.4e).

2.2 Indicators for Molecular Interaction Strength

Organic heterostructures are a central part of a manifold of (opto-)electronic devices and serve a variety of functions. Particularly molecular monolayers on metal electrodes are of paramount importance for device performance as they allow tuning energy levels in a versatile way. However, this can be hampered by molecular exchange, i.e., by interlayer diffusion of molecules towards the metal surface. Since the arrangement in organic heterostructures is of utmost importance for controlling the performance of organic (opto-)electronic devices, prediction of possible molecular exchange for a conjugated organic materials-pair on an inorganic substrate is indispensable for rational device design. However, even for model systems molecular exchange mechanisms are not fully understood. Accordingly, the concepts related to different indicators for the mechanism of molecular exchange will be introduced in the following, with the comparison of different COMs.

2.2.1 Introduction of Indicators

The energy-level alignment (ELA) between active COMs and metal electrodes is of paramount importance for charge transport across the metal-organic interface and thus represents an eminent factor for the efficiency of organic (opto-)electronic devices [59, 60]. Template layers between the metal contact and the active material have proven to be an efficient way for engineering interface energetics and tuning

energy barriers for charge injection/withdrawal [61, 62]. However, molecular diffusion can be a serious issue in the actual arrangement within the bilayer if it does not reflect the deposition sequence [63-65]. In particular, for weak coupling at an organic-metal interface, subsequently deposited COMs can diffuse through the template layer to the metal surface [27, 63, 66-68], making the template layer obsolete. Whether such molecular exchange takes place or not is, moreover, also a fundamental scientific interest, which is, even for bilayer model systems, not yet understood [67-74].

Although there are a plethora of studies about organic/organic heterostructures on clean metal surfaces focusing on bimolecular monolayers [31, 75-78], only few studies focus on bilayers [27, 67-69, 71, 72, 79, 80], where the bilayers of copper-phthalocyanine (CuPc) and 3,4,9,10-perylene-tetracarboxylic-dianhydride (PTCDA) on Ag(111) served as a model system [27, 71, 72, 79, 80]. For the deposition of PTCDA on a closed layer of CuPc on Ag(111), molecular exchange takes place and PTCDA reaches the Ag(111) surface [27], whereas for the inverse system, *i.e.,* CuPc on PTCDA, the initial bilayer arrangement is maintained [71, 72]. As expected, the coupling of CuPc with Ag(111) is relatively weak [81, 82], whereas PTCDA is comparatively strongly coupled to the same substrate [83-85]. Going beyond this model system, we show the concept that the organic-metal interaction strength is indeed a decisive factor for the sequential arrangement in organic heterostructures.

Interfacial "interaction strength" has been well defined and reproducible from a theoretical viewpoint [86-89]. However, reliable computation of adsorption energies of COMs on surfaces involves an advanced level of theory and still requires experimental input, *e.g.*, surface unit cells [88, 90]. Therefore, the indicators for organic-metal interacting strength have been developed experimentally based on:

1) vacuum-level shifts (ΔVL),
2) binding energy (BE) shifts of:
    i. valence electron features (ΔHOMO),
    ii. core-levels of aromatic carbon atoms (ΔC_{π}),
    iii. core-levels of carbon atoms in functional groups (ΔC_{funct}),
3) averaged adsorption distances (d_H).

Indicators #1 and #2 can be accessed by widely-used photoelectron spectroscopy (UPS and XPS) techniques and Indicator #3 can be accessed by means of the XSW technique [91, 92]. Importantly, while it is difficult to prove the absolute generality of these indicators, the next section shows that most of these indicators are consistent for the cases considered.

2.2.2 Application by Indicators

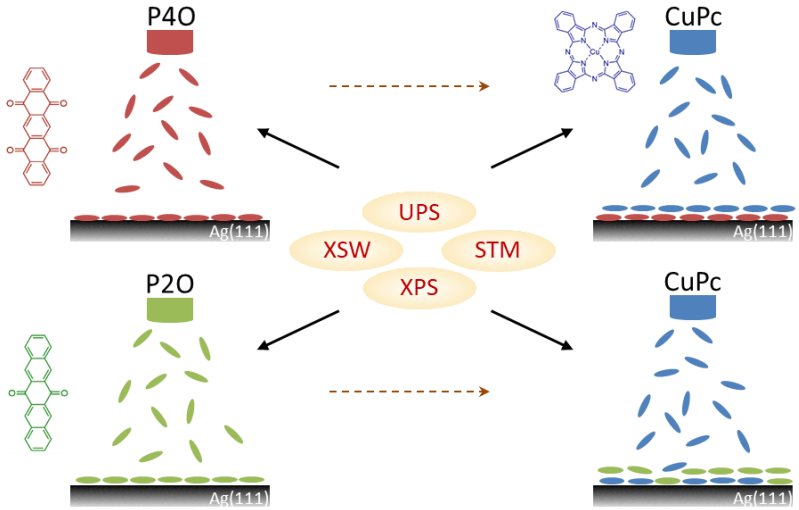

Figure 2.5: A sketch of the samples studied by UPS, XPS, XSW and STM, whereas the multilayer PxO (x=2, 4) is grown on Ag(111) and a low-temperature desorption is processed to form a well-ordered monolayer. CuPc is deposited in the following. This figure is taken from Ref. [26].

The organic-metal interaction strength is the result of various competing effects such as van der Waals interactions, charge transfer or Pauli repulsion principle, and a broad range of scenarios has been reported in a number of detailed studies over the last decades [31, 87, 88, 93-96]. As a striking example for the subtle competition of interaction strength between molecules and the substrate, 6,13-pentacenequinone (P2O) and 5,7,12,14-pentacenetetrone (P4O) (Fig. 2.5) have been identified [97]. Both COMs are physisorbed on Au(111) with a planar adsorption geometry and comparably large adsorption distances. In contrast, on Cu(111) they are chemisorbed involving a net electron transfer from the substrate to the adsorbate resulting in a (partially) filled former LUMO. The core-levels of the monolayer show strong chemical shifts and the molecules adsorb in a bent

conformation with short bonding distances. Ag(111) as a substrate provides an intermediate case, and by simply adding two more oxygen atoms to the molecular structure, the interaction can be changed from physisorption (P2O) to chemisorption (P4O) [97].

To determine the indicators by studying the arrangement, P2O and P4O have been chosen since a subtle change in chemical structure has a paramount effect on interfacial coupling with Ag(111). Moreover, copper-phthalocyanine (CuPc) has been applied as the following layer to further indicate the adsorption strength among them. As a result, subsequently deposited CuPc diffuses through P2O monolayers but forms bilayer structures on P4O evidenced by STM and XSW experiments, which shows that organic-inorganic coupling is crucial for molecular exchange and that organic-organic coupling plays a minor role in this context. The investigation progress has been systematically summarized in Fig. 2.5.

The indicators are then quantified (Fig. 2.6) to explain the mentioned phenomenon, *i.e.,* binding energy shifts determined by UPS or XPS, which can reliably predict molecular exchange of a COM-pair on a specific substrate. Adsorption distance of each element is determined by XSW, in order to further demonstrate the ability of the indicator to predict adsorption strength. Quantification of the coupling strength based on XPS and UPS experiments would be an important step to simply and reliably predict the energy-level alignment at organic-metal interfaces.

Fig. 2.6 shows the five indicators for organic-metal interaction strength. In addition to the indicators for the interaction of CuPc and PxO with Ag(111), also the values for PTCDA taken from Ref. [84, 85, 98, 99] and d_H of CuPc taken from Ref. [100] are included for comparison. Almost all these values show the same trend in the interaction strength with Ag(111) which increases following the order P2O, CuPc, PTCDA, P4O. This serial order confirms that the rearrangement in the measured bilayers is indeed determined by the coupling of the first monolayer with the substrate. As detailed below, all of these five indicators are the result of various, partially competing, effects and their consistency is thus remarkable.

Concerning the first indicator, ΔVL, it is noteworthy that for none of the COMs the vacuum-level increases upon monolayer formation, which could be expected, as

in all cases the LUMO becomes (partially) filled for the monolayers on Ag(111) [84, 85, 97]. However, ΔVL is the result of many competing effects and without advanced theoretical modeling it is impossible to say, whether the expected VL increase is mainly compensated by the push-back effect, back donation [93, 101] of charges or distortion induced intramolecular dipoles [102].

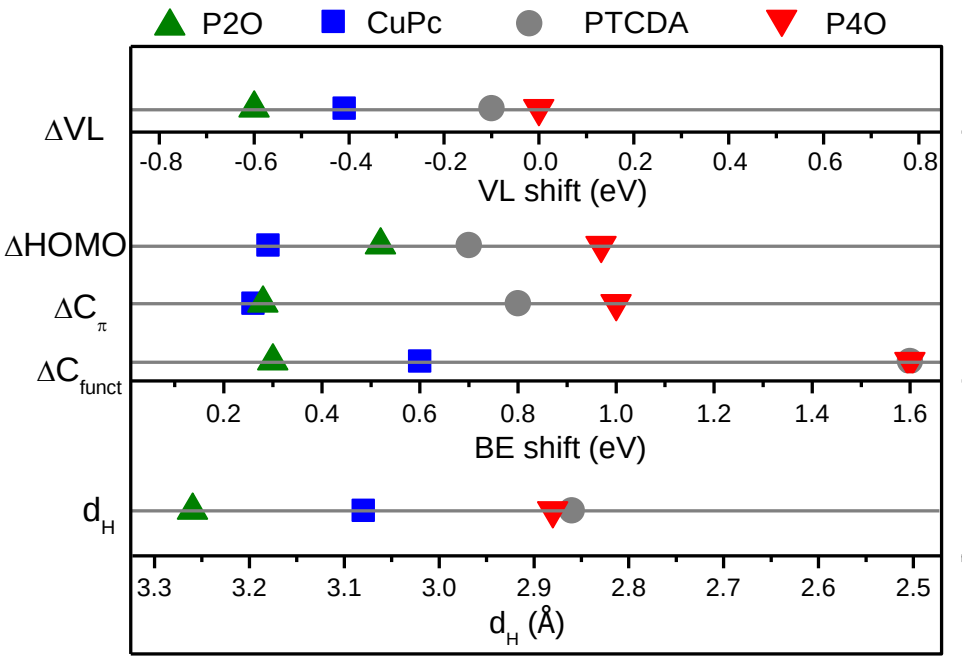

Figure 2.6: Vacuum-level shift (ΔVL) between clean Ag(111) and a monolayer of the respective COMs. Binding energy shift between monolayer and multilayer of the HOMO-maximum (ΔHOMO) and the C 1s peak of the molecular backbone (ΔC_{π}) and the functional group (ΔC_{funct}) of the respective COMs on Ag(111). Averaged bonding distance (d_H) of the carbon atoms in the molecular core in sub-monolayers on Ag(111). The figure is taken from Ref. [26].

Considering the core-level shifts, it is reasonable that the shift of the aromatic carbons' C 1s signal (ΔC_{π}) is similar to that of the HOMO as for all four COMs the HOMO is relatively delocalized over the whole molecule. The widest range (1.6 eV) in BE shifts can be found for the C 1s signals of carbon atoms in functional groups, i.e., C=O or C-N (ΔC_{funct}). This is, on the one hand, not surprising as for hydrocarbon systems since charge transfer is often mediated by functional groups or heteroatoms [97, 103]. We note that the functionality of the heteroatoms is distinctly different for PxO, CuPc and PTCDA and it is not straightforward that also ΔC_{funct} follows the

general trend. The same holds for d_H as averaged bonding distances (and even possible molecular distortions) alone are no clear indication for bonding strength [94, 104, 105]. For example, it was shown that additional bulky side-groups increase the averaged carbon bonding distance of a pyrene-derivative on Ag(111) without notable changes in the interaction strength as measured by UPS and XPS [94]. Moreover, it is only useful to compare bonding distance of different COMs on the same surface.

Overall, the core-level shifts (ΔC_π and ΔC_{funct}, determined by XPS) are the most reliable indicators for organic-metal coupling strength. They have the advantage that, in contrast to d_H, no complex synchrotron-based measurements are necessary to access them. This applies likewise for valence electron spectra. However, the complex relation of thin film structure and electronic structure even for weakly interacting systems does not allow to precisely estimate the coupling strength based on single parameters (ΔVL or ΔHOMO). For the considered systems, the indicators predict the sequential arrangement in heterostructures correctly. It is also noted that other factors such as the particular molecular weight or shape ("bulkiness") may also trigger the molecular exchange [106, 107], besides the organic-metal interaction strength.

2.3 Materials

In this section, the basic information of the organic molecules as well as the coinage metal substrates used in this thesis are introduced.

2.3.1 Organic Compounds

Figure 2.7 summarizes the chemical structure of organic molecules presented in this work. These molecules usually exhibit a planar structure in the gas phase and have a well-ordered arrangement when deposited on an atomically clean single crystal metal surface.

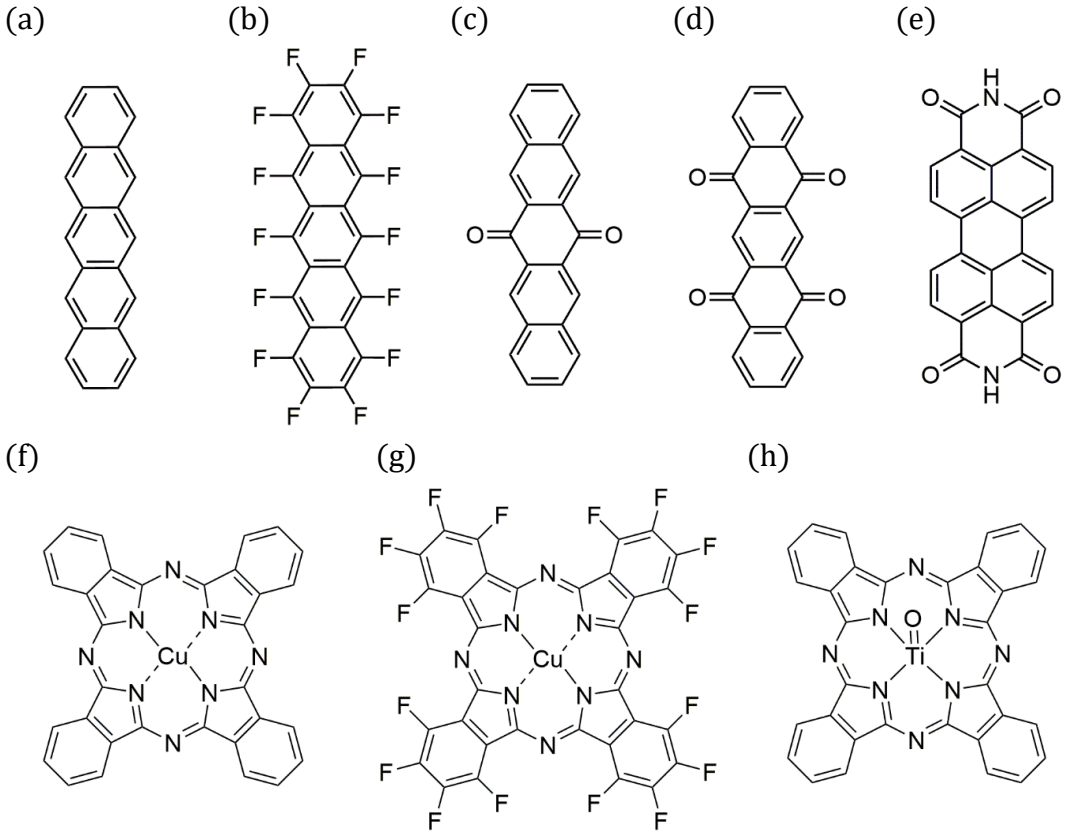

Figure 2.7: Organic compounds used in this work. (a) Pentacene (PEN), (b) Perfluoropentacene (PFP), (c) 6,13-pentacenequinone (P2O), (d) 5,7,12,14-pentacenetetrone (P4O), (e) Perylene-3,4,9,10-tetracarboxylic diimide (PTCDI), (f) Copper-phthalocyanine (CuPc), (g) Copper-hexadecafluorophthalocyanine (F_{16}CuPc), (h) Titanyl-phthalocyanine (TiOPc).

The chemical formula, donor or acceptor type, optical gap, and transport gap are given in below.

(a) Pentacene (PEN)

Formula: $C_{22}H_{14}$
Character: donor
Optical gap: 1.7 eV [108]
Transport gap: 2.4 eV [108]

(b) Perfluoropentacene (PFP)

Formula: $C_{22}F_{14}$
Character: acceptor
Optical gap: 1.94 eV [109]
Transport gap: 1.95 eV [110]

(c) 6,13-pentacenequinone (P2O)

Formula: $C_{22}H_{12}O_2$
Character: acceptor
Optical gap: 2.8 eV [111]
Transport gap: 2.8 eV [112]

(d) 5,7,12,14-pentacenetetrone (P4O)

Formula: $C_{22}H_{10}O_4$ Optical gap: not found/measured
Character: acceptor Transport gap: not found/measured

(e) Perylene-3,4,9,10-tetracarboxylic diimide (PTCDI)

Formula: $C_{24}H_{10}O_4N_2$ Optical gap: 2.17 eV [113]
Character: acceptor Transport gap: 2.37 eV [113]

(f) Copper-phthalocyanine (CuPc)

Formula: $C_{32}H_{16}N_8Cu$ Optical gap: 1.7 eV [113]
Character: donor Transport gap: 2.2 eV [113]

(g) Copper-hexadecafluorophthalocyanine (F_{16}CuPc)

Formula: $C_{32}F_{16}N_8Cu$ Optical gap: 1.5 eV [114]
Character: acceptor Transport gap: 1.93 eV [115]

(h) Titanyl-phthalocyanine (TiOPc)

Formula: $C_{32}H_{16}N_8OTi$ Optical gap: 1.4 eV [116]
Character: donor Transport gap: 1.7 eV [117]

2.3.2 Coinage Single Crystals

In our study, Au(111), Ag(111) and Cu(111) single crystals are chosen as the deposition substrate for organic molecules, because they have a well-ordered and smooth surface [84, 118-120]. Moreover, these metal are also commonly employed as the grid electrodes for the (opto)electronic devices [121, 122].

The electronic properties characterized by photoelectron spectroscopy (UPS and XPS) are displayed in Fig. 2.8(a, b, c) and (d, e, f), respectively. The UPS and XPS spectra of an atomically clean Au(111) substrate, which is obtained by several sputtering-annealing circles inside in UHV conditions, are shown by the top orange curves. In Fig. 2.8(a), there are several peaks located at binding energy between 2 eV to 8 eV attributed to d-band structures of Au. In this spectrum, the secondary electron cut-off can be clearly seen, which is near the binding energy of 16 eV. In this case, the work function of Au(111) can be directly determined as 5.2 eV. However, as the work function of the sample is not always larger than the work function of the electron analyzer, a biased voltage of the substrate is needed to let the low kinetic energy photoelectron overcome this energy barrier and be detected. From the XPS

spectra, different characteristic peaks of Au are displayed (Fig. 2.8d). Among all the peaks, the Au 4f is most intense and is always taken as a reference peak to calibrate the binding energy corresponding to other peaks. The fine structure of Au 4f core-level spectra is shown in Fig. 2.9(a). Au 4f peak splits into two peaks, known as Au $4f_{7/2}$ and Au $4f_{5/2}$, which are located at the BE of 84 eV and 88 eV, respectively. For Ag(111) single crystal, in Fig. 2.8(b), the UPS survey spectra shows again d-band features in the binding energy between 4 eV and 8 eV and the XPS full spectra provides characteristic peaks of Ag 3d and Ag 3p. The most intense peak, Ag 3d is shown in Fig. 2.9(b), and it is splitting in $3d_{5/2}$ and $3d_{3/2}$, centered at the BE of 368 eV and 384 eV, respectively. For the UPS spectra of Cu(111) (Fig. 2.8c), the copper d-band appears in the energy rough between 2 eV to 6 eV. A fine structure of the highest intensity peaks is demonstrated in Fig. 2.9(c). Cu $2p_{3/2}$ and Cu $2p_{1/2}$ appear at the BE of 933 eV and 953 eV, respectively. As it is known, the above mentioned peak splittings arise from spin-orbit coupling effects [123, 124].

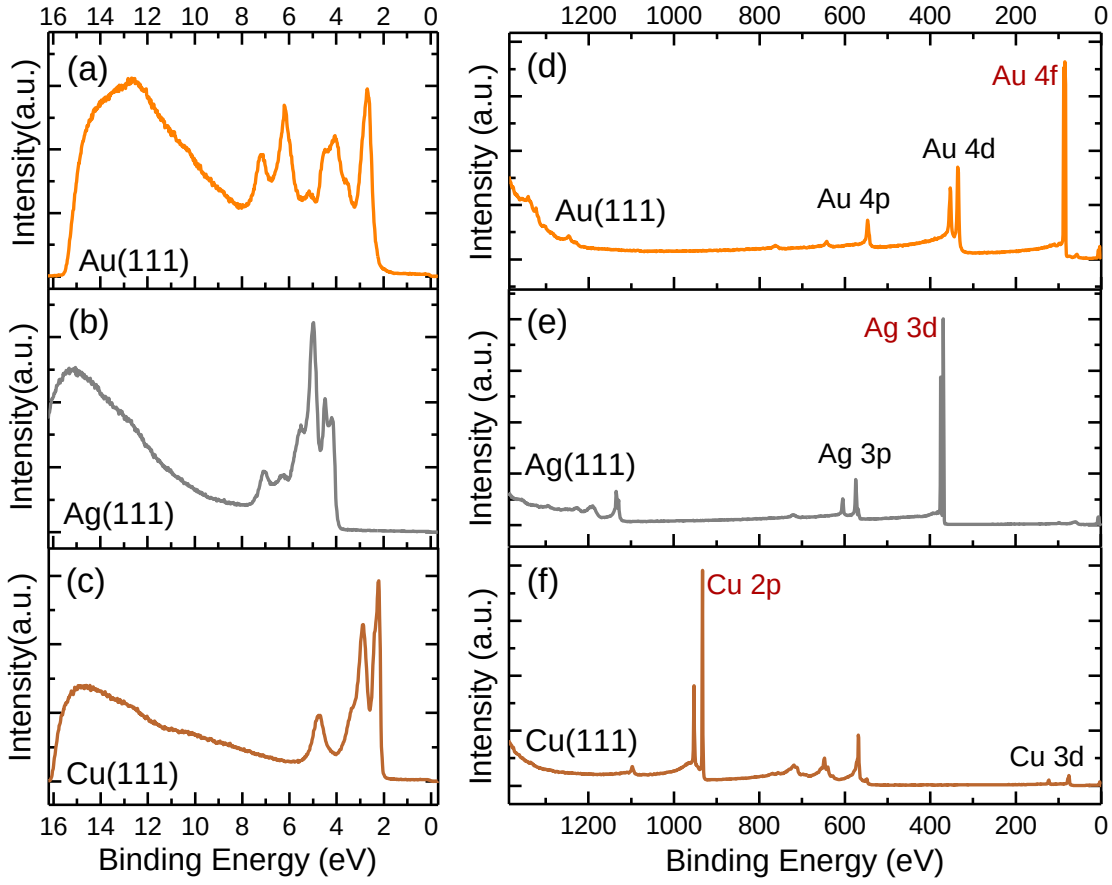

Figure 2.8: Photoelectron spectroscopy spectra in determining the properties of coinage metal crystal substrate.

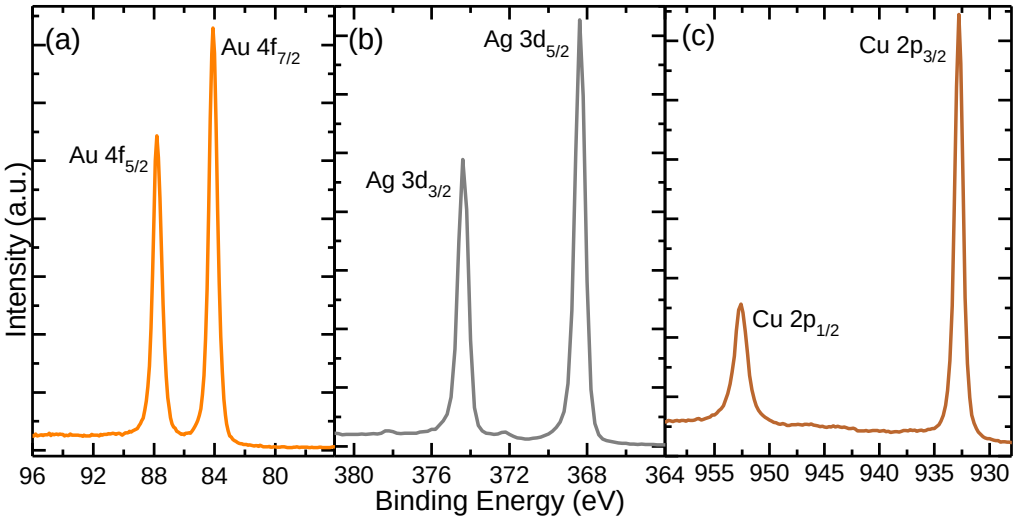

Figure 2.9: High resolution photoelectron spectroscopy spectra of Au $4f_{7/2}$, Au $4f_{5/2}$ (a), Ag $3d_{5/2}$, Ag $3d_{3/2}$ (b) and Cu $2p_{3/2}$, Cu $2p_{1/2}$ (c).

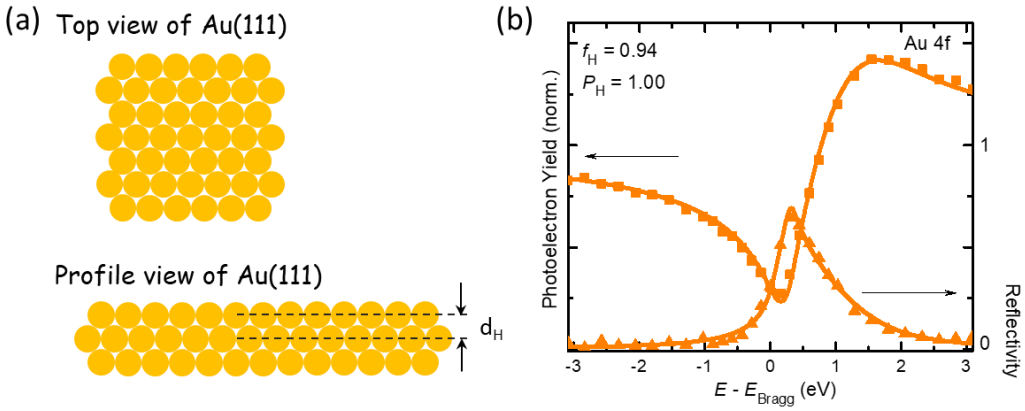

Figure 2.10: A sketch of Au(111) lattice structures of top view and profile view (a). XSW measurements, obtained in I09 beamline in DLS, on the Au(111) clean surfaces of the coinage metals along **H** = [111] (b).

The XSW scan of clean Au(111) single crystals is performed, in I09 beamline in DLS (Fig. 2.10). A brief sketch of Au(111) top view and profile view shows the surface structure (Fig. 2.10a). In Fig. 2.10(b), the reflectivity curve recorded during an XSW scan is plotted together with the photoelectron yield (Y_P), which is generated by a set of XPS scans at different photon energies close to the Bragg energy of Au (2.63 keV) (details see Section 3.2.3).

Based on the equation (3.8, 3.9), two parameters (f_H and P_H), showing the element information, can be accessed. As expected for a well-ordered single crystal, f_H shows a value near one, which proves that the Au substrate holds a high vertical order.

The LEED patterns of the single crystals have been exhibited in Fig. 2.11. The cleaned substrates show pronounced diffraction patterns stemming from the metal atoms. The three surface unit cells (parameters in Tab. 2.1) are hexagonal.

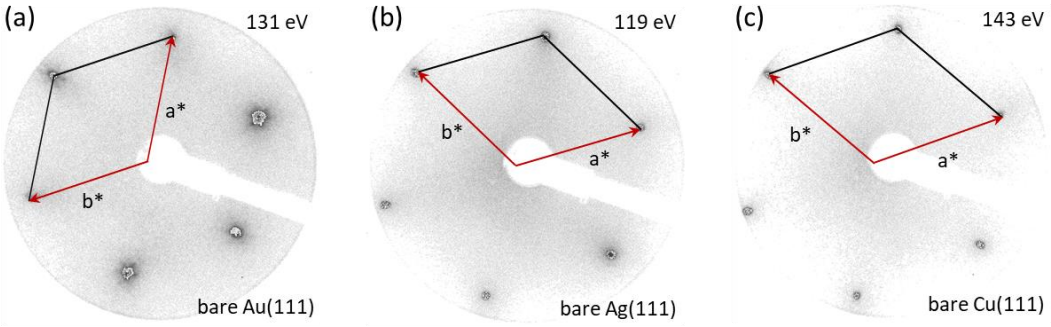

Figure 2.11: LEED patterns of clean metal substrates of (a) Au(111), (b) Ag(111) and (c) Cu(111). The structure of the unit cell in reciprocal space is superimposed in each LEED pattern while red arrows indicate the basic unit. The beam energy is included.

Table 2.1: Relevant parameters of Au(111), Ag(111) and Cu(111), with surface properties characterized by UPS, XPS, XSW and LEED.

	UPS	XPS		XSW		LEED		
						unit cell constant		
	WF/eV	characteristic peak/eV		lattice spacing/Å	Bragg energy/eV	a/Å	b/Å	angle/°
Au(111)	5.53	$4f_{5/2}$: 88	$4f_{7/2}$: 84	2.353	2634	2.86	2.91	118.5
Ag(111)	4.64	$3d_{3/2}$: 374	$3d_{5/2}$: 368	2.357	2630	2.83	2.91	121.0
Cu(111)	4.98	$2p_{1/2}$: 953	$2p_{3/2}$: 933	2.086	2972	2.56	2.54	119.4

Finally, all the parameters of Au(111), Ag(111) and Cu(111), determined by UPS, XPS, XSW and LEED techniques, have been listed in Tab. 2.1. They are always taken as the basic parameters to analyze the electronic structure and structural information of the subsequent formed heterostructures when organic molecules are deposited.

3. EXPERIMENTAL METHODS AND TECHNIQUES

The elementary knowledge to study and understand the experimental methods and techniques are essential to assure our research being carried out reliably. In the beginning, we present the preparation of the samples, which is overall the *in-situ* process in this thesis. Therefore, all the following methods and techniques are under ultra-high vacuum (UHV) conditions. For more details related to the UHV system, the reader is referred to Refs. [125, 126]. Afterwards, this chapter will introduce the versatile experimental techniques related to the research accomplished in this thesis, as well as the data analysis process.

3.1 Sample Preparation

To study the properties of organic semiconductor (OSC) materials, especially electronic characterizations, it is necessary to avoid any contamination of the materials and the substrate. Due to this reason, a particular cleaning procedure and deposition methods have to be used.

3.1.1 Substrate Cleaning and Preparation

Under the UHV system, the substrates, mainly coinage metal single crystals in this work, have been cleaned by sputtering and annealing cycles to reach well-ordered and residue free conditions [127, 128].

The annealing process is carried out by applying the current to a resistive heating system, which is built on the sample manipulator. With an almost non-resistance connection, the input voltage and current are linearly correlated. To be more precise, the thermal controller always has two modes to control the output, called “CV” and “CC” mode. For “CV” mode, a current maximum is fixed and automatically increased with the increasing of voltage, for “CC” mode, the vice versa. In our case, the “CC” mode is chosen. To ascertain the cleaning degree, the gold single crystal is always heated up to 550 ℃ (520 ℃ for silver), which is maintained for ~30 min. By such annealing process, most of the organic molecules and contaminations

can be removed, however, stronger interactions between contamination and substrate require more intense methods. Therefore, it comes to the sputtering process. In the UHV system, a stream of Ar gas is let in the chamber, and then ionized by high voltage, subsequently the Ar^+ ion is accelerated and hits onto the sample, destroying residuals and contaminations. Maintaining that method for approximately 30 min under 5 μA the drain current is more efficient to break chemical bonds and remove chemical interaction contaminations compared to the annealing process.

To obtain the clean and crystalline surface, as required by our precise techniques (following sections), several cycles of annealing and sputtering are required. Moreover, it is compulsory to end with the annealing process to compensate the destroyed surface after sputtering. With the interconnected vacuum chambers, it is convenient to check if the crystal is clean enough by a quick UPS or XPS scan.

3.1.2 Organic Molecular Beam Deposition

Having a clean and crystalline substrate prepared, the degassing of organic molecules is performed to purify the material, which would be contaminated by CO_2 or H_2O due to its exposure to air before installation into the UHV system. The thin films studied through this work, including (sub)monolayers and multilayers, have been prepared by organic molecule beam deposition (OMBD) process [51, 129].

As shown in Fig. 3.1, the sketch of the crucible containing the organic molecules, and deposition process are displayed. In Fig. 3.1(a), the cylinder glass crucible that is twined by the metal wire, which can be heated resistively until the desired temperature is reached. Later on, the organic molecules are evaporated and deposited on the substrate held on the sample holder, as depicted in Fig. 3.1(b).

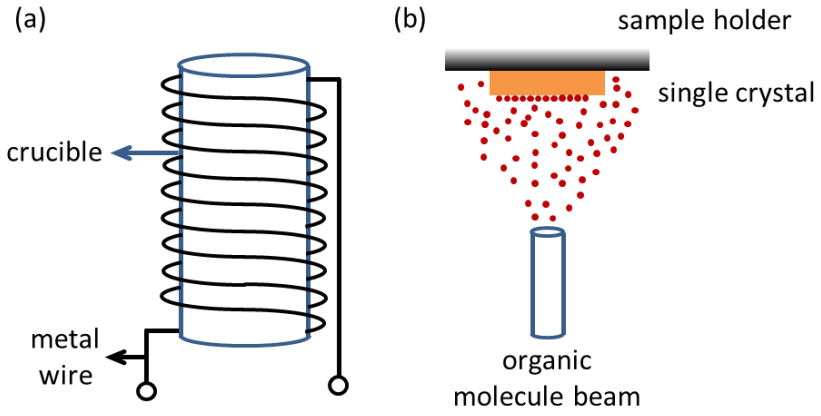

Figure 3.1: Sketch of a crucible (a) and thermal organic molecule beam deposition (OMBD) process (b).

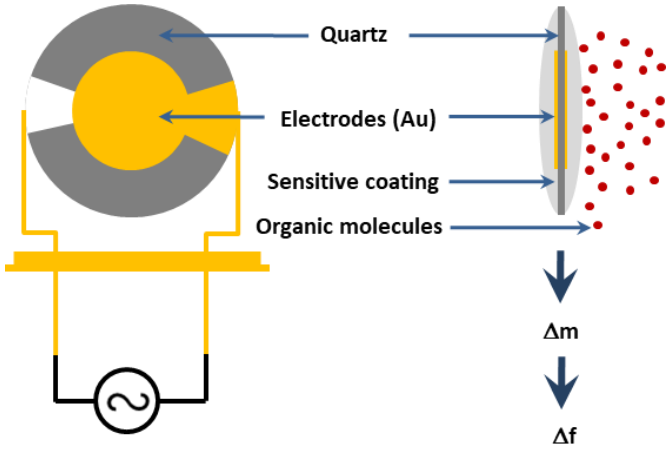

Figure 3.2: Sketch of a quartz crystal microbalance (QCM) sensor. Based on Ref. [130].

A quartz crystal microbalance (QCM) sensor has been placed at the deposition position to precisely calculate the deposition rate, which is systematically shown in Fig. 3.2. A QCM sensor is a kind of mass sensor, while it is based on a quartz crystal with an electrode equipped in the center, e.g. Au. Sensitive coating is applied on the surface to detect evaporated organic molecules. Consequently, the mass changes on the sensor and can be then converted into the frequency signals, allowing for a precise reading of rate and overall thickness [130].

For some technical reason, the sensor and the sample usually cannot be in the same direction or the same distance to the deposition source. Therefore, before the deposition process, the QCM requires the use of a tooling factor [131] in order to

calculate the true deposition rate at the substrate surface, whereas, it is defined considering the specific setup. The corrected tooling factor is applied during real experiments. Another factor which needs to be taken into account during this process is known as sticking coefficient [132]. It is a sensitive function of the nature of the particle-surface interaction, in this thesis, the molecule-coinage metal crystal interactions, which adapts a value between 0 and 1, where for 0 no molecules adsorb on the substrate and for 1 (an ideal situation) all molecules adsorb on the substrate. [133]

A QCM measurement is always conducted before the actual deposition takes place. After a stable evaporation rate is achieved, the QCM is removed and the substrate is put in the position.

3.2 Experimental Techniques

In the following section, the applied techniques will be introduced. Firstly, the photoelectron spectroscopy (PES) is addressed [134], separated into ultraviolet photoelectron spectroscopy (UPS) and X-ray photoelectron spectroscopy (XPS) which are sensitive to surface electronic properties. Then the main characterization method X-ray standing wave (XSW) technique, the forward step of XPS, lastly low-energy electron diffraction (LEED) to obtain the planar information of the thin films is introduced.

In general, the surface sensitive experiments are conducted under UHV conditions. It is due to the reason that gas molecules in the air could be absorbed on the solid surface, and will change the surface properties. However, in spite of the high vacuum of 10^{-6} mbar, there will be few layers of contaminations adsorbed on the bare solid surface. Nevertheless, it only happens until few hours under the UHV condition (< 10^{-9} mbar), thereby, we can get enough time to carry out the regular measurements [135, 136].

3.2.1 Ultraviolet Photoelectron Spectroscopy (UPS)

Ultraviolet photoelectron spectroscopy, UPS, has been established as a popular technique in recent years, to determinate surface and interface electronic properties

for atoms, molecules and solid materials. Furthermore, this technique has widespread application in various field like surface and material science, and holds significant contributions in the study of fundamental principles in solid state physics [137, 138]. Due to the low energy of ultraviolet (UV), in the energy range around 10 – 100 eV, it has a narrow line width so that only outer valence band electrons can be ionized and excited [46, 139]. Based on the UPS data, through the theoretical analysis of the spectrum, one can easily get the surface information of the molecular orbital levels, work function and density of states (DOS). Accordingly, UPS is widely used to study the interface between (in)organic semiconductors and metals, as well as the electronic structures in various kinds of molecules and polymers [140, 141].

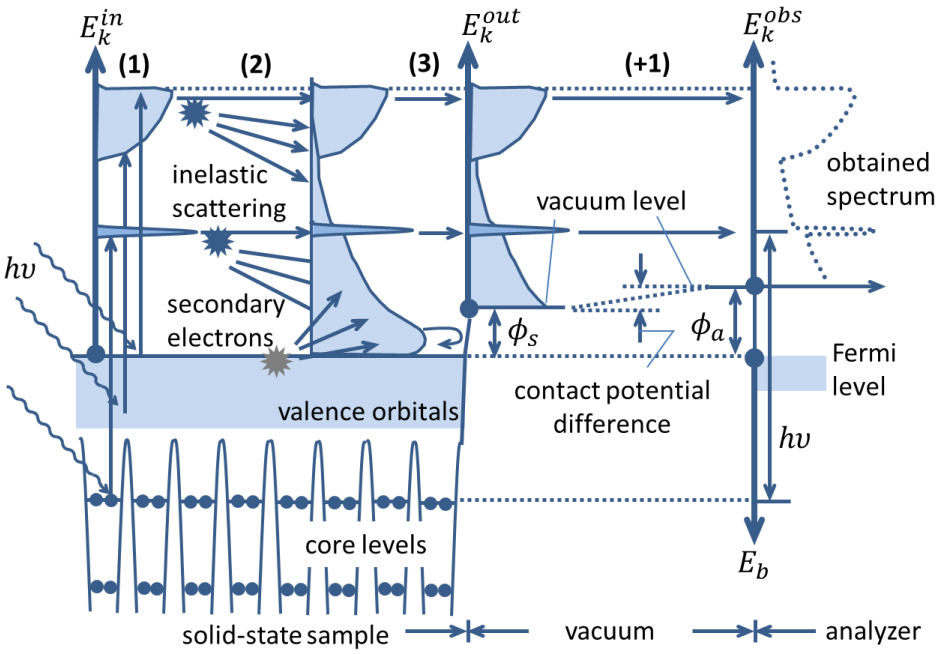

Figure 3.3: Schematic drawings of UPS as a three-plus-one step process, indicating the energy conservation: (1) photoexcitation of electrons; (2) inelastic scattering and secondary electrons; (3) penetration through the surface (barrier) and escape into the vacuum; (+1) photoelectrons collected by the analyzer. Image based on Ref. [142].

The three-plus-one step process of UPS technique is illustrated in Fig. 3.3, and the parameters are as same as introduced in Section 2.1. As sketched in Fig. 3.3, the UPS procedure is broken into three plus one distinct independent processes, which makes it simple to understand. In the first step (1), photoexcitation is fabricated on

the detect position under UV light ($h\upsilon$), then the photons are adsorbed and electrons are excited into photoelectrons with kinetic energy (E_k^{in}). In the second step (2), some photoelectrons lose their kinetic energy by the inelastic scattering in the solid before reaching the surface, which means part of the photoelectrons preserve their energies attenuate deeper into the solid. In the third step (3), the photoelectrons escape from the surface and emit into the vacuum, as E_k^{out} means the kinetic energy of the photoelectron out of the solid and ϕ_s the work function (surface potential) of the sample. Last, the plus one (+1) step, photoelectrons are collected and analyzed by a hemispherical analyzer (Fig. 3.19 and Fig. 3.20), with the output spectrum by the analyzer. In reality, the whole process is one-step process, however, the division into different steps can be justified reasonably and makes the interpretation much simpler [142, 143].

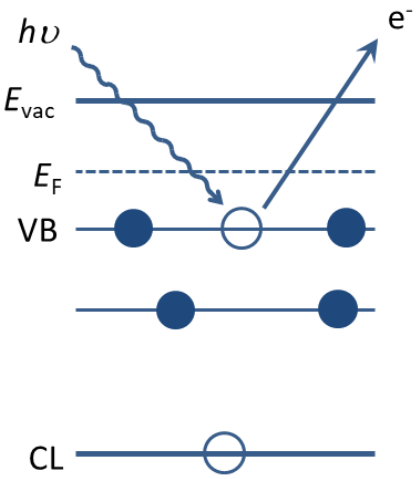

Figure 3.4: Schematic of electronic structure. Excitation of valence band electrons by incoming ultraviolet, then photoelectrons are emitted.

As introduced above, UPS is a technique based on the photoelectric effect [144, 145], and the processes are schematically shown at valence band (VB) in Fig. 3.4, as a comparison of XPS, which will be introduced in the next section, regarding to the following equation [146]:

$$\mathrm{E_k} = h\upsilon - \mathrm{E_b} - \Phi_\mathrm{s}, \tag{3.1}$$

where in the equation, $\mathrm{E_b}$ the binding energy, $h\upsilon$ the photon energy by the emission source, $\mathrm{E_k}$ the kinetic energy of excited photoelectrons, Φ_s the work function of the electron analyzer. As shown in Fig. 3.4, electrons from the VB are excited under UV emission and escape into the vacuum ($\mathrm{E_{vac}}$) state. The binding energy of photoelectrons is defined by the occupied orbitals so that by detecting kinetic energy

of electrons excited from, the energy of molecular orbitals can be represented by the collected spectrum [147].

The commonly used UV sources are listed,

H (Lymann α)	Ne I	He I	He II
10.2 eV	16.8 eV	21.2 eV	40.8 eV

or a synchrotron radiation source is used to reach a continuous range of photon energies (52 eV to 120 eV) of ultraviolet, as published in Ref. [56], by adjusting optical slides.

The UPS setup employed in this thesis is based on the He I radiation, while the UV light is generated by helium atoms with the electrons transmitted from 2p orbital to 1s orbital. The base pressure of the setup is maintained at 2^{-10} mbar.

Data analysis:

The UPS spectra are recorded with the following steps, a full scan (survey) and a zoom in scan at normal emission (horizontal direction), as well as the secondary electron cut-off (SECO) spectra (Fig. 3.5a). HOMO sensitive scans (Fig. 3.5b) are carried out at 45° (Fig. 3.21 in Section 3.2.5) as well as a survey scan that covers all energy range (main curve in Fig. 3.5).

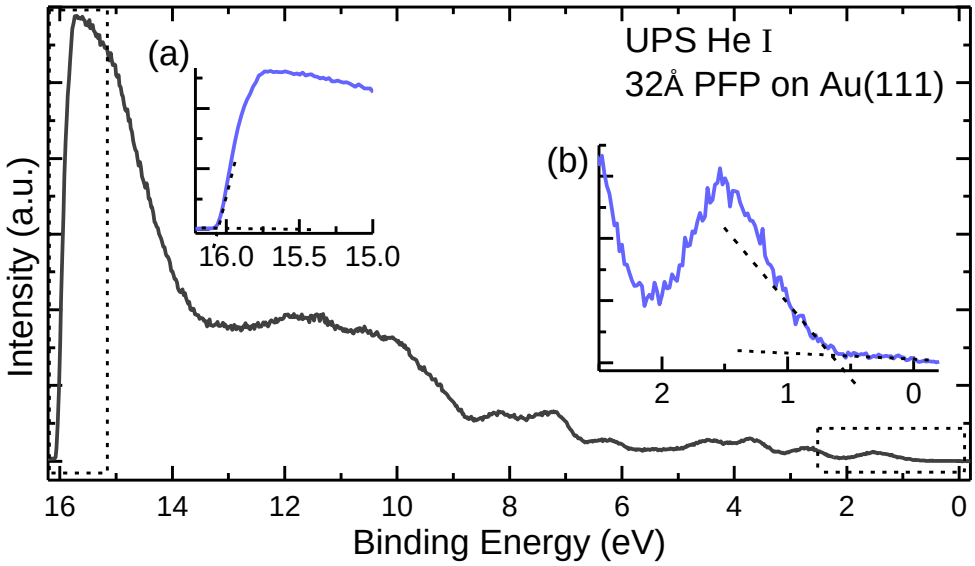

Figure 3.5: UPS spectra of a 32 Å PFP on Au(111), recorded at 45°. (a) Zoom in SECO spectrum, which determines the work function; (b) Zoom in valence band spectrum, which determines the HOMO position and HIB value. Data taken from Ref. [148].

In general, **(1)** the measurements taking at normal emission provide us an overview of the sample, metal Fermi-edge (~ 0 eV), work function (Fig. 3.5a), and new features indicating thickness variation. **(2)** The spectra recorded at 45°, where the electric vector of the photons and the momentum vector of photoelectrons are on a plane perpendicular to the sample surface [103], are more sensitive to the valence band of organic molecules, but shows lower metal d-band and Fermi-edge intensity compared to the normal emission scan. The comparison of HOMO signals measured at two angles are referred to Part II. The experiment performed at 45° implies to characteristic peaks of the sample, depends on the substrate and the organic molecules, like a shape peak at the binding energy around 13 eV is attributed to highly oriented pyrolytic graphite (HOPG) [149] substrate or a broadened peak saturated around 9 eV – 12 eV is a signal of the fluorinated organic molecules [150]. With respect to the signal intensity, we could hypothesize the qualitative amount of the materials. **(3)** In the valence band spectra (zoom in scan at 45°), the HOMO onset (cutoff in Fig. 3.5b) is the vital parameter to define the hole injection barrier (HIB) of the thin films on the single crystals.

3.2.2 X-ray Photoelectron Spectroscopy (XPS)

X-ray photoelectron spectroscopy (XPS) shares the same principle (Einstein's photoelectric effect) as the UPS technique, but with different photon energies, so that this technique can detect different excited photoelectrons [151, 152]. In analogy to UPS, XPS mainly focuses on the surface electronic configurations, as well as the chemically active components. Therefore, XPS has been widely used in these areas, i.e. investigation of various catalysts, adsorption and metal oxidation [153, 154]. The basic principle of XPS has been displayed in Fig. 3.6, the incoming X-ray emits onto the sample, and electrons are excited from core-levels of the surface atom to be photoelectrons. The photoelectrons are detected by the hemispherical analyzer (Fig. 3.19 and Fig. 3.20).

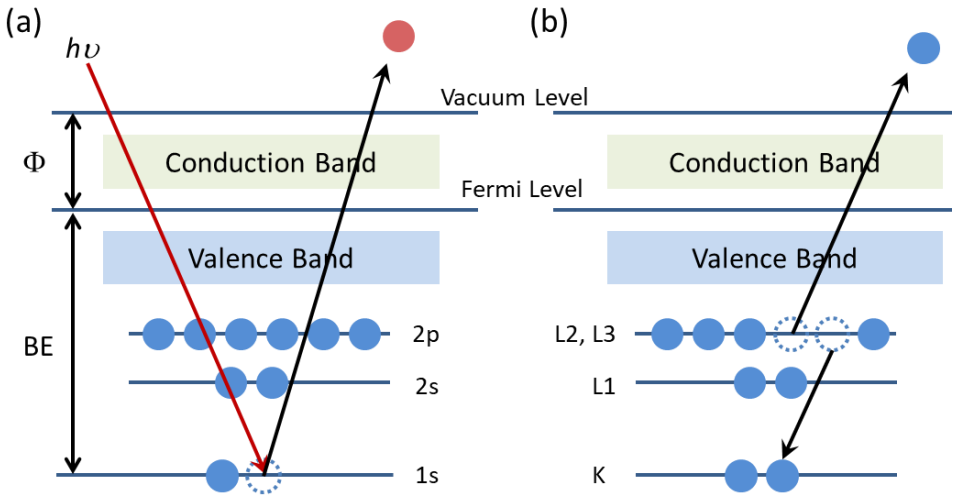

Figure 3.6: Fundamental principles of XPS technique. (a) Excitation of core-level electrons by incoming X-ray and photoelectrons emission. (b) Illustration of emitted Auger electrons process.

During an XPS scan (Fig. 3.6a), a hole appears in the excited core-level (CL), so that an electron from an outer level can jump to the inner core-level and take the position, meanwhile releasing energy. In some cases, the energy transfers into light, while in some other situations, the released energy can excite another electron. This is called Auger electron, the second photoelectron in one process (Fig. 3.5b). In consequence, when performing an XPS survey scan, the Auger electron spectra can be determined as well [41, 155].

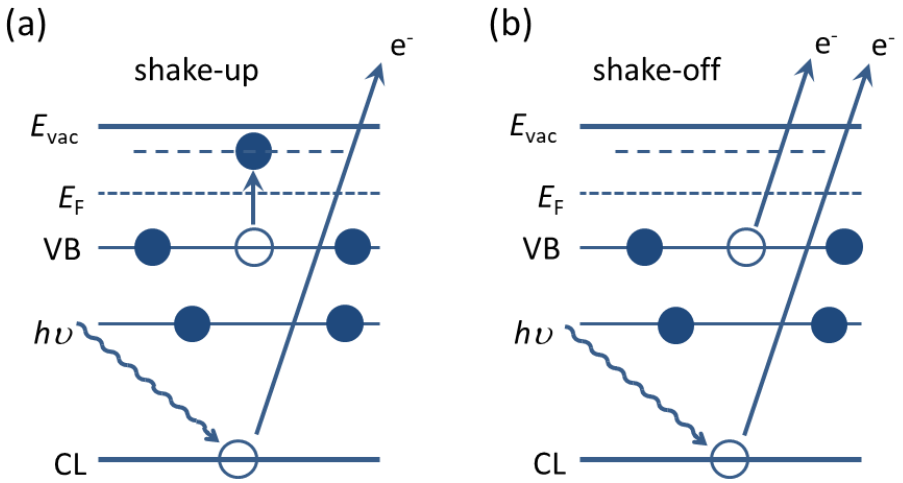

Figure 3.7: Two electron processes that can occur from a core-level (CL) during XPS excitation process. (a) Shake-up process, (b) shake-off process [156].

Apart from the Auger electron spectra, other phenomena have to be taken into account during the XPS process, as shown in Fig. 3.7, the shake-up (a) and shake-off (b) processes. With the incoming X-ray beam, an electron is excited and escapes into the vacuum. However, during this process, the photoelectron will consequently lose a certain amount of kinetic energy, thus this amount of energy shows a rather distinctive behavior. In Fig. 3.7(a), the shake-up phenomenon has been systematically structured as the lost kinetic energy excites another electron in the VB to an unbound state. Likewise, the lost kinetic energy may also excite a VB electron to vacuum state, as shown in Fig. 3.7(b). These processes are detectable but with a lower kinetic energy, in another word, a higher binding energy.

In general, Mg and Al target are the commonly used X-ray sources, the photon energies emitted by them are 1253.6 eV (Mg Kα) and 1486.6 eV (Al Kα). While an Al target is mostly used in this thesis, with a monochromator to access single wave length X-ray, except the XPS performed in the synchrotron, since the synchrotron can produce soft-XPS (SXPS) and hard-XPS (HXPS) with the consecutive energy ranges of 230 – 800 eV and 2.1 – 18 keV, respectively.

Data analysis:

As a useful tool to detect elements in different chemical environments, it is essentially important to analyze the XPS data, in another word, to fit different elemental donations as the technique can distinguish the same element within different chemical environments. With the help of the XPS handbook and other literature [157-160], the desired element can be determined by a certain range of binding energy region. However, despite the instruction by the handbook, as well as the setup condition, the specific case often shows the rather distinctively behavior.

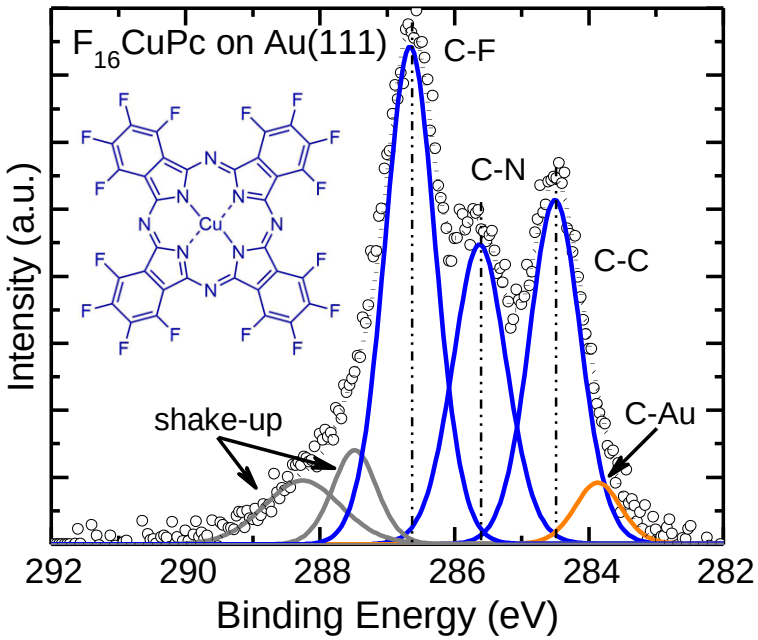

Figure 3.8: XPS data analysis. C 1s core-level spectrum of monolayer $F_{16}CuPc$ on Au(111). Data taken from Ref. [102].

As provided in Fig. 3.8 (data taken from Ref. [102]), the C 1s core-level spectrum is recorded with a monolayer $F_{16}CuPc$ deposited on Au(111) substrate. **(1)** To fit an XPS core-level spectrum [161], the software CasaXPS [162] is required. By utilizing this software, one can fit an XPS spectrum with rational contributions, as shown in Fig. 3.8, three distinguishable peaks with highest domain are fitting and colored into blue, remaining two grey peaks and a golden peak. **(2)** To reach the fitting results, we need to consider the chemical structure (insertion) first, and think about what kind of background to employ. **(3)** Usually, a Shirley background [163, 164] is adopted when analyzing the core-level spectra, depending on the situation, background subtraction needs to take place as well. In Fig. 3.8, the background subtraction is applied with a Shirley background at the beginning [165]. **(4)** Subsequently, based on the chemical structure of $F_{16}CuPc$, three distinctive carbon atom species are exhibited, nominated as C-C (carbon bound to another carbon atom), C-N (carbon bound to a nitrogen atom) and C-F (carbon bound to a fluorine atom). One can either rely on the XPS handbook [157] to figure out each contribution, or compare with the published literature [166-168], or distribute the peak contributions according to the effect by its neighboring atom, with a negative

charged atom leading to lower kinetic energy (higher binding energy). **(5)** Another parameter that needs to be considered is the full width at half maximum (FWHM) [169, 170], while during XPS analysis a reasonable range of FWHM is around 0.7 - 1.2 eV. **(6)** In the end, shake-up contributions have to be fitted without any limit of FWHM and peak shapes. Moreover, in this case, a small peak located at lower binding energy is linked to the broken C-F bonds (for a detailed discussion the reader is referred to Chapter 4), so that the carbon atoms are connected to the substrate (C-Au). After all the procedures, it provides high precision as depicted in Fig. 3.8.

3.2.3 X-ray Standing Wave (XSW) Technique

Related to the XPS technique, X-ray standing wave (XSW) technique [91, 171, 172] provides a method to further exploit the X-rays, and is a technique helping to determine the adsorption geometry and the adsorption distance of specific atoms in the organic molecules. The XSW technique is mainly based on a combination of the theory of dynamical diffraction (TDD) and XPS (introduced in 3.2.2). This technique has the advantage as it takes into account all wave interactions within the crystalline particle (both single crystal substrates and organic thin films) [173, 174], and it provides highly precision to determine the adsorption distance (typically ± 0.05 Å).

In general, there are several methods to employ the XSW technique, all in terms to generate the XSW field by crystal or surface reflection and detect photoelectrons or fluorescence [39, 171, 173]. To start with, the dynamical theory of X-ray diffraction derives the wave fields from the Maxwell equations [175] for a periodic electron density inside the crystal, the process is systematically shown in Fig. 3.9. The incident and diffracted wave vectors, $\boldsymbol{K}_0$ and $\boldsymbol{K}_\mathrm{H}$, fulfill the Bragg condition:

$$\boldsymbol{K}_\mathrm{H} = \boldsymbol{K}_0 + \mathbf{H} \tag{3.2}$$

with $|\boldsymbol{K}| = 1/\lambda$ and $\mathbf{H}$ being the reciprocal lattice vector.

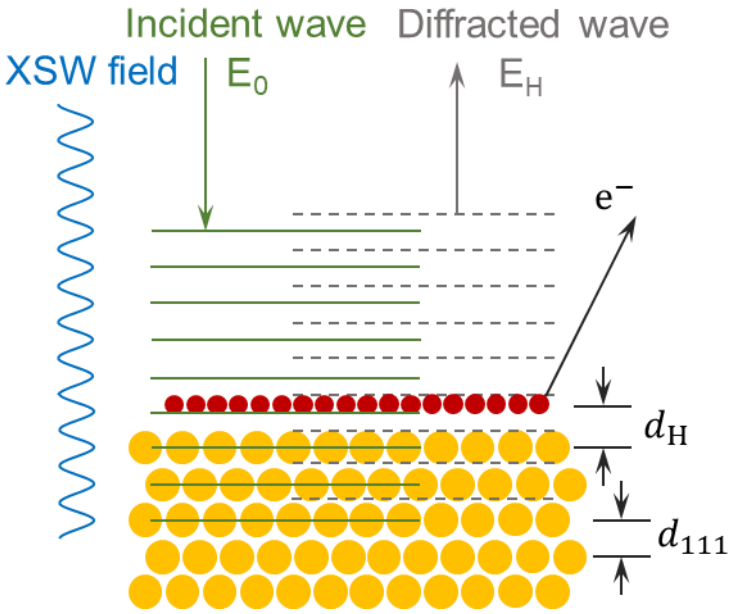

Figure 3.9: Fundamental principles of normal-incident XSW technique, which is produced by Bragg reflection of monochromatic X-rays from a single crystal substrate. The intensity variation of the photoelectron yield when scanning through the Bragg condition depends on the crystal lattice bonding distance (d_0). The sketch is based on Ref. [176].

As shown in Fig. 3.9, for which most cases are performed during real measurements, it is assumed that only two wave factors (two-beam approximation), $\mathbf{E}_0$ and $\mathbf{E}_\mathrm{H}$, almost perpendicular to the substrate, contribute to the amplitude. Therefore, the electrical field at position $\boldsymbol{r}$ can be described as the superposition of the incident and diffracted wave:

$$\mathbf{E}_0(r) = \sum_s e_{0s}\mathrm{E}_0 e^{-2\pi i K_0 \cdot \boldsymbol{r}} \tag{3.3}$$

$$\mathbf{E}_\mathrm{H}(r) = \sum_s e_{Hs}\mathrm{E}_H e^{-2\pi i K_H \cdot \boldsymbol{r}} \tag{3.4}$$

In the above equations, e_{is} presents the polarization factor (C), with two states σ, π ($\mathrm{C} = 1$, the σ polarization; $\mathrm{C} = \cos 2\theta$, the π polarization) [176]. During measurement, the incoming wave energy $E = hc/\lambda$ is calculated via the Bragg condition $\lambda = 2d_{hkl} \sin\theta_{\mathrm{Bragg}}$, and scanned around the energy (further information shown in Fig. 3.11).

Now the normalized spatial intensity variation I^{XSW} is defined as the following equation:

$$I^{\mathrm{XSW}}(v,\mathbf{r}) = \frac{|\mathbf{E}_0 + \mathbf{E}_\mathrm{H}|^2}{|\mathrm{E}_0|^2} = 1 + \left|\frac{\mathrm{E_H}}{\mathrm{E_0}}\right|^2 + 2\mathrm{C}\left|\frac{\mathrm{E_H}}{\mathrm{E_0}}\right|\cos(v - 2\pi\mathbf{H}\cdot\mathbf{r}) \tag{3.5}$$

This equation describes the intensity of the XSW field, meanwhile, the time dependence has been removed so that the maxima and minima do not change with the time.

By knowing the reflectivity R with $E_H = \sqrt{R}E_0 e^{iv}$, the above equation is modified into the following formation, with the spatial and phase modulation:

$$Y_P(v,\mathbf{r}) = 1 + R + 2\mathrm{C}\sqrt{R}\cos(v - 2\pi\mathbf{H}\cdot\mathbf{r}) \tag{3.6}$$

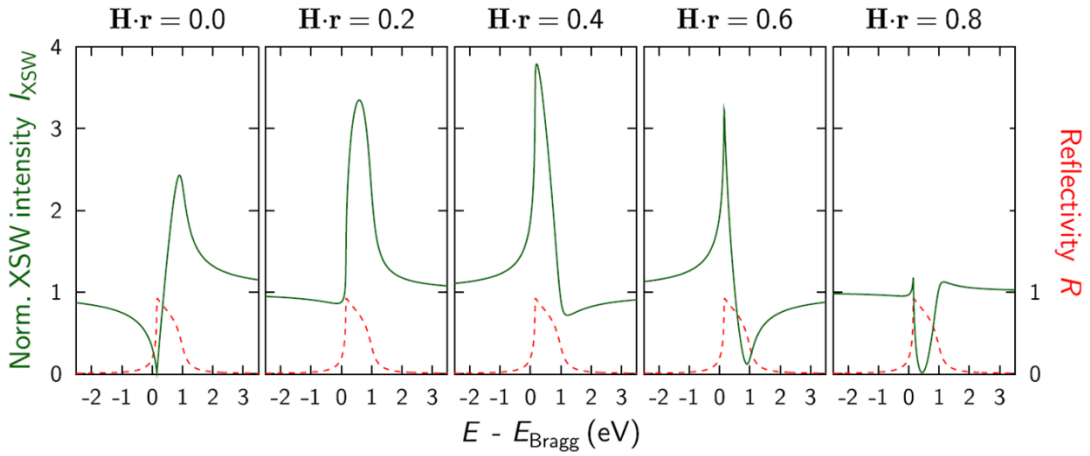

Figure 3.10: Normalized intensity of the XSW field for different $\mathbf{H}\cdot\mathbf{r}$, at different z/d_0 positions in the standing wave field, for a given Bragg reflection curve. The figure is adapted from Ref. [177].

By measuring the variation of the photoelectron yield Y_P, the spatial dependence of the intensity filed is illustrated in Fig. 3.10, as the paralleled $\mathbf{r}$ to $\mathbf{H}$ can be retrieved. Since the system is periodic, the curve repeats by a certain number, in this case, the period is 1. We now again simplify the structural information of the measured species, two parameters are introduced to compact the equation:

$$Y_P(h\nu) = 1 + R + 2\sqrt{R}f_\mathrm{H}\cos(v - 2\pi P_\mathrm{H}) \tag{3.7}$$

In this equation, the obtained two parameters are defined as: coherent fraction ($0 \le f_H \le 1$), providing the ordering of the detected atom, while $f_\mathrm{H} = 0$ for a completely disordered system and $f_\mathrm{H} = 1$ for a case of all the detected atoms at the same adsorption distance. The coherent position ($0 \le P_\mathrm{H} \le 1$), provides the relative atomic position $\boldsymbol{r}$ in the given diffraction planes as shown in Fig. 3.9 [92]. The

adsorption distance (d_{H}) in real space has a relationship with P_{H} given in the following equation:

$$d_{\mathrm{H}} = d_{hkl}(n + P_{\mathrm{H}}) \tag{3.8}$$

In the equation, d_{hkl} is the lattice plane of the substrate, n is an integer.

Data analysis:

To analyse the XSW data, based on the fitting mode by XPS, it requires us to carry out further procedure converting these theoretical information into real data. To introduce the process of data analysis, the Au(111) single crystal is taken as an example.

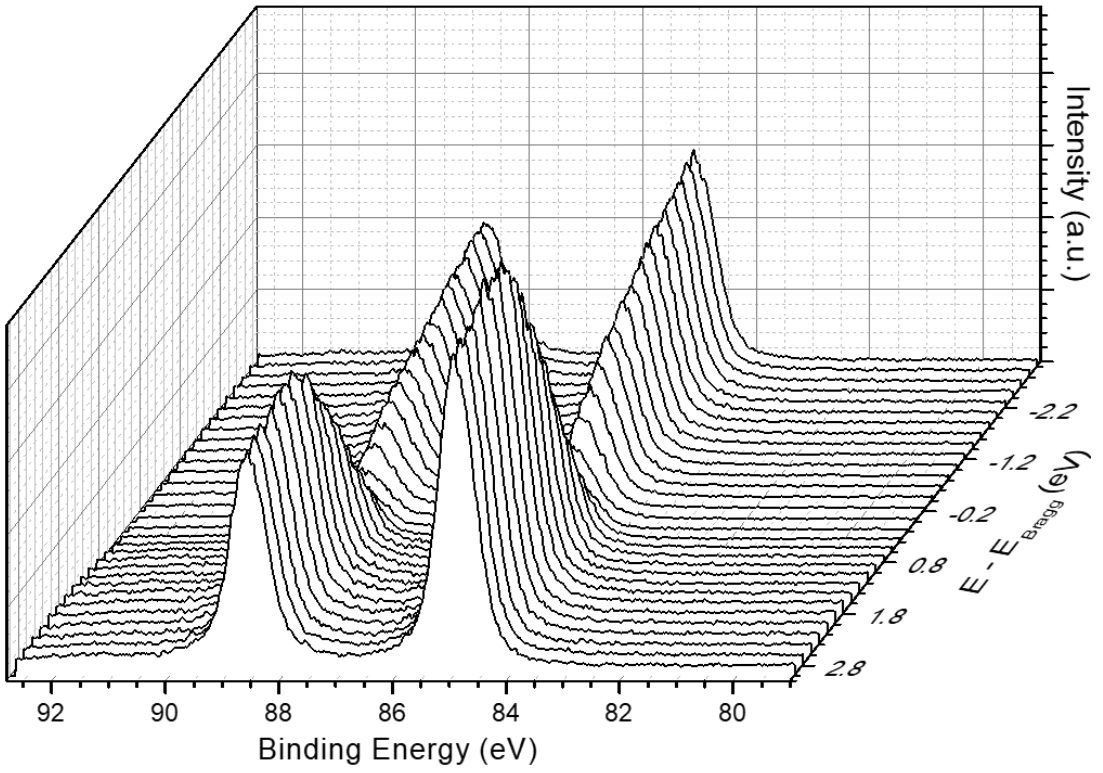

Figure 3.11: A set of XSW measurements on Au(111) single crystal. The X-axis is binding energy, the same as in the XPS spectra; Y-axis the intensity, usually of arbitrary unit; Z-axis the difference between the photon energy (E) and the Bragg condition (E_{Bragg}), each curve is recorded around the Bragg condition.

As being introduced in the beginning, the XSW measurement scans the sample through the Bragg condition. In Fig. 3.11, the Au(111) Bragg energy is known (2635 eV), therefore we use the photon energy near the Bragg condition, in this case, ± 3

eV, as shown in the z-axis ($E - E_{\mathrm{Bragg}}$). The XPS measurements then have been performed through the photon energy of 2635±3 eV, with a 0.2 eV interval. Each curve in the figure indicates an XPS scan of a specific photon energy, and the photoelectron analyser collects Au 4f signals (BE range 79 eV to 93 eV). With a sum of all spectra, the fitting process of XPS is applied on the spectrum to figure out the different chemical environments of the detected atom. Since we take Au(111) single crystal as the sample, the Au 4f core-level can be determined to the fine structure, i.e. Au $4f_{7/2}$ (~84 eV) and Au $4f_{5/2}$ (~88 eV).

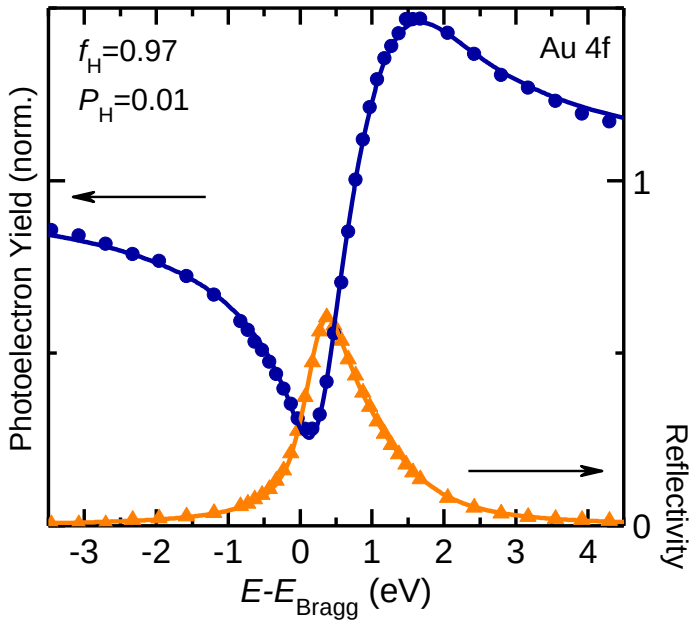

Figure 3.12: The typical XSW figure, while Au(111) is shown as the specimen. The photoelectron yield curve is generated corresponding to Fig. 3.11 and the reflectivity curve is recorded during the XSW scan. The two parameters, f_{H} and P_{H}, are shown with the calculated values.

The photoelectron yield (Y_{P}) is extracted from the XPS fitting results, more precisely, the area below the curve is used to evaluate the photoelectron yield. Consequently, the average position of the atom can be determined, according to Equation 3.8. The photoelectron yield curve and reflectivity curve of Au 4f core-level have been displayed in Fig. 3.12. In the figure, the normalized photoelectron yield (blue) is referred to the left y-axis, and the reflectivity curve (golden) to the right y-axis. The coherent fraction obtains 0.97 (close to 1), showing the highly ordered

single crystal properties; the coherent position is near 0, showing the same lattice unit, in another word, the adsorption distance of first layer gold atoms, (small atoms inorganic molecules) as Au itself.

3.2.4 Low-Energy Electron Diffraction (LEED)

As a technique to study the surface properties of solid samples, low-energy electron diffraction (LEED) is widely used on the atomic structures of different single crystals. With the acquired LEED patterns, one is able to investigate the arrangement and lattice space of outer layers on a sample, which makes the method a reliable way to analyse the surface atomic structures. Until now, hundreds of clean surfaces and adsorption layers on the surface have been studied by LEED [178]. It is rather simple to observe a LEED pattern despite it cannot reveal precisely surface structures, but it is possible to get most of the information from a surface qualitatively. We could learn about periodicity of the atomic arrangement and its symmetry through LEED, which is related to the structure, size and orientation of the unit cell, from where we can estimate whether the reconstruction happens among the surface adsorption [179].

Nowadays, the typical LEED setup is called “back-display” system, and the structure of it is shown in Fig. 3.13. In both sketches, the incident electron beam, generated by the electron gun, is accelerating when crossing the electric field, and electrons are then emitted to the transparent hemispherical fluorescent screen. Afterward, electrons pass a small hole on the screen and arrive to the sample surface. Generally, the electron beam has a diameter of around 0.3 mm to 1.0 mm, and the current is about 1 μA. The sample is put in the middle of the hemispherical so that the diffracted electrons will pass through one radius of the hemispherical to arrive at the LEED screen [178].

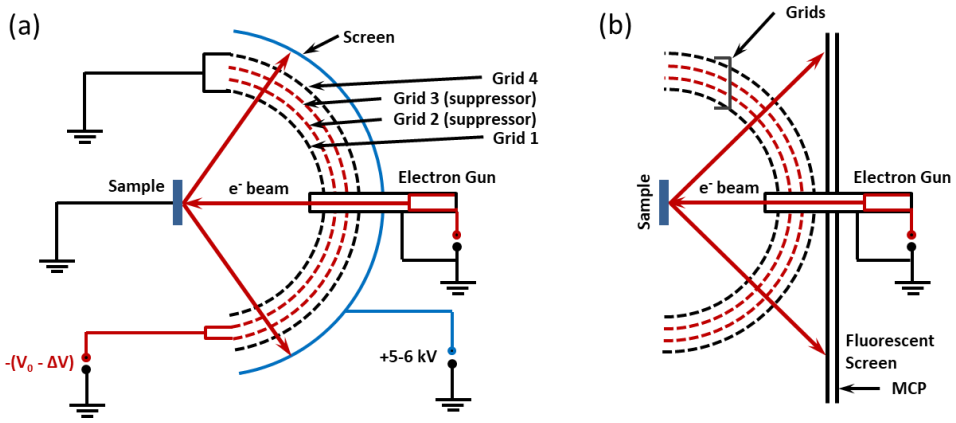

Figure 3.13: The sketch of a typical LEED setup. (a) is adapted from Ref. [180], and (b) is adapted from Ref. [181].

The surface of a circular shaped sample will be slightly influenced due to the electron beam. In order to reduce this error bar, a smaller diameter of electron beam is necessary. As a result, a microchannel plate (MCP) LEED, Fig. 3.13(b), is acquired to obtain an electron beam with a diameter of about 0.3 mm. Apart from the typical systems, a MCP LEED uses a flat screen to display diffracted patterns (see Ref. [181]). However, the LEED pattern will be distorted due to a flat screen. Since no further correction device is installed in the setup, a non-ideal LEED pattern will be collected. Therefore, the distorted patterns need to be corrected following these equations:

$$x = \frac{x_b r}{\sqrt{x_b^2 + y_b^2 + (r+d)^2}} \tag{3.9}$$

$$y = \frac{y_b r}{\sqrt{x_b^2 + y_b^2 + (r+d)^2}} \tag{3.10}$$

r is the radius of the grid, d is the length of the electron gun, x and y are the parameters in the LEED pattern after correction, while x_b and y_b are the original parameters [181].

To analyze the LEED patterns, we need to use the lattice structure theory in the solid-state physics. In a two-dimensional (2D) situation, two vectors, named $\vec{a}$ and $\vec{b}$, are used to define a lattice unit cell, also known as basic vectors. Based on the two basic vectors, there exist five Bravais lattices due to the periodical translation of the unit cells, called square, rectangular, centered rectangular, hexagonal and oblique, shown in Fig. 3.14. The reciprocal space parameters have a relationship with Bravais lattice according the equations:

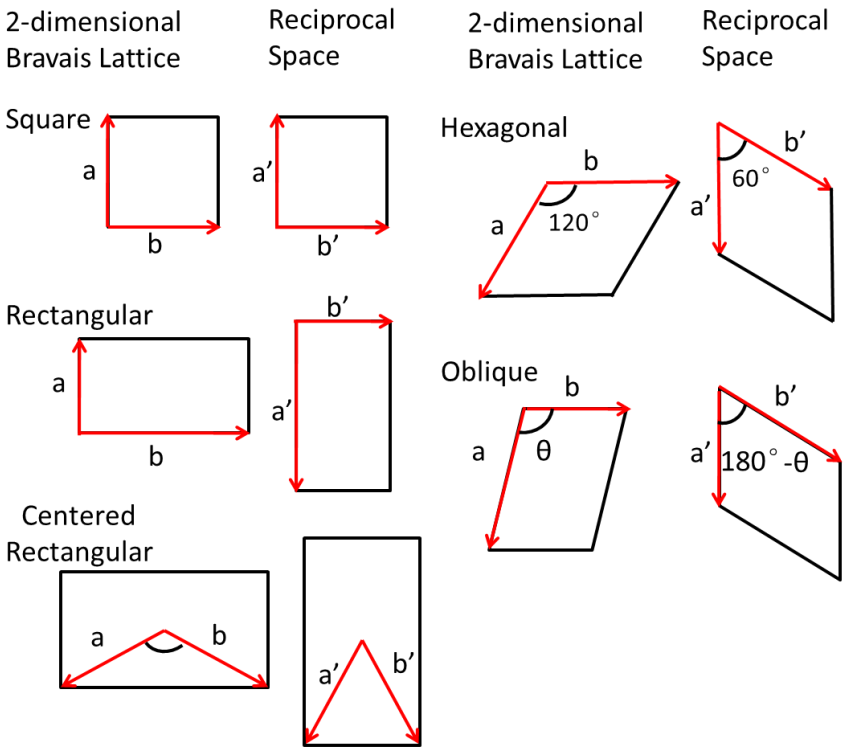

Figure 3.14: Five basic two-dimensional Bravais lattices and their reciprocal space structures.

$$\overrightarrow{a'} = 2\pi \frac{\vec{b} \times \vec{c}}{\vec{a} \cdot (\vec{b} \times \vec{c})} \tag{3.11}$$

$$\overrightarrow{b'} = 2\pi \frac{\vec{c} \times \vec{a}}{\vec{a} \cdot (\vec{b} \times \vec{c})} \tag{3.12}$$

In this equation, the third vector $\vec{c}$ is perpendicular to the plane formed by vector $\vec{a}$ and $\vec{b}$. Meanwhile, the reciprocal parameters and the basic vectors have a relation as [180]:

$$\vec{a} \times \overrightarrow{a'} = 2\pi, \vec{b} \times \overrightarrow{b'} = 2\pi \tag{3.13}$$

$$\vec{a} \times \overrightarrow{b'} = 0, \vec{b} \times \overrightarrow{a'} = 0 \tag{3.14}$$

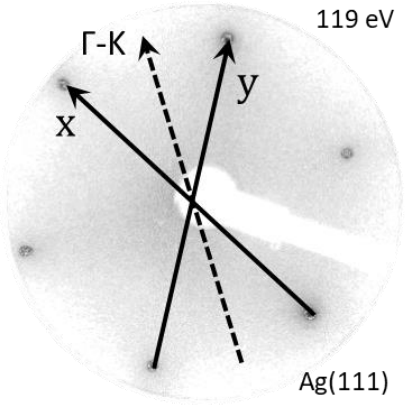

Figure 3.15: LEED alignment. A method to calculate Γ − K direction [182] of single crystal. Ag(111) was taken as a sample, this LEED pattern is taken from Ref. [55].

As a useful method to study surface structure of single crystals, it is also used to define the Γ − K direction in a crystal surface in its Brillouin zone[182], as shown in Fig. 3.15. In this figure, it is clear to see the six diffraction spots of Ag(111) single crystal, as well as a silver atom diffraction spot hidden in the center. The Γ − K direction has been defined as the direction, which is parallel to the crystal lattice. To correlate this direction with the set-up in the lab, we have to collect two parameters during LEED alignment, the α value of x and y, as marked in the figure. In this case, we got

$$\alpha_x = 29.35,\ \alpha_y = 15.70$$

When we calculate the average of these two values, the Γ − K direction is defined: $\alpha = 22.52$, which is crucial during UPS measurements at $\theta = 45°$. As a surface sensitive technique, the measurement along crystal Γ − K direction provide more subtle information to the HOMO signal of thin film less than a monolayer (nominal 4 Å).

The device used in this thesis is a MCP LEED, its total length is 80 mm, and the electron gun has a diameter of 10 mm. The electron beam energy range is between 5 eV and 750 eV, the beam current is 2 μA when the electron beam energy is 100 eV, the diameter of working area is 80 mm. The LEED patterns have been corrected before analysis.

Data analysis:

To analyze the LEED data, we need to know the calculation process from reciprocal space to real space, with the geometry of the diffraction processes shown below Fig. 3.16. The *x* is measured in pixels of the camera, which is a distance between two diffraction spots in a LEED pattern, *z* the distance between the target sample and electron gun (e-gun) and can be measured in the lab. The other parameters will be followed according to the Bragg condition, and replaced by the setup parameters.

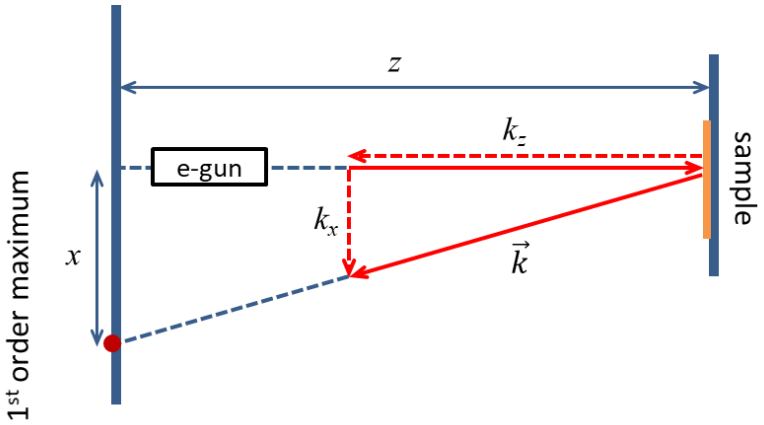

Figure 3.16: Geometry of the electron diffraction processes, each parameter is labelled with a specific symbol and is in line with the equations.

As illustrated in Fig. 3.16, there is

$$x \sim \frac{x}{z} = \frac{k_x}{k_z} \approx \frac{k_x}{|\vec{k}|} \sim \frac{k_x}{\sqrt{E}} = \frac{|\vec{b}|}{\sqrt{E}} \tag{3.15}$$

so that *x* is proportional to the last formula, while

$$E = \frac{\hbar^2 \vec{k}^2}{2m_e} \tag{3.16}$$

which is also the electron energy. For this reason, we have to define the relationship between *x* and the formula. As a well-defined single crystal, Au(111) (hexagonal lattice) can be used as the sample, whereas its lattice constant and the angle are known (Fig. 3.18):

$$|\vec{a}| = 2.884\ \text{Å}, |\vec{b}| = \frac{2\,\pi}{|\vec{a}| \cdot \sin 60^\circ}$$

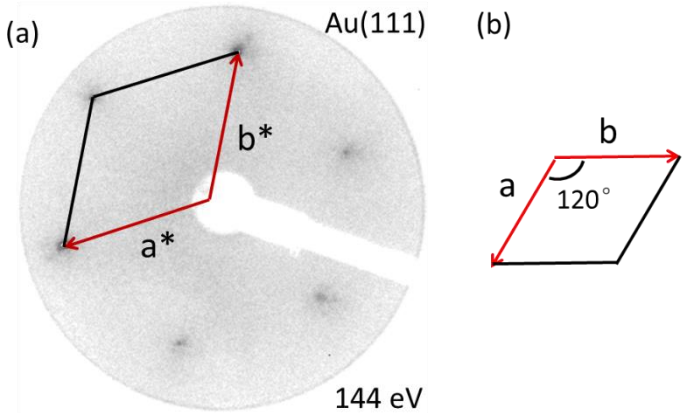

Figure 3.17: Analysis process of the LEED pattern. Au(111) single crystal surface is used as the sample, due to the crystalline structure and bright diffraction spots.

$$x = d\frac{|\vec{b}|}{\sqrt{E}} \tag{3.17}$$

In Equation (3.17), d is a constant value related to the setup, which needs to be calculated by the Au single crystal.

To analyze the LEED data, the LEEDpat software [183] is helpful to accomplish the definition of unit cells. In Fig. 3.17, after we seek out a meaningful unit cell in the LEED pattern, following the above equations, the two parameters (a and b) are calculated as shown in Tab. 3.1.

Table 3.1: Unit cell parameters of Au(111), a and b lattice length, angle and one unit cell area are shown, which are the same as the computational results [184].

/ Å	a	b	angle	area
Au(111)	2.86	2.91	118.5	7.2

3.3 Experimental Setups

All the measurements were carried out in Diamond Light Source (DLS, Didcot, UK), and in collaboration of Prof. Steffen Duhm in Soochow University (Suzhou, China).

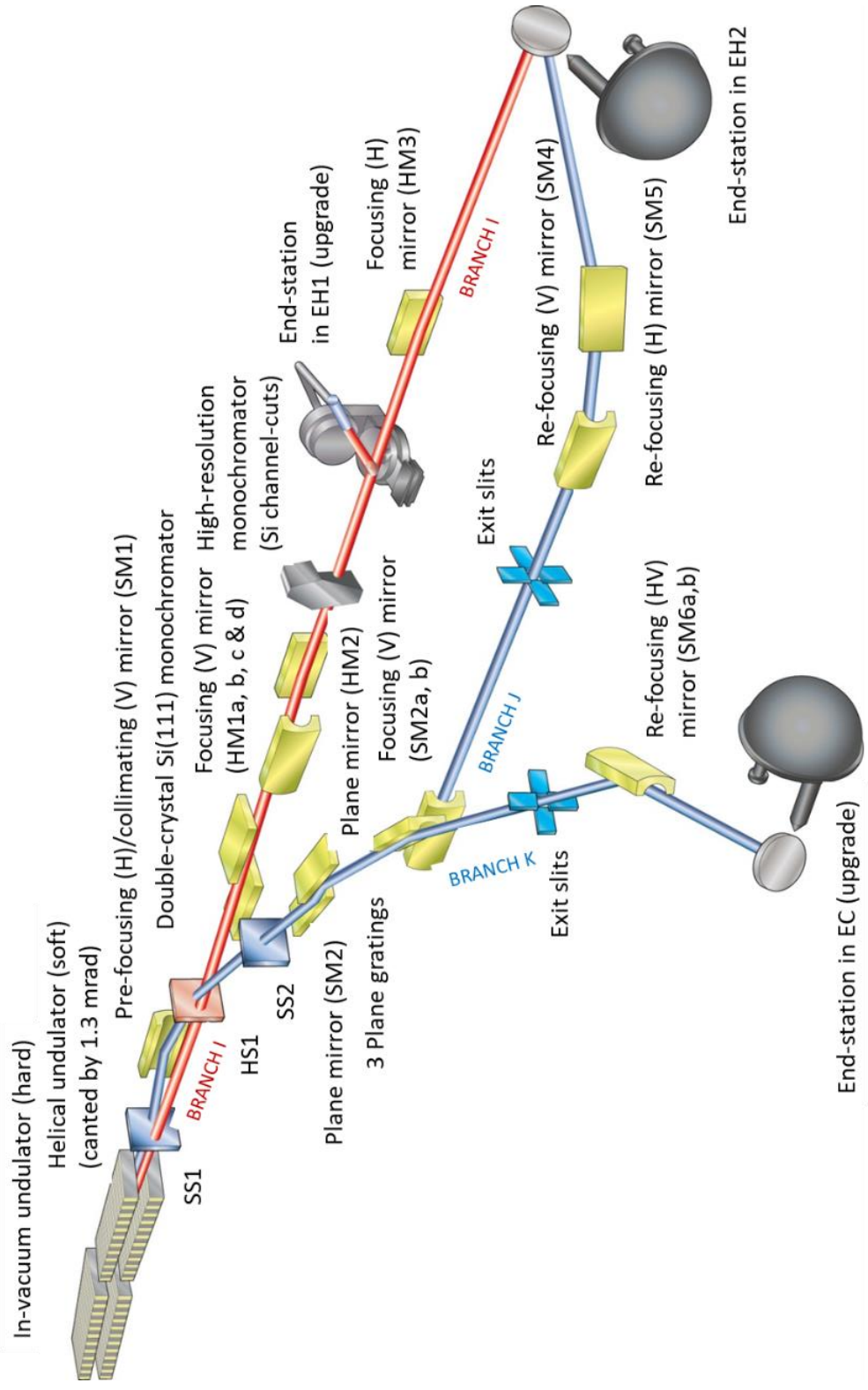

Figure 3.18: Sketch of beamline I09 at Diamond Light Source, Didcot, UK. The hard X-rays (I) and soft X-rays (J) branches can be focused on the same spot of the sample. Additional end-stations are to be built (branch K), where only the soft beam is used. Image taken from [185].

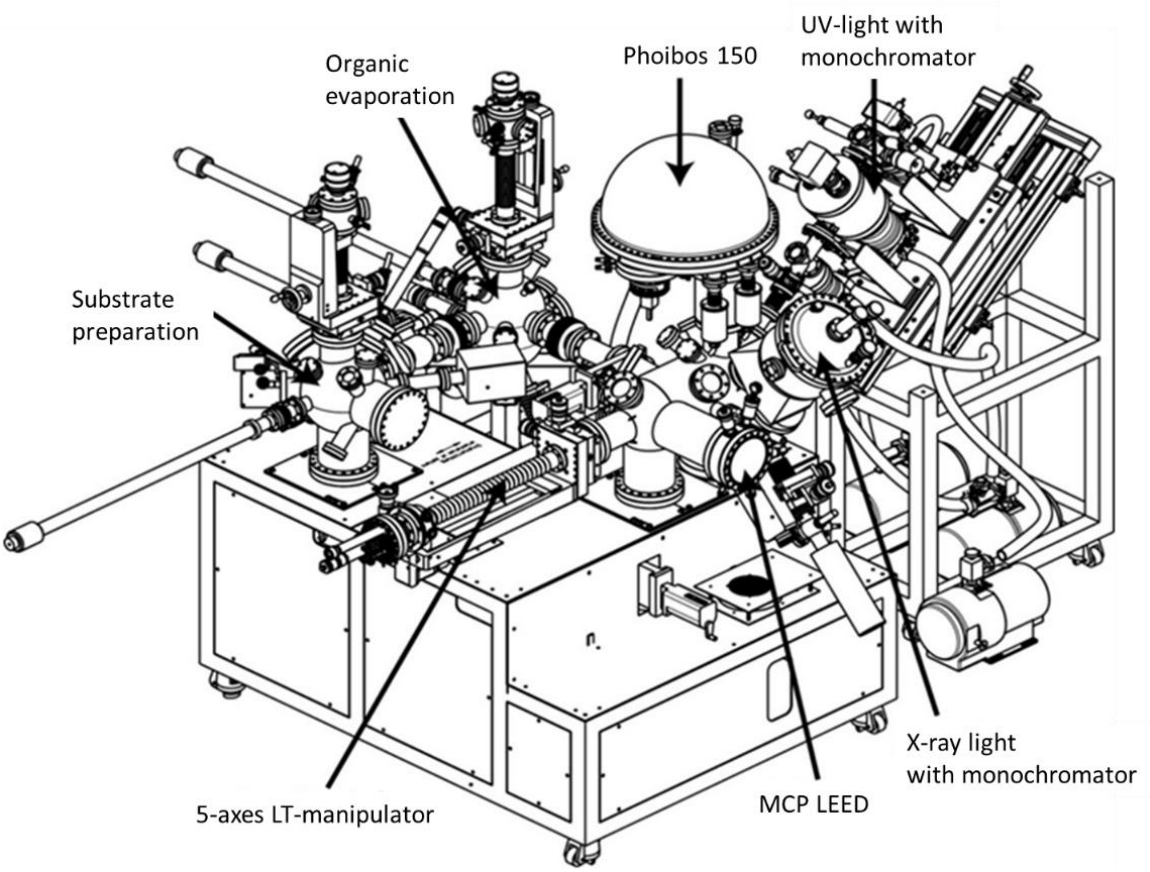

Figure 3.19: Sketch of the UHV setup at FUNSOM, Soochow University, China. Picture courtesy of SPECS GmbH.

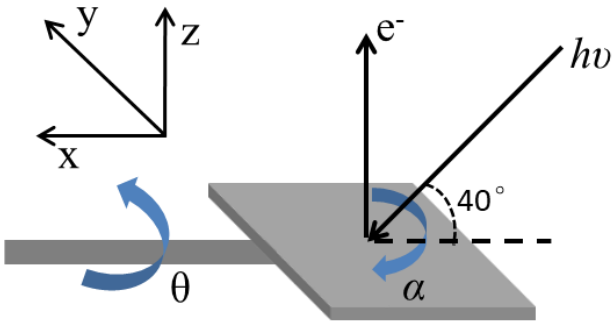

Figure 3.20: A sketch of the 5-axis sample manipulator, with x, y, z, θ and α. As x, y and z indicate the general coordinates in space, while θ and α show two rotating directions.

Part II

Results and Discussion

4. HETEROMOLECULAR BILAYERS ON AU(111)

The results presented in this chapter were published in Ref. [102].

Heteromolecular bilayers of π-conjugated organic molecules (COM) on metals, considered as model systems for more complex thin film heterostructures, are investigated with respect to their structural and electronic properties. By exploring the influence of the organic-metal interaction strength in bilayer systems, we determine the molecular arrangement in the physisorptive regime for copper-hexadecafluorophthalocyanine (F_{16}CuPc) on Au(111) with intermediate layers of 5,7,12,14-pentacenetetrone (P4O) and perylene-3,4,9,10-tetracarboxylic diimide (PTCDI). Using the X-ray standing wave (XSW) technique to distinguish the different molecular layers, we show that these two bilayers are ordered following their deposition sequence. Surprisingly, F_{16}CuPc as the second layer within the heterostructures exhibits an inverted intramolecular distortion compared to its monolayer structure.

4.1 Introduction

In recent years, heteromolecular structures have attracted significant attention [76, 186-188], especially because of their widespread potential for and use in organic (opto)electronic devices. In this context, both the electronic and structural properties of the organic layers are highly relevant as they have a strong impact on the charge carrier transport and thus overall device performance [147, 189]. The energy-level alignment at the organic-organic and organic-inorganic interface [38, 190], which is a key issue also for molecular heterostructures, has been subject of intense research [24, 46, 191, 192]. For a better understanding of more elaborate thin film architectures, different bi-component model systems on single crystal surfaces have been investigated. Deposited either as molecular mixtures [12, 29, 78, 193, 194] or bilayer structures [26, 27, 79] these systems show that the interplay of molecule-molecule and molecule-substrate interactions is rather complex and may even induce unexpected re-arrangement processes such as the exchange of the first and the second layer. Importantly, one might also observe significant molecular

distortions in those heterostructures [26, 27], which reflect the impact of the different interaction mechanisms on the adsorbed molecules.

To address the fundamental questions raised by these observations, one has to employ different molecule-substrate combinations. Detailed investigations of those systems using complementary experimental techniques allow for a controlled preparation of bilayer structures. It has been observed for heterostructures on Ag(111) that deposition of a second molecular species may induce a complete replacement of weakly interacting molecules in the first layer [26, 27]. Generally, chemisorption at organic-metal interfaces can lead to adsorption-induced molecular distortions in the contact layer [195, 196] and, consequently, to additional intramolecular dipole moments [197, 198]. In contrast, the interaction of molecular monolayers with inert surfaces is dominated by weak dispersion forces [55, 84, 199, 200]. To minimize the organic-metal interaction strength, we chose the Au(111) surface. This will allow to investigate whether such distortions occur in molecular bilayers on weakly interacting substrates as well and whether they are induced by the substrate or rather by intermolecular interactions. Since fluorination of organic semiconductors is expected to further weaken this interaction [201, 202], we employed the electron acceptor copper-hexadecafluorophthalocyanine (F_{16}CuPc) [203, 204] as the top layer. The fluorination leads, furthermore, to large chemical shifts in the C 1s core levels [205, 206], which is beneficial for analyzing XP spectra of the heterostructures.

In order to reduce the charge carrier barriers between the organic active layer and the metal electrode, different intermediate layers may be employed between F_{16}CuPc and gold. Accordingly, we use 5,7,12,14-pentacenetetrone (P4O) and perylene-3,4,9,10-tetracarboxylic diimide (PTCDI) (chemical structures inserted in Fig. 1) as the insertion layer. Both molecules form well-defined monolayers on clean metal surfaces [75, 97, 118, 207, 208] and are chosen because of their rather different surface unit cells [55, 209, 210], which allows to study a possible impact of (in)commensurability on the bilayer growth. For comparison, F_{16}CuPc has been grown also on Au(111) directly and with a P4O or PTCDI layer below. In our present work, the core-level signals and the molecular surface structures, including vertical and planar information, of the mono- and bi-layer systems have been studied by

high-resolution X-ray photoelectron spectroscopy (HR-XPS), normal-incidence X-ray standing wave (NIXSW) measurements and low-energy electron diffraction (LEED). In addition, a possible impact of molecular distortions on interface energetics has been measured by ultraviolet photoelectron spectroscopy (UPS).

4.2 Homomolecular Systems: P4O, PTCDI, F_{16}CuPc on Au(111)

We start to characterize the P4O, PTCDI and F_{16}CuPc monolayers on Au(111), as determined by UPS, XPS, XSW and LEED.

4.2.1 Photoelectron properties

As determined by LEED (Fig. 4.1a-c), the in-plane structure of P4O, PTCDI and F_{16}CuPc monolayers on Au(111) are shown, with additional simulation results of LEED below. The measurements show pronounced diffraction patterns stemming from the adsorbates. The three surface unit cells (parameters in Tab. 4.1) are hexagonal and in good agreement with previous studies [26, 211, 212]. From these, we can conclude that molecules are essentially lying down on the surface.

The chemical analysis by HR-XPS is shown in Fig. 4.1(d). The two peaks in the C core-level spectrum of P4O on Au(111) are labelled as C-C (284.34 eV) and C=O (287.05 eV), as in previously reported results [97]. Similarly, the C 1s spectrum of the PTCDI (Fig. 1e) monolayer allows one to distinguish two peaks, defined as C-C (perylene core) located at the BE of 284.24 eV and C=O (functional group) at a BE of 287.35 eV, with a small shake-up satellite located at higher BE. In the case of F_{16}CuPc, the C 1s core-level shows three distinct peaks, which appear at binding energies of 284.50 eV, 285.62 eV and 286.66 eV and are assigned to carbon atoms bound to carbon (C-C), nitrogen (C-N) and fluorine (C-F) atoms, respectively [167, 201, 213]. The peak located at the lowest BE (283.89 eV) is attributed to a small portion of carbon atoms bound to the substrate (C-Au) due to broken C-F bonds [206] while the shoulder (two grey peaks) at higher BE corresponds to shake up satellites [26, 214]. The relative chemical shifts of all three peaks correspond to F_{16}CuPc in multilayers on polycrystalline Au [167], which indicates physisorption of F_{16}CuPc on the Au(111) surface. The assignment is done following the molecular stoichiometry and is in line with previous studies [215, 216]. Importantly, the

relative BE positions of the three carbon species can be used as criterion to fit the bilayer core-level spectra.

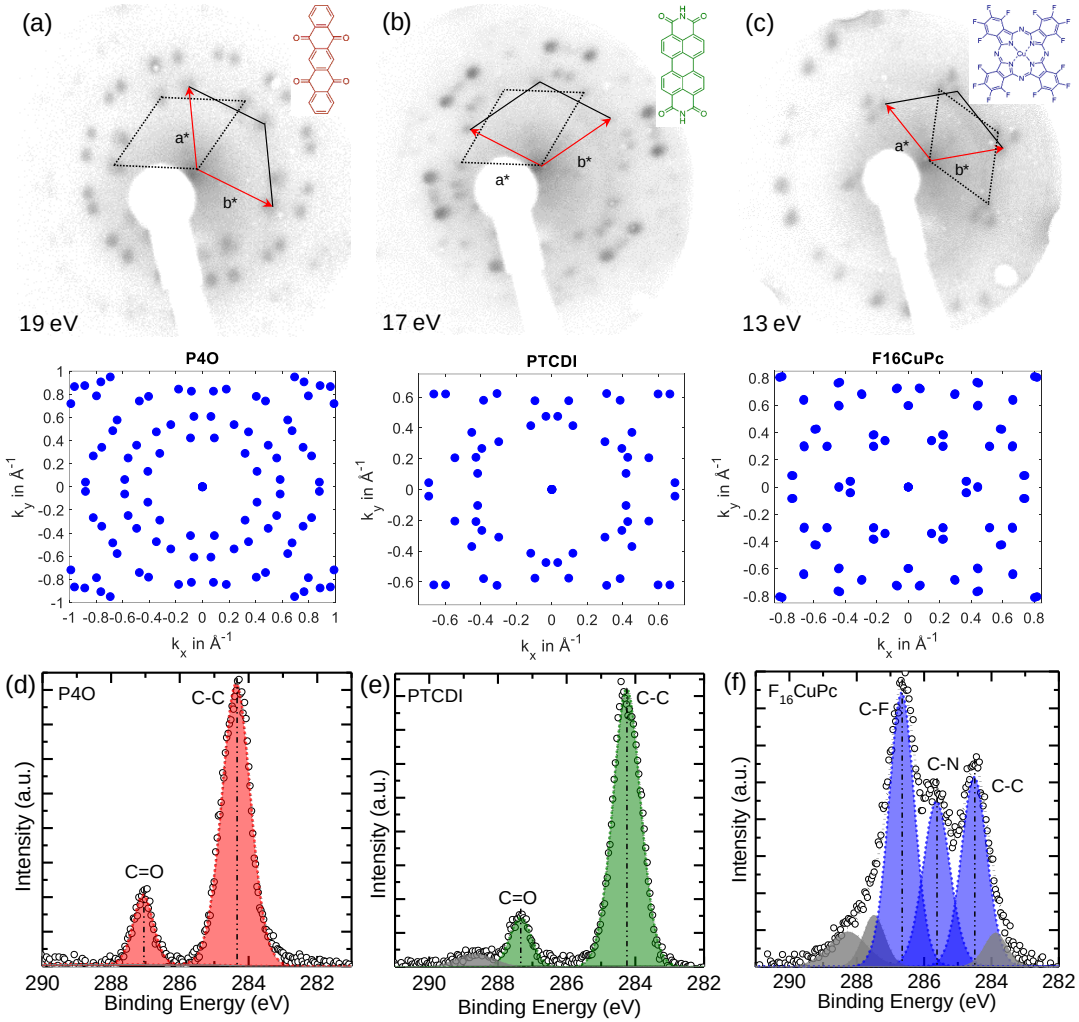

Figure 4.1: LEED patterns (electron energies included) for 1 monolayer (~ 4 Å) (a) P4O, (b) PTCDI and (c) F_{16}CuPc on Au(111), respectively. Simulated (LEEDpat [183]) LEED patterns, while P4O, PTCDI and F_{16}CuPc on Au(111) are shown orderly. The unit cell is superimposed in each LEED pattern while the one with red arrows separates two different unit cells in one pattern. HR-XPS measurements of C 1s core-level spectra of (sub)monolayer P4O (d), PTCDI (e) and F_{16}CuPc (f).

Table 4.1: Lattice parameters (in Å) of the hexagonal unit cells on Au(111) in monolayers, as deduced from the LEED patterns.

/ Å	P4O	PTCDI	F_{16}CuPc
a (Å)	15.5 ± 0.1	15.8 ± 0.1	18.4 ± 0.1
b (Å)	15.7 ± 0.1	16.0 ± 0.1	18.3 ± 0.1
angle (°)	120.5	119.2	120.3

4.2.2 Adsorption properties

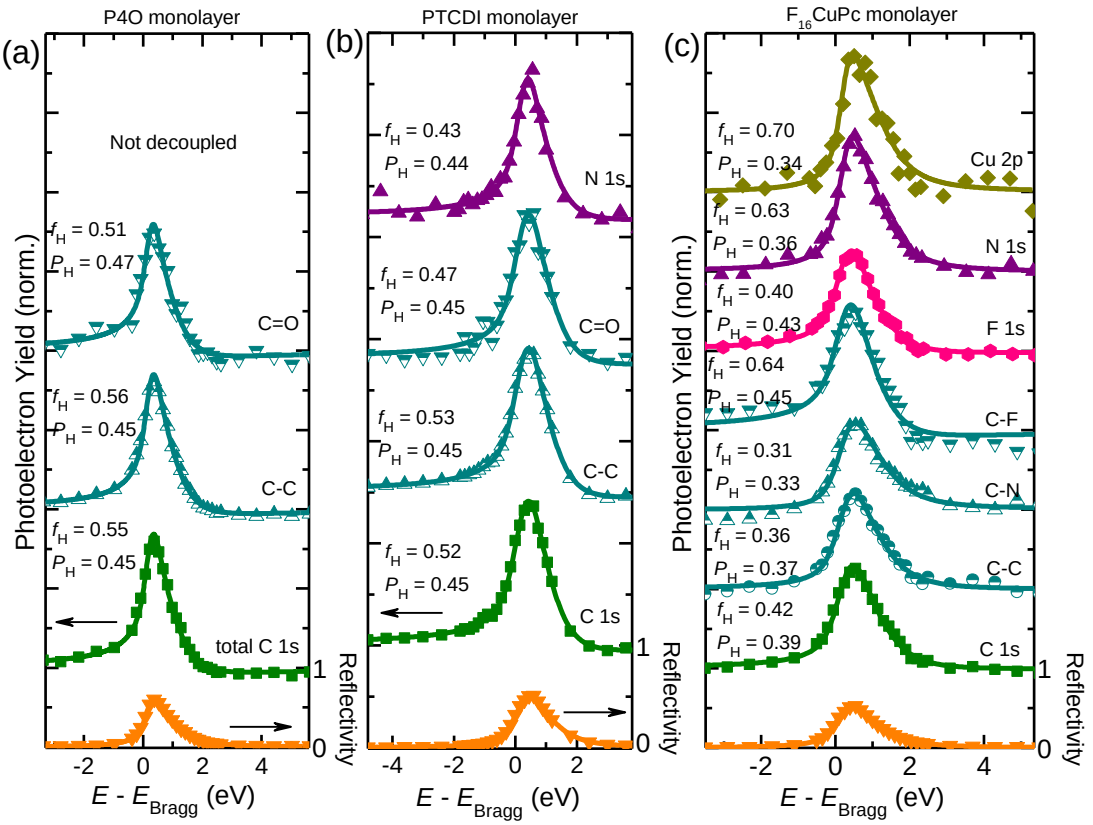

Figure 4.2: XSW results of (sub)monolayer P4O / Au(111) (a), PTCDI / Au(111) (b) and F_{16}CuPc / Au(111) (c), different carbon species and total photoelectron yield are shown, respectively. All carbon species the molecule can be distinguished and successfully analyzed, namely "C-C", "C=O", "C-N" and "C-F" while "C 1s" refers to the total photoelectron yield combining all of them together. The information of other elements in F_{16}CuPc is shown following the same color-code as in Fig. 4.11.

Having established the spectroscopic features of the core-levels and the in-plane structure of the three different monomolecular systems, we now turn to the vertical adsorption geometry and present the corresponding XSW results, that provide precise adsorption distances (typical precision < 0.05 Å [176]). The analysis of the photoelectron yield Y_P (see supporting information) in the standing wave field, which is generated by the interference of incident and Bragg-diffracted X-ray standing waves, gives the coherent position (P_H) and coherent fraction (f_H). P_H can be used to determine the average vertical adsorption distance (d_H) of the different adsorbate atoms by $d_H = (P_H + n)\,d_0$,[171] with $d_0 = 2.35$ Å being the lattice plane spacing of gold along the [111] direction and n being an integer number [171], that

arises from the periodicity of the standing wave field, which is important to distinguish between the molecules adsorbing in the first layer and those in the second. f_H is a parameter describing the degree of vertical order of the respective adsorbate atoms [26]. Due to the surface relaxation of Au and to obtain ideal adsorption distances, the values were corrected as stated in Ref. [217].

Table 4.2: The adsorption distance of P4O, PTCDI and F_{16}CuPc on Au(111) in Å as derived from XSW measurements according to the relation $d_H = (P_H + n)d_0$. (*) means that the element is not present in the molecule and (-) that the results could not be obtained or decoupled in the analysis. The final adsorption distances were calculated taking into account the surface reconstruction occurring for this substrate [217]. The different carbon species are labeled "C-C", "C-N", "C-F" and "C=O" while "C_{av}" gives the averaged adsorption distance of all carbon atoms within one molecule. Uncertainties are obtained according to different measurements, calculated by standard deviation.

/ Å	C-C	C-N	C-F	C=O	C_{av}	F	N	Cu	O
P4O (2 keV)	3.34 ±0.01	*	*	3.38 ±0.02	3.35 ±0.00	*	*	*	-
P4O (5 keV)	3.26 ±0.00	*	*	-	3.25 ±0.01	*	*	*	3.17 ±0.03
PTCDI	3.33 ±0.01	*	*	3.33 ±0.00	3.33 ±0.01	*	3.34 ±0.01	*	-
F_{16}CuPc	3.16 ±0.00	3.05 ±0.06	3.34 ±0.07	*	3.20 ±0.02	3.30 ±0.02	3.12 ±0.01	3.01 ±0.09	*

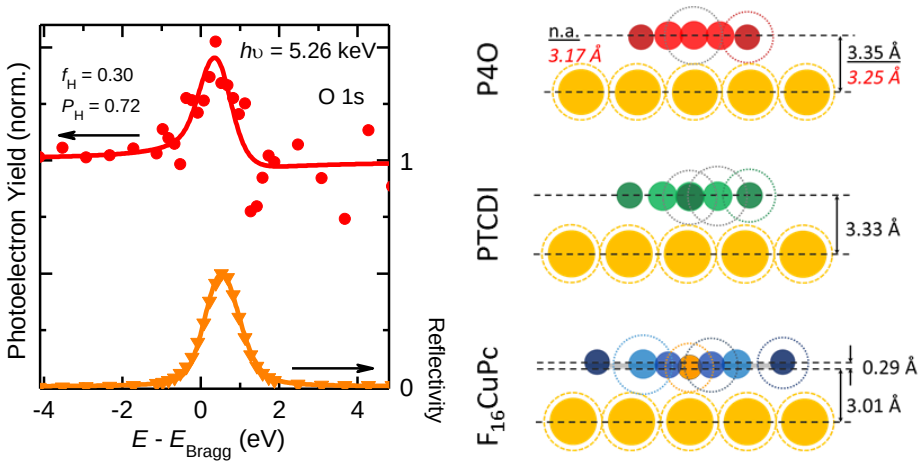

Figure 4.3: XSW measurement of oxygen showing the photoelectron yield and reflectivity for a P4O monolayer on Au(111). The XPS spectra were taken close to the (222) Bragg energy of Au, i.e. around $E_{Bragg} = 5.266$ keV. Sketch of the vertical adsorption geometries of P4O, PTCDI and F_{16}CuPc on Au(111) (in Å) as inferred from the XSW measurements (Fig. 4.2 and Tab. 4.2). Note that for P4O / Au(111) the black numbers correspond to $E_{Bragg} = 2.635$ keV and the red numbers to 5.266 keV. Elements with dashed lines are drawn according to their van der Waals radii. The displayed adsorption distances were calculated taking into account the surface reconstruction observed on gold surfaces [217].

The complete XSW data analysis of the homomolecular systems P4O, PTCDI and F_{16}CuPc on Au(111), which is based on the HR-XPS fitting model discussed in Fig. 4.1, is displayed in Fig. 4.2. As shown in Fig. 4.3, also the adsorption distance of the oxygen atoms in P4O have been measured using the (222) Bragg reflection of gold (photon-energy range 5266 ± 4.5 eV) to avoid the overlapping gold Auger peak [55], which is encountered for the (111) reflection (Fig. 4.2a). The downside of using the higher order reflections is that fewer photoelectrons are generated, thus leading to weaker and noisier signals. To account for this, a larger error of ~ 0.1 Å is associated with the adsorption distances. By applying the equation for P_H, we determine the adsorption distance as $d_H = 3.17$ Å [171]. When using the (111) Bragg reflection of Au (2.64 keV), it is only possible to measure the adsorption distance of carbon atoms in P4O, for which we distinguish two carbon species, one bound to another carbon atom (3.34 Å) and the one bound to an oxygen atom (3.38 Å). In Fig. 4.3, the adsorption geometry, including d_H, of the three molecules on Au(111) is shown. Because of the high-quality XSW data and the core-level fitting model employed, the

adsorption distance of different inequivalent species within the same core-level signal is accessible (full list of adsorption distances in Tab. 4.2). Monolayers of P4O and PTCDI on the surface remain in a flat-lying configuration with d_H of 3.35 Å and 3.33 Å, i.e. in line with previous studies with only minor differences in PTCDI [55, 97]. The same holds for F_{16}CuPc, it adsorbs flat on the surface with an average adsorption distance of 3.35 Å, similar to the results reported by de Oteyza et. al. [205]. Thanks to the improved set-up at I09 and the state-of-the-art photoelectron spectrometer, we have been able to resolve, in contrast to the previous report, different inequivalent carbon species and nitrogen. Thus, as shown in Fig. 4.3, the central copper ion takes the lowest height (3.01 Å) compared to the other elements [201], i.e. similar to other metal phthalocyanine molecules [198, 218-220]. Influenced by the copper atom, the nitrogen atoms that are bound to it show an intermediate height with respect to the Cu and F atoms, which show the adsorption distance (3.12 Å). Moreover, carbon atoms in different chemical environments show a similar trend, i.e. the carbon atoms in C-F bonds have the largest adsorption distance (3.34 Å) while carbon in C-N bonds are closer to nitrogen itself. Comparing all elements in F_{16}CuPc, we conclude that F_{16}CuPc, which is planar in the gas phase [221, 222], shows a significant distortion on Au(111) as the central Cu atom is located below and F atoms above the average adsorption distance, which was observed for the same molecules on Ag(111) and Cu(111) [201].

4.3 Heteromolecular Systems: F_{16}CuPc-Bilayers

Having a detailed picture of the three monomolecular systems on Au(111), including their in-plane and vertical geometry as well as their electronic properties, we now proceed to the heteromolecular bilayer structures. For the heterostructures, F_{16}CuPc was vacuum-sublimed on monolayers of P4O and PTCDI. For the UPS and XPS measurements, the nominal thickness of the template layer has been as close to monolayer coverage as possible and making sure that it does not exceeded one monolayer; for LEED, HR-XPS and XSW measurements these monolayers have been prepared by thermal desorption of multilayers.

4.3.1 Photoelectron properties

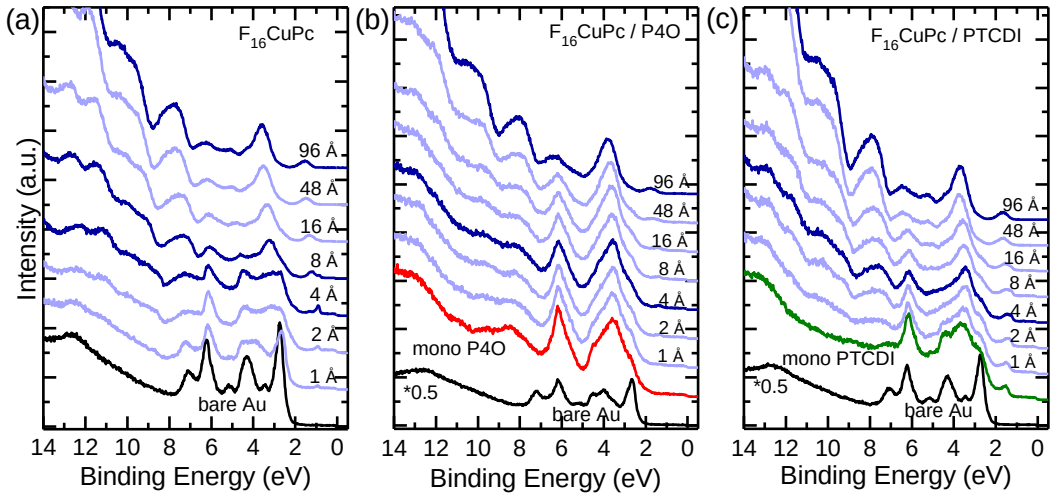

Figure 4.4: Full UP spectra collected at 45° emission for the stepwise deposited COMs on Au(111). (a) Pure F_{16}CuPc grown on Au(111) with the mono- and multi-layer spectra highlighted by darker lines. UP spectra of F_{16}CuPc deposited on a monolayer of P4O / Au(111) (b), PTCDI / Au(111) (c). For the heterostructures the nominal mono- (4 Å) and multi- (96 Å) layer thickness of F_{16}CuPc spectra are indicated.

Prior to discussing the coverage-dependent evolution of the valence-electron region spectra of the bilayers, full UP spectra and zoom in spectra of F_{16}CuPc, F_{16}CuPc / P4O and F_{16}CuPc / PTCDI have been shown in Fig. 4.4 and Fig. 4.5. In Fig. 4.4(a), bare Au(111) displays a gold 5d-band characteristic feature among 2-8 eV. With F_{16}CuPc deposition, gold features submerged gradually, while F_{16}CuPc features started. Notably, in the valence region, intense photoelectron features in the BE range of 9-12 eV can be seen, as well as the bilayer spectra (Fig. 4.4b and c), which are known as molecular orbitals that strongly involve fluorine atoms [150]. The UPS survey spectra also confirm that the penetration depth of this technique is approximately 10 Å, deeper adsorbate cannot be observed [223, 224]. With the deposition of F_{16}CuPc, the intensity of the substrate-derived Fermi edge is attenuated and characteristic peaks of F_{16}CuPc appear (Fig. 4.4a and Fig. 4.5): the highest occupied molecular orbital (HOMO)-derived peak centered at 0.90 eV (for submono- and mono- layer thickness). The intensity of this peak becomes strongest at the nominal monolayer coverage (4 Å), and increasing the coverage leads to an attenuation of this feature due to the limited probing depth of UPS. For an F_{16}CuPc

monolayer thickness, a new feature appears at higher BE (~ 1.31 eV) close to the monolayer HOMO peak, which apparently splits into two peaks. The fine-structure of the splitting, which can only be observed for a thickness corresponding to a mono- (4 Å) and bi- (8 Å) layer, could be explained by considering the formation of dimers, a phenomenon that has been observed for PbPc on HOPG as well [220]. Further experiments will be required to verify this hypothesis in general.

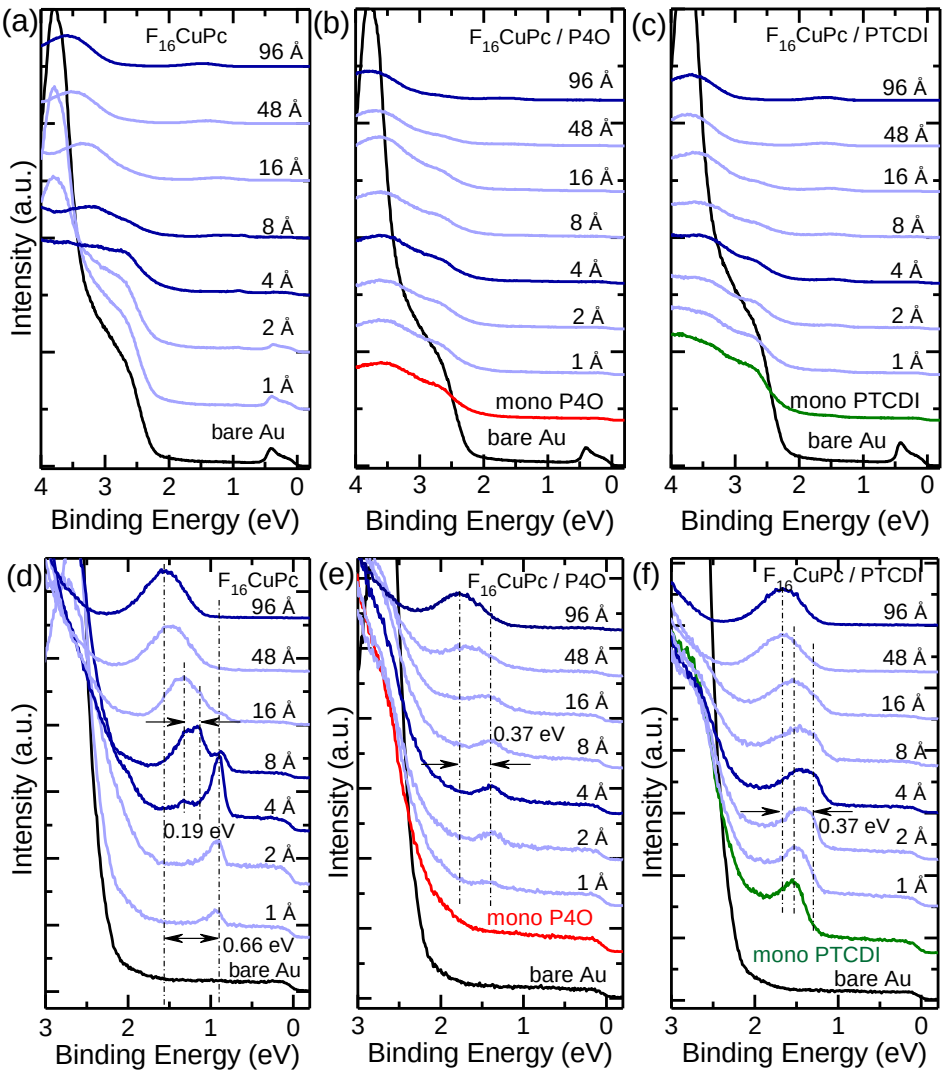

Figure 4.5: Zoom in UP spectra for the stepwise deposited COMs on Au(111), (a-c) were recorded at normal incidence and (d-f) at 45° emission. (a, d) Pure F_{16}CuPc grown on Au(111) with the mono- and multi-layer spectra highlighted by darker lines. UP spectra of F_{16}CuPc deposited on a monolayer of P4O / Au(111) (b, e), PTCDI / Au(111) (c, f). For the heterostructures the nominal mono- (4 Å) and multi- (96 Å) layer thickness of F_{16}CuPc spectra are indicated. Vertical lines refer to the position of the HOMO.

Fig. 4.5(b, e) and (c, f) show the coverage-dependent evolution of UP spectra of F_{16}CuPc deposited on Au(111) pre-covered by the two adlayers (P4O and PTCDI). For the F_{16}CuPc / P4O bilayer (Fig. 4.5b, Fig. 4.5e), i.e. with a P4O monolayer on Au, because of the gold d-band at a low binding energy (~ 2 eV), the HOMO peak of P4O is disturbed by the Au features. The HOMO-derived peak of F_{16}CuPc, located at a BE of 1.40 eV at one monolayer thickness (4 Å), gradually emerges with increasing coverage. It shifts by 0.37 eV towards higher BE with further F_{16}CuPc deposition as expected due to the reduced photo hole screening by the substrate [97]. This is in line with F_{16}CuPc and P4O forming a bilayer system on Au(111) as the VB features of F_{16}CuPc are different from those in Fig. 4.5(a), indicating that the molecules are not in contact with the substrate. The HOMO peak shift of F_{16}CuPc is found to be similar for deposition on the PTCDI-monolayer. Here, the F_{16}CuPc HOMO peak features become visible while the PTCDI HOMO signal (1.52 eV in green curve) vanishes. Notably, in this bilayer the HOMO position of F_{16}CuPc also shifts by 0.37 eV with further deposition of F_{16}CuPc, i.e. by the same amount as for the P4O interlayer on Au(111).

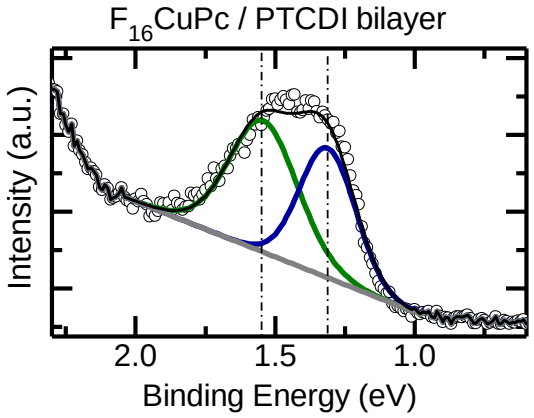

Figure 4.6: Fitting of the UP spectrum of the F_{16}CuPc / PTCDI bilayer on Au(111). The spectrum is taken from Fig. 4.5(f) with 4 Å F_{16}CuPc deposited on Au(111) pre-covered by a monolayer PTCDI. The blue curve belongs to the F_{16}CuPc HOMO peak, while the green curve is the PTCDI signal with their HOMO position at 1.31 eV and 1.55 eV, in agreement with the discussion in the main text.

Notably, a possible fitting on HOMO peaks of F_{16}CuPc / PTCDI bilayer on Au(111) can be accessed (Fig. 4.6), using the similar method as the fitting mode applied on

XPS core-level spectra. Adapted by mono-PTCDI and mono-F_{16}CuPc valence band spectra, the curve generated by monolayer F_{16}CuPc on Au(111) which is pre-covered by monolayer PTCDI can be distinguished by two different contributions. The blue curve belongs to the F_{16}CuPc HOMO peak, while the green curve is the PTCDI signal with their HOMO position at 1.31 eV and 1.55 eV, in agreement with the discussion in the bilayer regime (Fig. 4.5d and Ref. [55]). In this figure, F_{16}CuPc shows a HOMO peak which arises from the monolayer system which the HOMO peak of PTCDI belong to its multilayer signal, proving again the ordered bilayer growth mode.

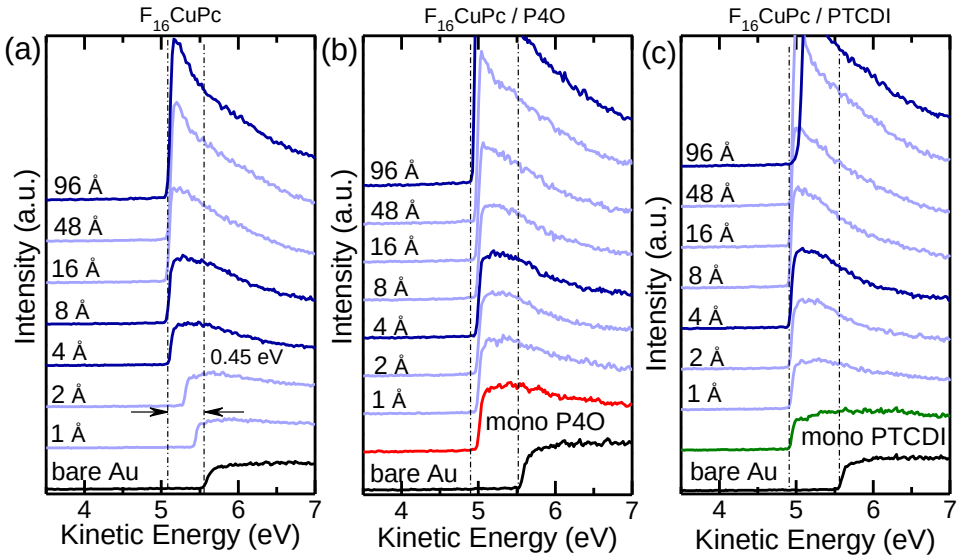

Figure 4.7: Thickness-dependent secondary-electron cutoff (SECO) region of F_{16}CuPc, F_{16}CuPc / P4O and F_{16}CuPc / PTCDI on Au(111), respectively. Monolayer of the insertion molecules (P4O or PTCDI) is colored by red and green, in accordance with the color code in main text.

The secondary-electron cutoff (SECO) spectra were carried out with a biased voltage of -3 V, and the plot was calculated to kinetic energy (Fig. 4.7). The work function (WF) or vacuum level (VL) can be determined by SECO spectra. Following the same order as the valence band spectra, we can figure out the stepwise WF with different thickness of F_{16}CuPc on Au(111) (Fig. 4.7a), mono-P4O / Au(111) (Fig. 4.7b) and mono-PTCDI / Au(111) (Fig. 4.7c). As shown in Fig. 4.7(a), the WF of clean gold substrate is about 5.55 eV, in agreement with the previous studies [199, 200]. With the deposition of F_{16}CuPc, the work function is shifted to lower kinetic energy by ~0.48 eV. According to the spectra, we find that the WF is mainly shifted with the

thickness of 4 Å (a nominal monolayer), and contains stable with further deposition. In Fig. 4.7(b), with monolayer P4O adsorbed on Au(111), the WF is shifted by 0.56 eV and has been shifted slightly with F_{16}CuPc deposition, meaning that F_{16}CuPc only has weak influence on this bilayer. The situation in F_{16}CuPc / PTCDI bilayer is similar as F_{16}CuPc / P4O, while PTCDI dominates most of the shift on WF and further F_{16}CuPc maintains unchanged.

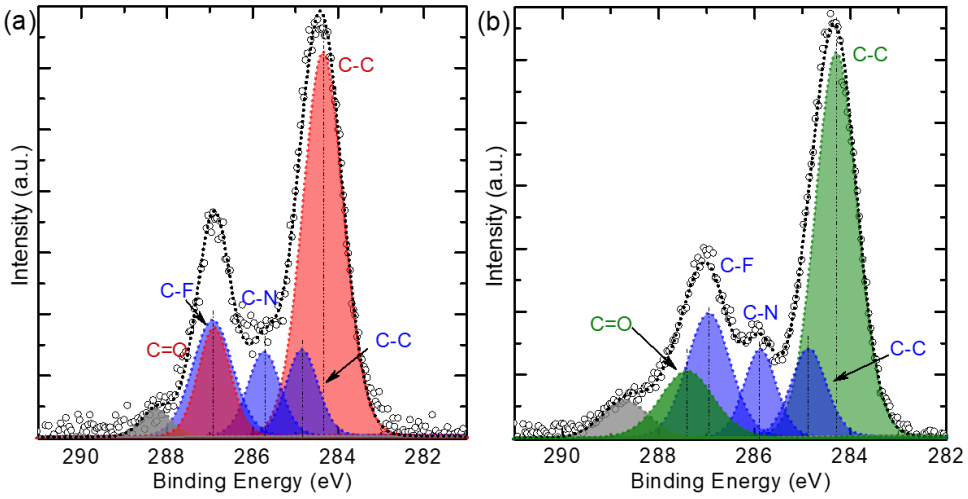

Figure 4.8: HR-XPS measurements of C 1s core-level spectra for bilayer systems of F_{16}CuPc / P4O (a) and F_{16}CuPc / PTCDI (b) on Au(111). Spectra are taken with $h\upsilon$ = 800 eV. The monolayers of the template molecule were prepared by desorption, then a monolayer F_{16}CuPc was deposited on top. The color-code is adapted from Fig. 4.1. Red areas belong to P4O, green areas belong to PTCDI and blue areas indicate the F_{16}CuPc contribution.

Adapting the fitting model from Fig. 4.1, we analyze the C 1s core-levels of a (sub)monolayer F_{16}CuPc on Au(111) pre-covered by a monolayer of P4O (Fig. 4.8a) and PTCDI (Fig. 4.8b). In Fig. 4.8(a), the C-C and C=O peaks of P4O (red areas) are visible with a BE difference of 2.54 eV which is identical to the monolayer spectra of P4O on Au(111) (Fig. 4.1e). Meanwhile, the C signals attributed to F_{16}CuPc (blue areas) prevail with similar BE shifts for each species compared to Fig. 4.1(f), i.e. the C-N (C-F) component is found at 0.91 eV (2.12 eV) higher BE than C-C. The residual area at ~288 eV most likely corresponds to a shake-up peak. The results in Fig. 4.8(b) demonstrate that all components related to PTCDI (green areas) and F_{16}CuPc (blue areas) occur at BE positions, which agree with the monolayer fitting results.

Specifically, the two carbon species of PTCDI exhibit a BE difference of 3.11 eV, and the carbon peaks of F_{16}CuPc are distributed as they are in Fig. 4.1(f) and Fig. 4.8(a). For comparison, the XPS core-level spectra of F_{16}CuPc mono- (~4 Å) and multi- (~96 Å) layers on the pre-covered Au(111) are shown in Fig. 4.9.

The results in Fig. 4.9 were performed in Soochow University, with the collaboration with Prof. Duhm, while the set-up is different from that in DLS (Fig. 3.20). In Fig. 4.9, F_{16}CuPc / P4O and F_{16}CuPc / PTCDI have been displayed at the bottom of Fig. 4.9(a) and (b), while multilayer F_{16}CuPc on monolayer P4O (PTCDI) are shown on the top. The same results of both bilayer systems are determined, with almost identical fitting mode, that different carbon species in each molecule are distinguishable. When the thickness of F_{16}CuPc goes to 96 Å (a nominal multilayer), the C signal is still visible in the P4O-bilayer system with comparably lower intensity. However, with a monolayer PTCDI in between Au and multi-F_{16}CuPc, its signals are submerged by thicker F_{16}CuPc film. The results of multilayer F_{16}CuPc on top of P4O / Au(111) and PTCDI / Au(111) are more complicated to have deeper explanation, therefore we refuse to give more discussion.

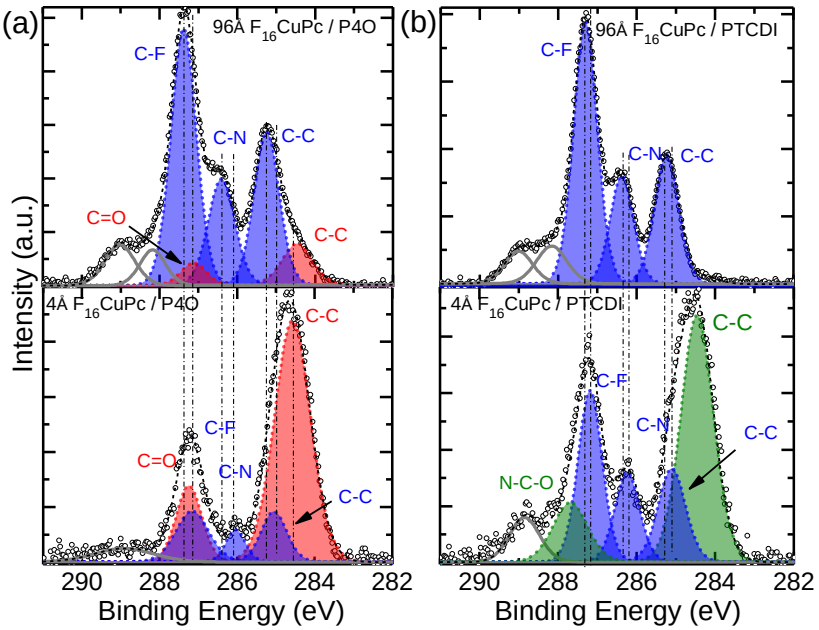

Figure 4.9: XPS measurement of C 1s core-level spectra in the bilayer (heterostructure) systems. (a) The nominal coverages are 4 Å (mono-) and 96 Å (multi-) of F_{16}CuPc on 4 Å P4O or PTCDI on Au(111).

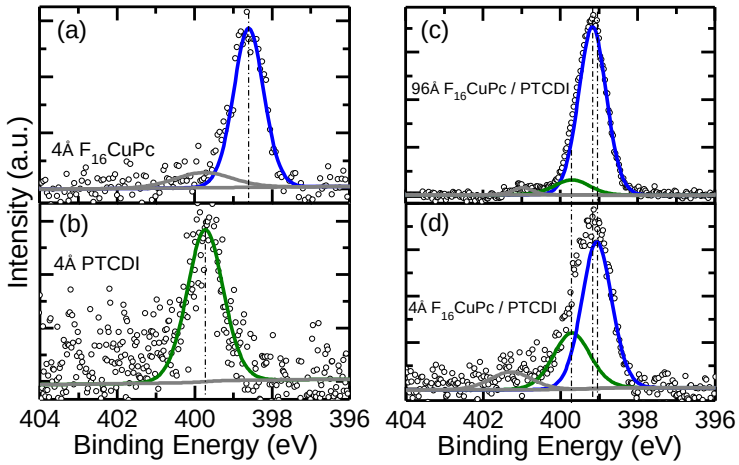

Figure 4.10: XPS measurements of N 1s core-level spectra for monolayer $F_{16}CuPc$ (a), PTCDI (b), multilayer $F_{16}CuPc$ / mono-PTCDI (c), and monolayer of $F_{16}CuPc$ / mono-PTCDI (d) on Au(111). Spectra are recorded with $h\upsilon$ = 1486.6 eV, by a monochromatized Al Kα source.

Beside the C 1s core-level spectra, N 1s core-level spectra is recorded at the same time, as shown in Fig. 4.10. We have shown nitrogen signal from monolayer (4 Å) $F_{16}CuPc$, monolayer PTCDI, $F_{16}CuPc$ / PTCDI bilayer (both molecules have the thickness of 4 Å) and multilayer $F_{16}CuPc$ on mono-PTCDI / Au(111). The N 1s signal of $F_{16}CuPc$ (Fig. 4.10a) and PTCDI (Fig. 4.10b) give us the standard fitting mode to figure out different nitrogen contributions in both molecules in the bilayer system, as shown in Fig. 4.10, with N 1s in $F_{16}CuPc$ located at the BE of 389.59 eV and 399.74 eV in PTCDI. According to the monolayer results, the nitrogen curve of bilayer can be fitted as well, see Fig. 4.10(c, d). In Fig. 4.10(d), the blue curve located at the BE of 399.03 eV is attributed to $F_{16}CuPc$ molecules, and the green curve at 399.73 eV is attributed to PTCDI molecules, showing similar phenomenon as both in monolayer systems. In Fig. 4.10(c), the PTCDI contribution remains the same as noted by the dashed line while the blue curve ($F_{16}CuPc$ contribution) has been shifted slightly to 399.15 eV, which is due to different chemical environment with multilayer (96 Å) $F_{16}CuPc$ deposited on the top.

4.3.2 Adsorption properties

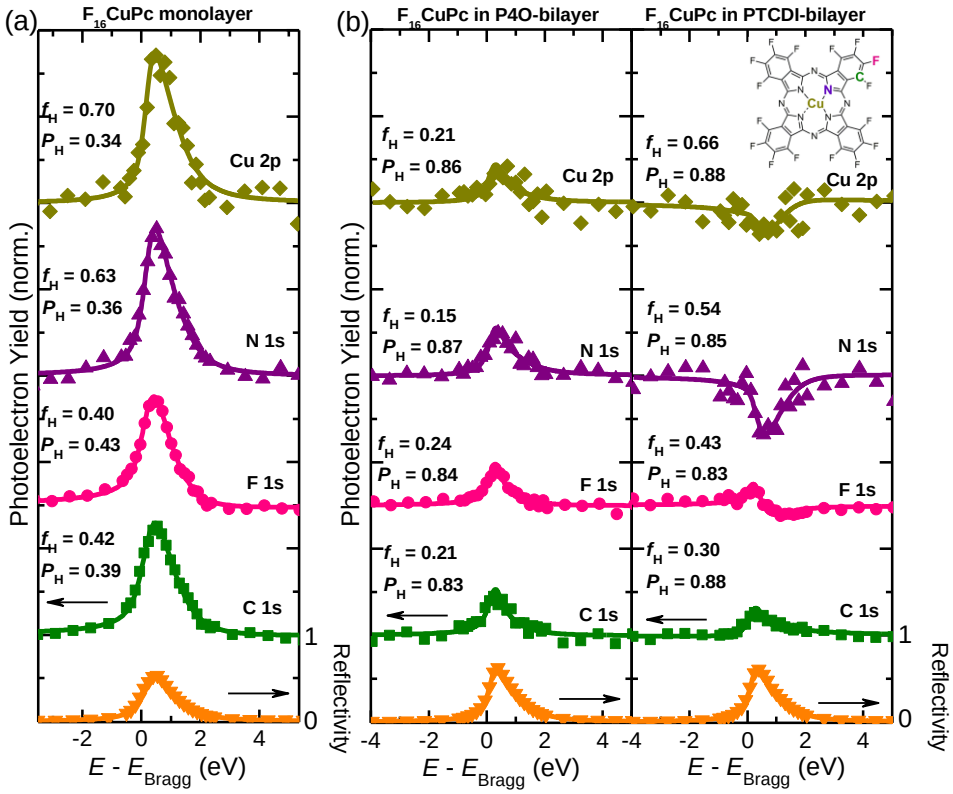

Figure 4.11: XSW measurements for an $F_{16}CuPc$ (sub)monolayer directly adsorbed on Au(111) (a), on top of a P4O (b) and PTCDI (c) monolayer, both on the same substrate. The inset describes the color code of different components in $F_{16}CuPc$.

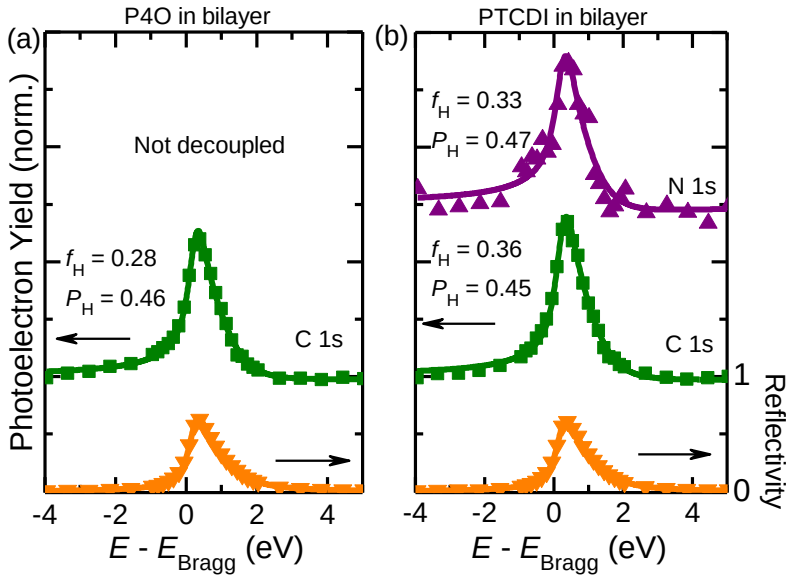

Figure 4.12: XSW measurements for an $F_{16}CuPc$ (sub)monolayer adsorbed on top of a P4O (a) and PTCDI (b) monolayer, both on Au(111).

After the investigation of the chemical properties by XPS, the adsorption distances were measured using the XSW technique. The photoelectron yield Y_P (E-E_{Bragg}) and corresponding fits for F_{16}CuPc in mono- and bi- layers together with the corresponding least-square fits are displayed in Fig. 4.11 and Fig. 4.12. Details for all F_{16}CuPc signals have been measured and the corresponding element-specific results are summarized in Tab. 4.3. After F_{16}CuPc deposition on the P4O-adlayer, the P4O molecules remain within the error bars at the same height as before adding the second layer, i.e. at 3.38 Å (vs. 3.34 Å). The Cu and N atoms of F_{16}CuPc are found to be about 3.3 Å above P4O, i.e. at similar intermolecular distances as CuPc / P4O [26] on Ag(111). The F and C atoms are found to be slightly closer to the P4O molecules with a difference of 0.11 Å, which indicates a soft bending of the molecule in the second layer.

Table 4.3: The adsorption distance d_H of F_{16}CuPc / P4O and F_{16}CuPc / PTCDI bilayers on Au(111) determined by XSW measurements according to the relation $d_H = (P_H + n)\,d_0$. Uncertainties are obtained according to different measurements, calculated by standard deviation.

	F_{16}CuPc/P4O/Au(111)					F_{16}CuPc/PTCDI/Au(111)			
/ Å	C_{av}	F	N	Cu	/ Å	C_{av}	F	N	Cu
F_{16}CuPc	6.51 ±0.06	6.56 ±0.03	6.71 ±0.02	6.67 ±0.08	F_{16}CuPc	6.69 ±0.02	6.61 ±0.01	6.67 ±0.02	6.74 ±0.03
P4O	3.38 ±0.01	*	*	*	PTCDI	3.33 ±0.01	*	3.43 ±0.03	*

For the PTCDI-bilayer system, we find that the adsorption geometry of the PTCDI interlayer changes upon deposition of F_{16}CuPc. Initially, PTCDI monolayers on Au(111) are essentially planar, i.e. with its two carbon species and nitrogen atom at identical adsorption distances. According to the XSW data analysis, we find that the C atoms in PTCDI remain at the adsorption distance of the monolayer system. In contrast, the N atoms are located at an adsorption distance of 3.43 Å, which is 0.10 Å higher than the C atoms. This significant difference between C and N in PTCDI means that the initially flat molecule is bent due to the interaction with F_{16}CuPc molecules in the second layer (see Fig. 4.12 and Tab. 4.3). The Cu atoms are found 3.41 Å above the C atoms of PTCDI, whereas the F atoms are only 3.28 Å above, which

is similar to the adsorption distance differences of CuPc and PTCDA [72] on Ag(111). Thus, the adsorption geometry of F_{16}CuPc is qualitatively similar to the P4O-bilayer with a spread of 0.13 Å within the molecule.

As discussed above, F_{16}CuPc shows a slightly distorted structure when adsorbed on Au(111) with the Cu atom located at the lowest and F atoms at the highest position. According to the XSW measurements, it adsorbs with an inverted intramolecular distortion (~ 0.1 Å) on top of both intermediate layers, compared to the F_{16}CuPc monolayer on Au ($\Delta d_H = 0.29$ Å). Considering the carbon backbones of both bilayer systems, the distance Δd_H between F_{16}CuPc and the adlayers are 3.13 Å (P4O-bilayer) and 3.36 Å (PTCDI-bilayer). There are differences between the coherent fractions of both systems as well. F16CuPc on PTCDI shows values very similar to the monolayer case, whereas on P4O, the f_H for the different elements is reduced. This could be explained by the different packing of PTCDI and P4O on Au(111), which induces a different degree of disorder in the second layer. Overall, the adsorption geometry of F_{16}CuPc in the bilayers is found to be significantly different compared to the distorted structure of the monolayer on Au(111), i.e. in the bilayer F_{16}CuPc molecules show an inverted intramolecular distortion due to the insertion of the first layer.

4.4 Discussion

The vacuum level (VL) position with increasing film coverage (Fig. 4.13) provides further insight into the interfacial interaction strength at the F_{16}CuPc / Au(111) and F_{16}CuPc / P4O (PTCDI) interface and the morphology of the thin films [120, 225]. From Fig. 4.13, we found that in all cases, the work function of clean Au(111) is ~5.55 eV. Upon initial deposition of PTCDI and P4O, the vacuum level shows a steep decrease (~0.60 eV), which almost saturates at a nominal coverage of 4 Å and stays essentially constant for higher coverages. The situation of F_{16}CuPc / Au(111) is similar to PTCDI and P4O, while its ΔVL is about 0.45 eV with a coverage of 4 Å. This behavior confirms flat-lying molecules in the monolayer and predominate multilayer growth for thicknesses larger than 4 Å. For these molecules,

as has been proved to be physisorbed on Au(111), the vacuum level shift is mainly ascribed as push-back effect [226].

Deposition of F_{16}CuPc on P4O / Au(111) and PTCDI / Au(111) does not result in notable changes of the VL because of the weak coupling at these interfaces. However, a more comprehensive discussion combining the results of various experimental methods is followed to indicate reasons of the vacuum level shift.

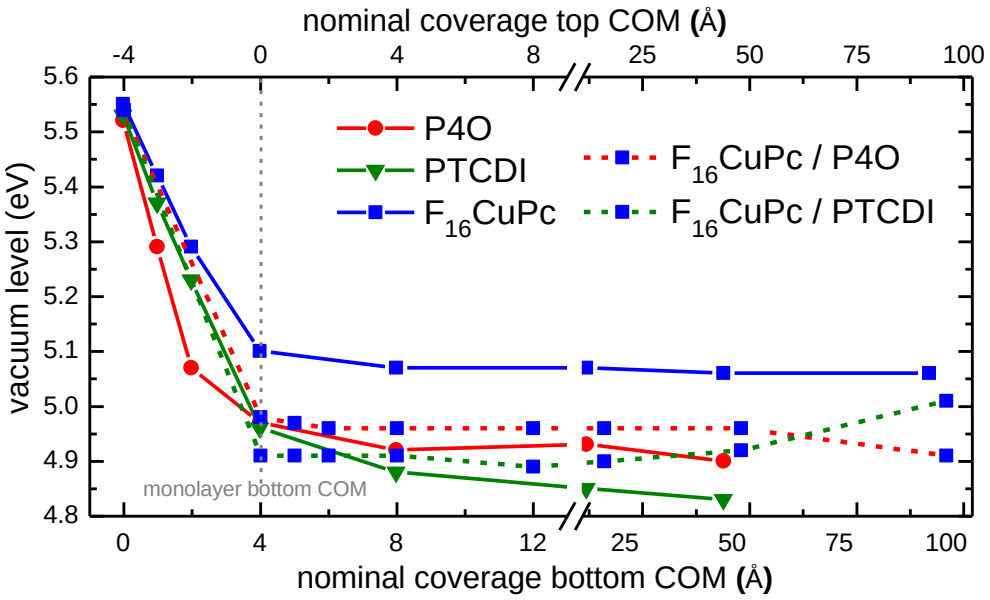

Figure 4.13: Coverage-dependent evolution of the vacuum level with respect to the corresponding Fermi level for all investigated thin films on Au(111), some are determined from Fig. 4.7. PTCDI data are taken from Ref. [55]. "Bottom" and "top" COM denote the deposition sequence of the thin films. The solid lines correspond to the monomolecular systems and are referred to the bottom abscissa. The dashed lines describe the heteromolecular systems created upon the deposition of increasing coverages of F_{16}CuPc (referred to the top abscissa) on a full monolayer of P4O (red) and PTCDI (green).

F_{16}CuPc Monolayer: The results of the present paper are schematically summarized in Fig. 4.14, including the adsorption geometry, i.e. with the element-specific bonding distances of the F_{16}CuPc monolayer and bilayers as they were determined by XSW measurements. In addition, the energy level diagram derived by UPS is displayed at the bottom. By combining these results, we can draw a picture of the F_{16}CuPc monolayer system as it has been discussed. The vacuum level (VL) (details see Fig. 4.7 and Fig. 4.13) position with increasing film coverage (Fig. 4.7)

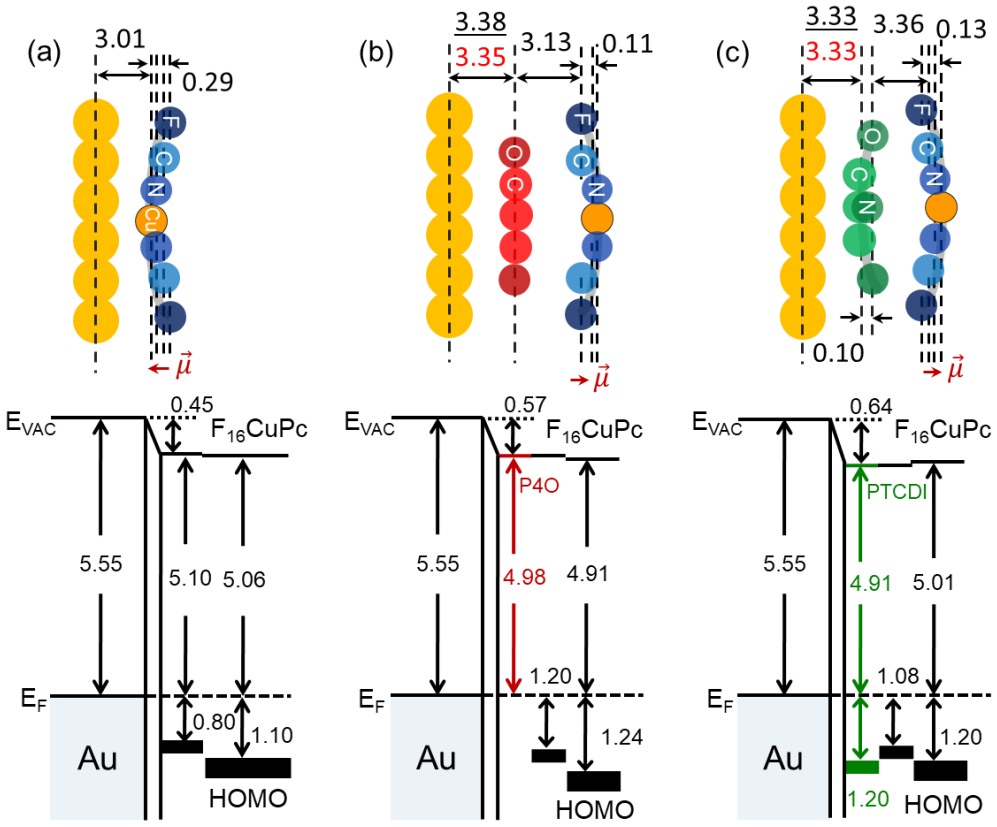

Figure 4.14: Adsorption geometries $F_{16}CuPc$ (a), $F_{16}CuPc$ / P4O (b) and $F_{16}CuPc$ / PTCDI (c) on Au(111). In Fig. 6(b) and (c), black values indicate bilayer systems and red values (bottom) are from the monolayer systems for comparison. Real adsorption distances were calculated considering the surface reconstruction of Au(111) [217]. Energy-level diagram of the three organic-metal interfaces are determined by UPS measurements.

provides further insight into the interaction strength for the mono- and hetero-molecular interfaces [120, 199, 200]. Fig. 4.14(a) illustrates the distorted adsorption geometry of $F_{16}CuPc$ with the copper atom at the lowest distance and fluorine atoms being 0.29 Å higher. Upon initial deposition of $F_{16}CuPc$, the vacuum level shows a steep decrease ($\Delta VL = 0.45$ eV), which nearly saturates at monolayer coverage (Fig. 4.7 and Fig. 4.13). This behavior confirms flat-lying molecules in the monolayer and also multilayer growth regime. The observed VL shifts can be explained to a large extent by Pauli repulsion. However, the distortion of this molecule according to XSW results and the corresponding dipole moment ($\vec{\mu}$) needs to be taken into account for a complete picture of the adsorption behavior and energy levels. In general, vacuum level shifts ΔVL at organic-metal interfaces can have two contributions [22, 198]:

$$\Delta VL = \Delta\Phi_{dip} + \Delta\Phi_{bond}$$

In this equation, $\Delta\Phi_{bond}$ contains the effect of the molecule-metal interaction, which is mainly caused by Pauli repulsion for the weakly interacting F_{16}CuPc / Au(111). The other contribution $\Delta\Phi_{dip}$ is proportional to the distortion-induced dipole moment ($\vec{\mu}$) [227] shown in Fig. 4.14(a). It is because fluorine atoms with negative partial charge take an adsorption distance, which is 0.29 Å higher than that of copper atoms with their positive partial charge. For F_{16}CuPc monolayers on Au(111), the observed ΔVL can be ascribed to the combination of the molecular dipole moment [22, 198] and the push-back effect (with ΔVL increasing for decreasing adsorption distance [99, 228]) [225, 226].

F_{16}CuPc Bilayers: Within the P4O-derived bilayer (Fig. 4.14b), the P4O molecules virtually remain at the same adsorption distance as in the monolayer system (3.35 Å vs 3.38 Å). More importantly, F_{16}CuPc on P4O adsorbs in the geometry with Cu and N atoms repelled by ~ 0.11 Å relative to the C and F atoms. This is in contrast to the strong upward bending of F atoms in F_{16}CuPc-monolayers on Au(111). It can be speculated that the repulsive interaction of the F atoms with the Au(111) substrate is weakened by the template layer. The lack of interaction between P4O and F_{16}CuPc is further supported by the absence of a notable vacuum-level shift, while the slight vacuum-level shift (~0.10 eV) at this interface can be ascribed to the distortion of F_{16}CuPc itself. A similar behavior is found for the PTCDI / F_{16}CuPc bilayer, where the VL is lowered by a monolayer of PTCDI on Au(111) and deposition of F_{16}CuPc on top causes no further VL change at low coverages (only 0.10 eV for thicker films). The XSW results give evidence of the weak coupling between F_{16}CuPc and PTCDI. With F_{16}CuPc deposited to form the bilayer, the planar PTCDI molecule is slightly bent with its nitrogen atoms closer to the F_{16}CuPc molecule, while F_{16}CuPc shows more of the inverse bending (0.13 Å) as it was found for the P4O-derived bilayer. Apart from that, in both bilayers, differences between the highest adsorbed element in the first layer and the lowest adsorbed element in the second layer (F_{16}CuPc) are similar, i.e., 3.13 Å and 3.18 Å, demonstrating again that P4O and PTCDI have a comparable template function for F_{16}CuPc.

4.5 Conclusion

In summary, we have studied the geometric and electronic structure, specifically the adsorption distances and vacuum level shifts, at the organic-organic and organic-metal interfaces of F_{16}CuPc, F_{16}CuPc / P4O and F_{16}CuPc / PTCDI bilayer systems on Au(111). Our measurements have shown that the three molecules are physisorbed on this substrate and that, as expected for weak interactions, the HOMO positions of F_{16}CuPc in the two different bilayer systems are nearly identical. Moreover, the fluorine-upward distorted structure of the F_{16}CuPc monolayer on Au(111) is confirmed by XPS and XSW, together with the support of UPS and LEED. Notably, the advantages of the XSW technique have been used to resolve the adsorption distance of two different layers with an error bar of < 0.1 Å, demonstrating the potential of further investigations on such heterostructures. Therefore, the growth of F_{16}CuPc as the second layer is confirmed by XSW and UPS measurements. For the P4O derived bilayer, the P4O molecules as the bottom layer representing the contact with the substrate remain essentially at the same bonding distances as P4O in monolayers on Au. Deviations, however, occur for the F_{16}CuPc molecules in the second layer with an intramolecular downward distortion. The XSW results reveal that in the F_{16}CuPc / PTCDI bilayer, both molecules show a different adsorption behavior compared to the monolayers. In this bilayer system, there is the upward bending of nitrogen in PTCDI and downward bending of fluorine in F_{16}CuPc, which indicates an attraction between these two materials. An intramolecular distortion of F_{16}CuPc is found for these bilayers, yet with inverted direction compared to the adsorption on metal substrates. Overall, we have shown that also in the physisorptive regime the substrate plays a crucial role for the conformation of adsorbates.

5. PEN-PFP MIXTURES ON AU(111)

This chapter is based on Ref. [148].

As crucial element in organic opto-electronic devices, heterostructures are of pivotal importance. In this context, we present a comprehensive study of the properties on a simplified model system of an organic donor-acceptor (D-A) bilayer structure using ultraviolet photoelectron spectroscopy (UPS), X-ray photoelectron spectroscopy (XPS), low-energy electron diffraction (LEED) and normal-incidence X-ray standing wave (NIXSW) measurements. Pentacene (PEN) as donor material and perfluoropentacene (PFP) as acceptor material are chosen to produce bilayer structures on Au(111) and Cu(111) substrates by sequential monolayer deposition of the two materials. By comparing the adsorption behavior of the PEN/PFP bilayers on weakly and strongly interacting substrates, we find that: i) the adsorption distance of the first layer (PEN or PFP) indicates physisorption on Au(111), ii) the characteristics of the bilayer structure on Au(111) are (almost) independent of the deposition sequence, and hence, iii) in both cases a mixed bilayer is formed on the weakly interacting substrate. This is in striking contrast to PFP/PEN heterostructures on Cu(111), where strong chemisorption pins the PEN molecules to the metal surface and therefore no intermixed bilayer is formed by subsequent PFP deposition. Our results illustrate the strong tendency of PEN and PFP molecules to mix, which *per se* has important implications for the fabrication of PEN/PFP heterojunctions.

5.1 Introduction

Conjugated organic materials (COMs) have received considerable attention due to their potential for the application as active layers in novel (opto-)electronic devices, such as organic light emitting diodes (OLEDs) or organic photovoltaics (OPVs) [18, 229-231]. In particular, interface properties are of importance since they determine charge carrier barriers and the energy level alignment (ELA) between an active material layer and the metal electrode. Template layers between the metal electrode and the active material have been proven to be an efficient way

for engineering interface energetics and tuning energy barriers for charge injection/withdrawal [7, 232-234]. Therefore, the interface between the active molecular layer and the metal substrate plays a crucial role as it is the key component of the organic film and hence will influence the performance in respective applications [26, 56, 235]. As shown in various studies, the coupling strength of the template layer with the substrate, a factor which is crucial for the growth of subsequently deposited organic layers [27, 29, 236, 237], can be quantified through different experimental "indicators", i.e. vacuum-level shifts determined by ultraviolet photoelectron spectroscopy (UPS), core-level shifts determined by X-ray photoelectron spectroscopy (XPS) and bonding distances determined by the X-ray standing waves (XSW) technique [26].

Being an intensively studied p-type semiconductor material, pentacene (PEN, $C_{22}H_{14}$) holds great potential for application in organic electronic devices due to its good processability compared to smaller oligoacenes, and high charge carrier mobilities consistently reported for thin films [200, 238-241]. With regard to the fabrication of bipolar transistors, a corresponding n-type organic semiconductor should have similar physical and structural properties except for the type of charge carriers [28, 242-244]. For that reason, we chose perfluoropentacene (PFP, $C_{22}F_{14}$) [13, 110, 150] as acceptor material and studied the adsorption behavior and coupling strength between the two COMs. Mixed thin films based on this donor-acceptor (D-A) pair have already been studied with optical methods, X-ray diffraction and theoretical methods [215, 242, 245-249]. However, the adsorption of the first layers, in particular vertical bonding distances, have not been measured, also because previous studies mostly used SiO_2 or HOPG as substrates, i.e. inert surfaces with weak interaction and/or limited usability for XSW measurements [128, 149]. Specifically, the XSW technique requires highly ordered and crystalline substrates, for instance, coinage metal single crystals, which can be easily prepared under ultrahigh vacuum (UHV) conditions, and also facilitates high resolution UPS and XPS measurements [91, 182, 250].

PEN and PFP – like most organic semiconductor molecules[22, 39, 251] – are physisorbed on Au(111) [150, 252], while on Cu(111) PEN exhibits strong chemisorption [200, 227]. Therefore, we chose Au(111) and, for comparison,

Cu(111) as substrates to study the D-A bilayer systems (PFP / PEN and PEN / PFP) and to investigate in particular the impact of the substrate interaction for this D-A pair. Hence, the aim of the present work is to elucidate the coupling strength of this important D-A pair, and the influence of subsequent layers on the adsorption distance of the first layer.

5.2 Adsorption properties of PEN and PFP on Au(111)

We start discussing the electronic and adsorption properties of PEN and PFP on Au(111), as determined by XSW, UPS and XPS techniques. To determine the adsorption distance, the monolayer PEN (PFP) has been prepared on the Au substrate by OMBD process (Section 3.1.2), and the thin film properties were then measured by HR-XPS and XSW techniques. To obtain a well-formed monolayer on the substrate, a low-temperature annealing (desorption) process was carried out with roughly three organic molecular layers (~ 10 Å) on the substrate.

5.2.1 PEN on Au(111)

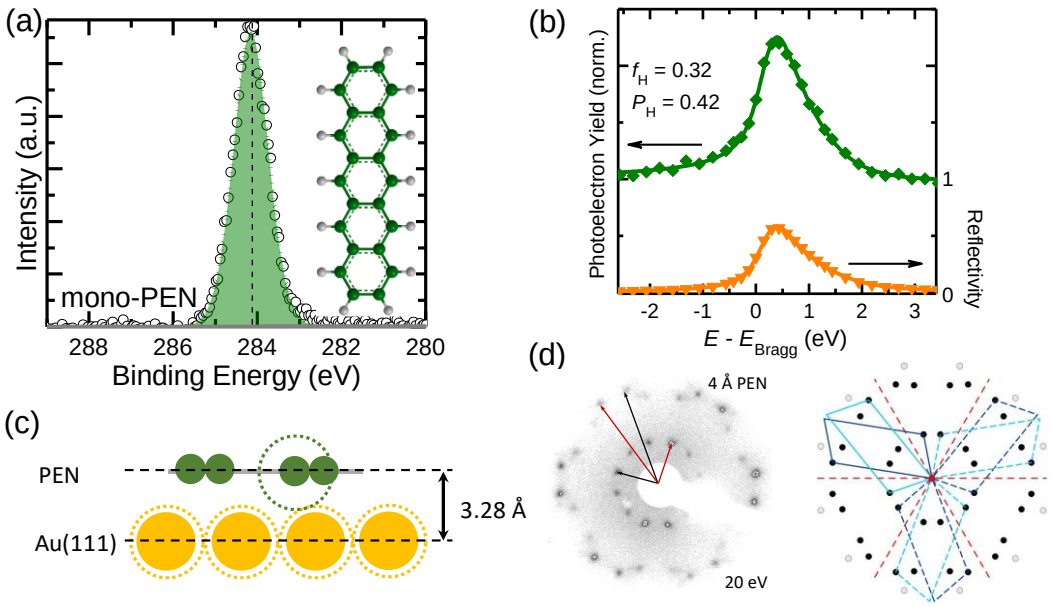

Figure 5.1: (a) HR-XPS spectrum of monolayer PEN on Au(111) with chemical structure inserted. (b) XSW fitting results of PEN monolayer adsorbed on Au(111). (c) Elements with dashed circles are drawn according to their van der Waals radii, and solid balls the covalent radii. The displayed adsorption distance was calculated by taking into account the surface reconstruction observed on the gold surface [217]. (d) Experimental and simulated LEED patterns on monolayer PEN/Au(111).

Pentacene ($C_{22}H_{14}$), as its chemical structure inserted in Fig. 5.1(a), has been studied primarily to compare with the bilayer behavior. According to its chemical structure, the HR-XPS results presented only C 1s signal as shown in Fig. 5.1(a), located at the BE of 284.12 eV and further guide to analyze the XSW data. For the adsorption of PEN on Au(111), plotted in Fig. 5.1(b), the bonding distance (3.28 Å, see Tab. 5.2) is essentially the same as its interplanar spacing [253, 254], which shows the similar adsorption distance as the other physisorption regimes [55, 97, 102, 199]. The adsorption geometry of (sub)monolayer PEN on Au(111) has been sketched in Fig. 5.1(c). Well-defined LEED pattern for monolayer PEN on Au(111) has been measured and analyzed in detail to characterize the in-plane structure, in Fig. 5.1(d). We have found the unit cell of $a = 16.09$ Å, $b = 7.65$ Å and $\gamma = 70.2°$, with the superstructure of $\begin{pmatrix} 6 & -1 \\ -2 & 3 \end{pmatrix}$ the same as previous study [200].

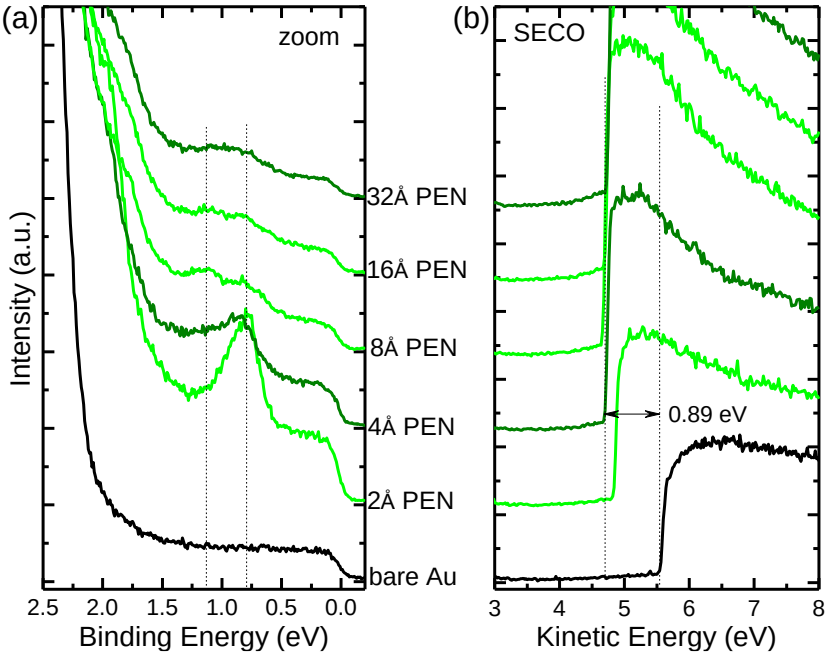

Figure 5.2: (a) Zoom in valence band and (b) SECO spectra of thickness-dependent PEN deposited on Au(111). In the figures, substrate are colored by black, PEN monolayer (4 Å) and multilayer (32 Å) are highlighted by darker green. Dashed vertical lines are used for comparison.

The electronic properties of thickness-dependent PEN on Au(111), moreover, confirm the physisorption, as has been concluded in the previous studies [150, 200]. With initial PEN deposition (2 Å), the appeared peak (centered at the BE of 0.81 eV)

is ascribed as the monolayer HOMO peak of PEN. Further deposition leads to a broadening of this peak, while a second peak (1.12 eV) arises at its left shoulder. Subsequently, the monolayer HOMO peak decreases and the other increases slightly. In Fig. 5.2(b), the SECO spectra have been exhibited. As highlighted by different color, the WF has been shifted by 0.89 eV with monolayer PEN deposited on the substrate, and remains constant with further deposition. The vacuum level shift is mainly attributed to the push-back effect of metal surface electrons spilling out into vacuum [200].

5.2.2 PFP on Au(111)

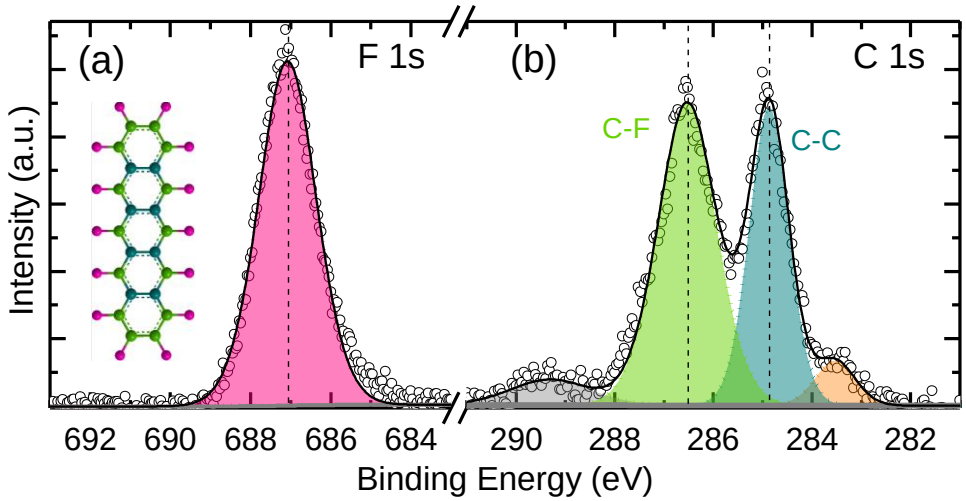

Figure 5.3: HR-XPS spectra of monolayer PFP on Au(111) with chemical structure inserted, F 1s (a) and C 1s (b) core-levels are as displayed.

Perfluoropentacene ($C_{22}F_{14}$), chemical structure inserted in Fig. 5.3(a), has been studied to determine its adsorption properties. As observed by its chemical structure, the HR-XPS results, in Fig. 5.3, are showing the F 1s and C 1s core-level spectra. In Fig 5.3(a), the fluorine atoms in PFP molecules are located at the binding energy of ~686.56 eV. However, the carbon atoms in the molecules, in Fig. 5.3(b), indicate two different species, named C-C (carbon bound to another carbon atom) and C-F (carbon bound to a fluorine atom), at the BE of 284.85 eV and 286.56 eV [227], the same as this molecule on the other coinage metal substrates [202, 255, 256]. The fitting mode of C 1s core-level spectra, then, will be used to adapt on the XSW analysis. The gray peak, at higher binding energy (~ 290 eV), is ascribed as the

shake-up contribution; the golden curved peak, at lower binding energy (~ 283 eV), indicates the C-Au bond as partially C-F bonds are broken [206].

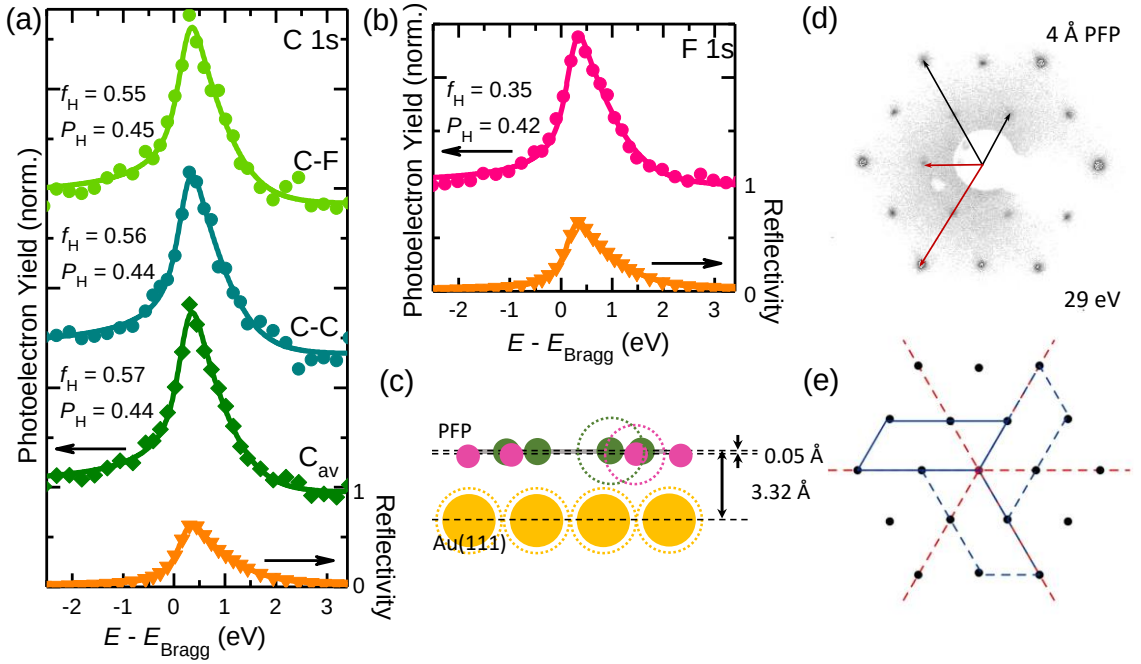

Figure 5.4: XSW fitting results of PFP monolayer adsorbed on Au(111), C 1s (a) and F 1s (b) core-levels. Spectra are taken at Bragg energy of Au(111), $E_{Bragg} = 2634$ eV. The chemical sensitivity of this technique provides information for the different atom species, carbon and fluorine atoms, as well as for the different inequivalent carbon atoms in PFP (named as C-C and C-F, C_{av} the averaged adsorption distance of all carbon atoms in PFP molecules). (c) Sketch of the vertical adsorption geometry of PFP on Au(111), the fluorine atoms show a lower adsorption distance (0.05 Å) than that of carbon. Elements with dashed circles are drawn according to their van der Waals radii, and solid balls the covalent radii. The displayed adsorption distance was calculated by taking into account the surface reconstruction observed on the gold surface [217]. (d) Experimental and (e) simulated LEED patterns on monolayer PFP/Au(111).

As shown in Fig. 5.4(a) and (b), the entire adsorption information of (sub)monolayer PFP on Au(111) is obtained, with fluorine and two carbon species depicted, adapted the fitting mode discussed in Fig, 5.3. Compared to a monolayer PEN on Au(111), PFP maintains a similar adsorption distance as PEN, with its fluorine atoms located at the distance of 3.27 Å ($P_H = 0.42$) and both carbons ($P_H = 0.44$) remain 0.05 Å higher adsorption distance than fluorine. According to the

limitation of the XSW technique, we conclude a flat-lying PFP, see the sketch shown in Fig. 5.4(c), on Au(111) with a typical physisorption regime. In Fig. 5.4(d, e), we have found the unit cell of a = 17.34 Å, b = 8.67 Å and γ = 60°, with the superstructure of $\begin{pmatrix} 6 & 0 \\ 0 & 3 \end{pmatrix}$ the same as previous study [256].

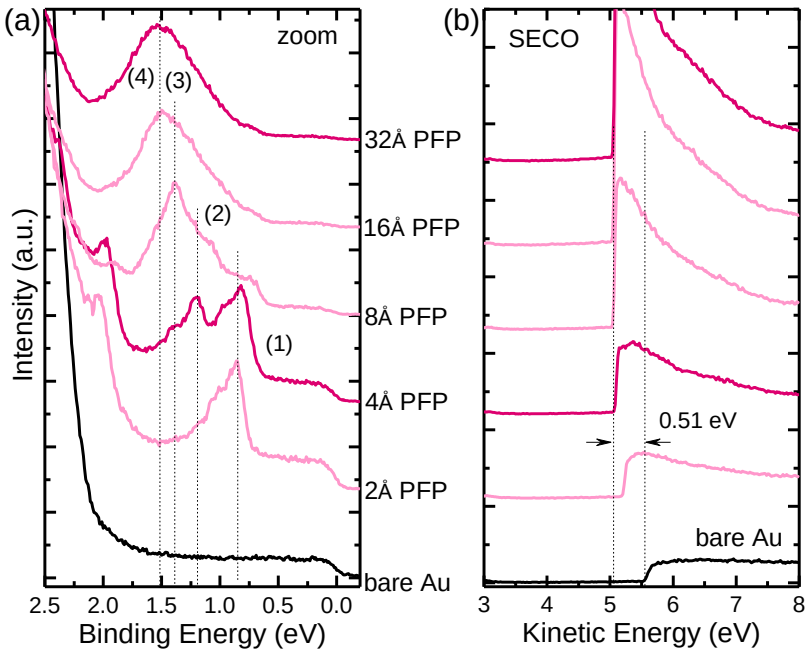

Figure 5.5: (a) Zoom in valence band and (b) SECO spectra of thickness-dependent PFP deposited on Au(111). In the figures, substrate are colored by black, PFP monolayer (4 Å) and multilayer (32 Å) are highlighted by darker red. Evolution of valence band shift and vacuum level shift are highlighted by dashed vertical lines.

The electronic properties of thickness-dependent PFP on Au(111) have been displayed in Fig. 5.5, zoom in valence band (a) and SECO spectra (b). As highlighted by four vertical lines in Fig. 5.5(a), four HOMO peaks are ascribed as four layer contributions [150]. Deposition of PFP on Au(111) has shifted the sample WF from 5.55 eV (bare Au) to 5.07 eV (nominal monolayer thickness 4 Å), that is, 0.48 eV difference, and can be described as the push-back effect, due to the weak interaction between PFP and Au(111) interface [150].

5.3 PEN-PFP bilayers on Au(111)

After discussing the electronic and adsorption properties of PEN and PFP on Au(111), the bilayer formations on Au(111) will be introduced in this section, determined by XSW, UPS and XPS methods. The experimental process remains similar as in Section 5.2, in case to obtain a well-formed monolayer on the substrate, a low-temperature annealing (desorption) process was carried out with roughly three organic molecular layers (~ 10 Å) on the substrate. Consequently, (sub-)monolayer of PFP or PEN molecules have been deposited on the sample, the UPS and XPS measurements are then carried out with thickness-dependent processes.

5.3.1 Adsorption Properties

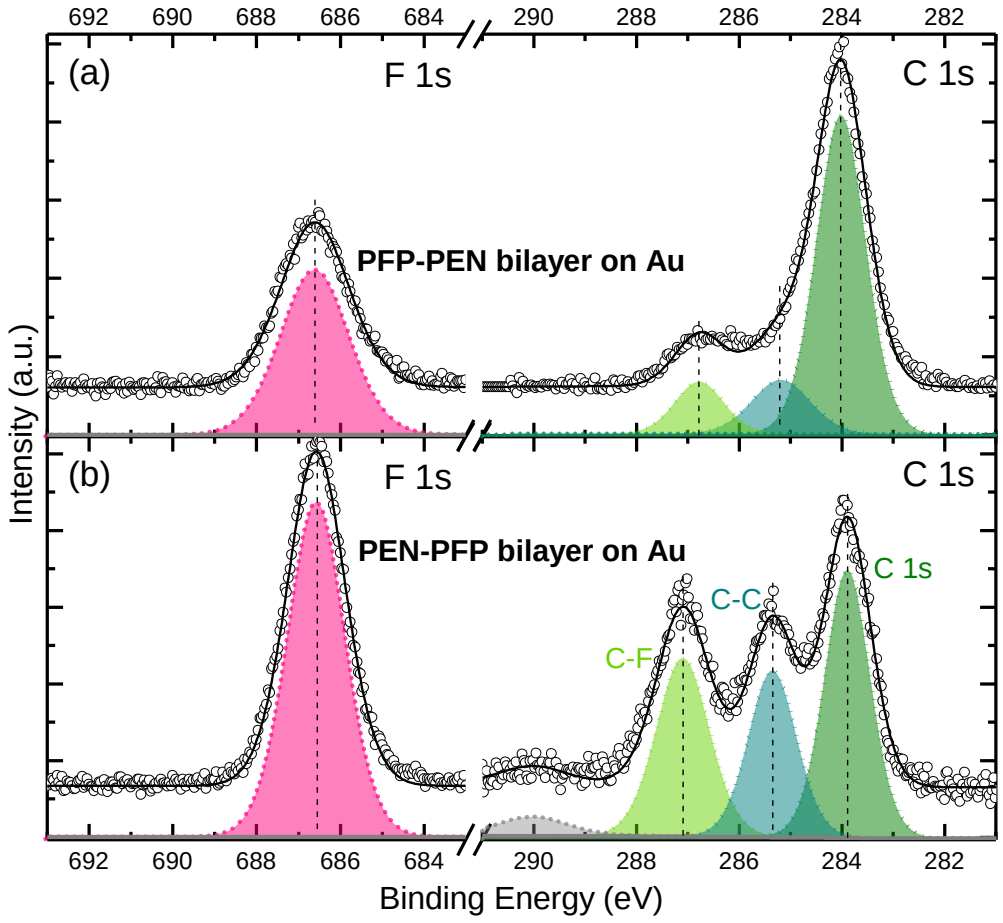

Figure 5.6: HR-XPS spectra of PFP-PEN, PEN-PFP bilayer on Au(111). (a) PFP was deposited on the monolayer PEN on Au(111); (b) PEN was deposited on the monolayer PFP on Au(111). Dashed lines are used for comparison.

To characterize the electronic properties of the two bilayers on the Au substrate, HR-XPS measurements have been carried out to extract the core-level information. As shown in Fig. 5.6, the two growth sequences of the bilayers result in almost identical core-level signals. As expected, in both cases, the top layers show slightly lower intensities as slightly less than a monolayer has been intentionally deposited. Overall we find significant changes in the BE position of the C 1s core-levels in the bilayers with respect to the single-component monolayers. The F 1s signal at a BE of 686.55 eV in Fig. 5.6 originates from the PFP molecules and is at 0.52 eV lower BE than in the PFP monolayer (Fig. 5.3a). When turning to the carbon core-level spectra, three distinct peaks at 284.01 eV, 285.18 eV and 286.88 eV can be identified in Fig. 5.6(a). The prominent peak at the lowest BE, which is associated with PEN molecules in the bilayer, is observed at smaller BE ($\Delta = -0.14$ eV compared to the PEN monolayer on Au(111) in Fig. 5.1a). The two peaks with similar intensities to the left of the PEN signal are attributed to C-C and C-F contributions of PFP molecules in the bilayer. The C-C peak of PFP is shifted to higher BE ($\Delta = +0.31$ eV compared to the PFP monolayer spectrum on Au), i.e. contrary to the PEN carbon signal, as well as the C-F peak of PFP ($\Delta = +0.39$ eV). Importantly, for the PEN on PFP bilayer spectrum shown in Fig. 5.2(b) the three main peaks, which correspond to the same chemical species as just discussed, exhibit the same trend of core-level shifts as the PFP on PEN bilayer: The C signal derived from PEN is located at an even lower BE ($\Delta = -0.26$ eV), while the C-C and C-F signals of PFP shift to higher BE ($\Delta = +0.47$ and $+0.59$ eV). The specific values of these peak positions are summarized in Tab. 5.1.

Table 5.1: Core-level positions of fluorine atoms and inequivalent carbon atoms determined by HR-XPS measurements, mono-PEN, mono-PFP, deposition sequence of PFP/PEN and PEN/PFP bilayers.

/eV	C (PEN)	C-C (PFP)	C-F (PFP)	F (PFP)
mono-PEN	284.15	*	*	*
mono-PFP	*	284.87	286.49	687.07
PFP/PEN	284.01	285.20	286.78	686.59
PEN/PFP	283.87	285.34	287.08	686.55

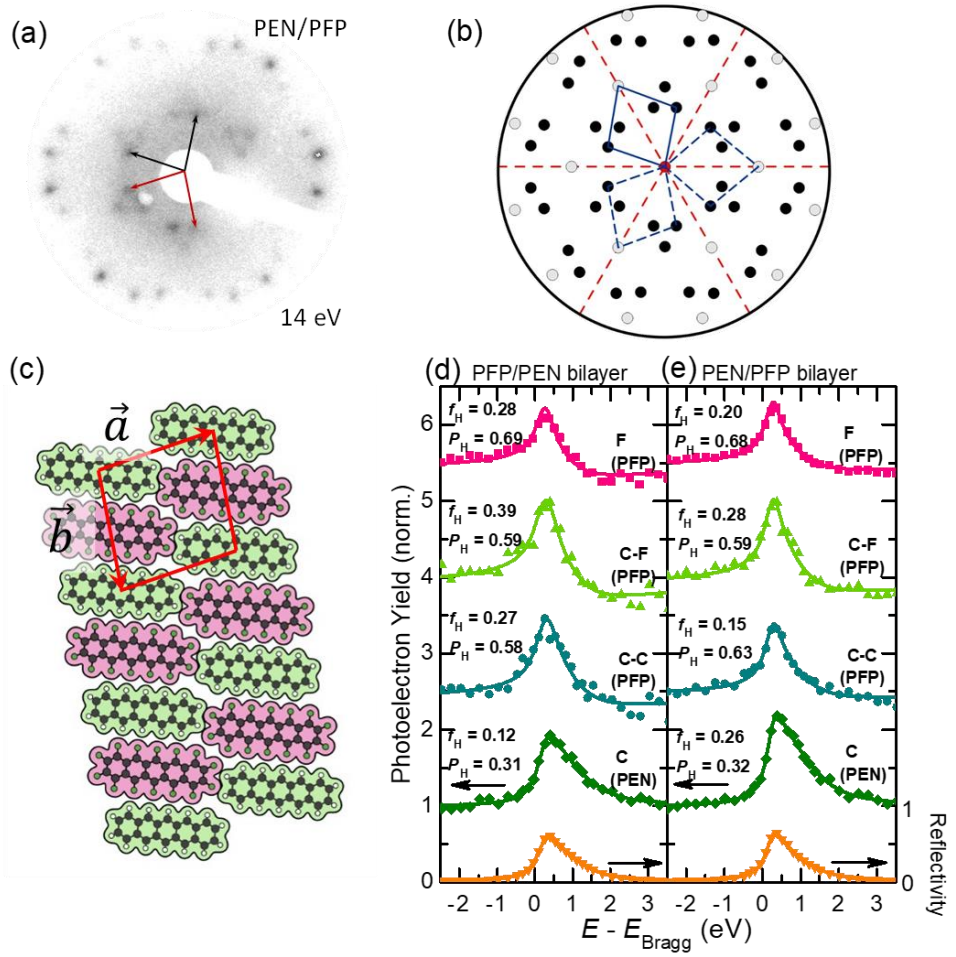

Figure 5.7: (a) LEED pattern of PEN/PFP bilayer on Au(111), (b) simulated LEED pattern, (c) model of a mixed film with the unit cell derived from the simulated LEED pattern. (d) and (e) XSW fitting results of the D-A bilayers adsorbed on the Au(111) substrate. The structural information is contained within the coherent position, P_H, and the coherent fraction, f_H. Spectra are taken around the Bragg energy E_{Bragg} = 2.634 keV of Au(111).

The analysis of the PEN/PFP bilayer LEED pattern is shown in Fig. 5.7(a-c). For the experimental LEED pattern (Fig. 5.7a), a superstructure of $\begin{pmatrix} 6 & -2 \\ -2 & 6 \end{pmatrix}$ has been derived, showing that the corresponding unit cell is significantly larger than that of the monolayer films on Au(111) (Fig. 5.1 and Fig. 5.4) with $a = 15.29$ Å, $b = 15.29$ Å and $\gamma = 81.8°$. In particular, b is increased by a factor of ~ 2 so that a and b are now equal, which allows us to conclude that the unit cell contains two molecules. Since the identical LEED patterns for both stacking sequences have been observed (i.e. PEN/PFP and PFP/PEN) [148], it is likely that these two molecules are a PEN and a

PFP molecule per unit cell. The corresponding molecular superstructure is illustrated in Fig. 5.7(c).

The XSW bilayer data displayed in Fig. 5.7(d) are derived using the HR-XPS fitting model (Fig. 5.6) to extract the photoelectron yield (Y_P). Hence, we are able to provide structural information for each element and chemically inequivalent species of PEN and PFP.

For the two bilayer systems considered, i.e. with the deposition order of PFP on PEN (Fig. 5.7d) and PEN on PFP (Fig. 5.7e), robust coherent positions and fractions could be derived for all carbon species and the fluorine atoms. The fluorine signal, which is necessarily related to the PFP molecules, apparently yields an adsorption distance of PFP 6.23 Å ($P_H = 0.69$) above the Au(111) surface within the PFP-PEN bilayer. Interestingly, the fluorine signal is practically the same for the PEN-PFP bilayer with almost identical P_H and similar f_H values. Further insight into the adsorption behavior can be derived from the carbon species of PEN and PFP: for both bilayers, we find nearly identical coherent positions P_H for C (PEN) with 0.31 vs. 0.32, and likewise for C-C and C-F (PFP) values close to 0.60. Thus, the coherent positions for all species are within the error margin independent of the deposition sequence. Moreover, they are significantly different from the respective values of the monolayer systems (cf. Tab. 5.3). In principle, this could be explained by bilayer formation and with the bonding distance of the molecules in the contact layer (first monolayer) being strongly affected by the adsorption of the second layer. Another scenario, however, is partial molecular exchange in a way that, for both systems, PEN as well as PFP molecules occupy the first and the second layer with similar probability, which means that mixed bilayers are formed, as indicated by LEED analysis. The modulo-n ambiguity of NIXSW complicates an assignment of vertical bonding distances in heterostructures. Nevertheless, for a bilayer with PFP exclusively in the contact layer on Au(111), i.e. without considering a mixed bilayer, the coherent position that was measured would correspond to adsorption distances either in the range of 1.4 Å or 3.7 Å (according to Equ. 3.8), which are both unreasonable values, e.g. too small or too large. For PEN in the contact layer, an average adsorption height of around 3.0 Å would be obtained, which is in the range of reasonable values for COMs on Au(111) [39]. Yet, the adsorption distances of PEN

in both bilayers would be rather low compared to its monolayer value of 3.28 Å on Au(111), considering that for other bilayer systems on Au(111) the second layer does not influence the adsorption distance of the first layer significantly [102]. Therefore, we conclude that the most likely reason for the observed small coherent fractions and unreasonable adsorption heights, compared to the ordering bilayer growth, e.g. F_{16}CuPc/PTCDI bilayer on Au(111) ($f_H \approx 0.5$) [102], is that PEN and PFP occupy both layers of the bilayer systems, because of the strong intermixing.

Comparing the behavior of PFP/PEN bilayers on Au(111) and Cu(111) [257], i.e. nearly unchanged adsorption distance of PEN on Cu versus the strong change induced by PFP on Au, demonstrates their fundamentally different nature. The PFP molecules in the two bilayers exhibit a reversed bending, i.e. on Cu(111) the F atoms are closer to the substrate than the C atoms of PFP, whereas on Au(111) the F atoms are further away. The coherent fractions associated with the PFP/PEN bilayer on Cu, however, are similar to those on Au. Below, the exact adsorption distances are provided in Tab. 5.2, showing that F and C have an adsorption difference of 0.19 Å.

Table 5.2: Coherent fraction (f_H), coherent positions (P_H) and adsorption distance (d_H/Å) of the samples obtained by XSW measurements, monolayer of PEN and PFP on Au(111), bilayer systems of PFP on PEN and PEN on PFP on Au(111), monolayer PEN on Cu(111) and PFP/PEN bilayer on Cu(111), respectively. The XSW results of COMs on Cu(111) are taken from Ref. [257].

		PFP/PEN/Au(111)				PFP/PEN/Cu(111)			
		PEN	PFP	PFP/PEN	PEN/PFP			PEN	PFP/PEN
C (PEN)	f_H	0.32	*	0.12	0.26	C (PEN)	f_H	0.52	0.40
	P_H	0.42	*	0.31	0.32		P_H	0.16	0.13
	d_H	3.28	*	*	*		d_H	2.43	2.35
C-C (PFP)	f_H	*	0.56	0.27	0.15	C (PFP)	f_H	*	0.21
	P_H	*	0.44	0.58	0.63				
	d_H	*	3.33	*	*		P_H	*	0.79
C-F (PFP)	f_H	*	0.55	0.39	0.28				
	P_H	*	0.45	0.59	0.59		d_H	*	5.73
	d_H	*	3.33	*	*				
F 1s	f_H	*	0.55	0.28	0.20	F 1s	f_H	*	0.20
	P_H	*	0.45	0.69	0.68		P_H	*	0.69
	d_H	*	3.33	*	*		d_H	*	5.54

5.3.2 Thickness-dependent Photoelectron properties

Valence band spectra measured by UPS for different PEN+PFP heterostructures and thicknesses are shown in Fig. 5.8. Here, the labels only refer to the deposition order and not to the real situation on the surface. For a PEN monolayer (4 Å) on the Au(111) substrate (green curve), the peak centered at a BE of 0.79 eV (feature 2) can be identified as the monolayer HOMO peak of PEN. Upon deposition of PFP on top of the PEN monolayer, the intensity of this peak is decreasing and a new peak (feature 3) appears, which is located at a similar BE as the HOMO-level of PFP in multilayer on Au(111) [150]. A careful look at the valence band spectra reveals that the broad peak at ~0.7 eV BE observed for 2 Å PFP on mono-PEN/Au is shaped by two contributions: feature 2 is considered as weakened monolayer HOMO peak of PEN, whereas feature 1 arises at a lower BE (peak onset at 0.49 eV). Because the observed shift of feature 1 relative to the PEN-HOMO is similar to that of the PEN C 1s core-level (Fig. 5.6), we believe that this peak is derived from PEN molecules in the mixed bilayer. With more PFP deposition, the HOMO peak of PEN gradually disappears. However, for the PEN/PFP bilayer (top four curves), i.e. with a PFP monolayer (4 Å) on Au(111) (red curve), a HOMO peak (feature 4) stemming from mono-PFP is observed. It has been shown that monolayers of PEN and PFP on Au have similar HOMO positions at 0.78 eV BE vs 0.90 eV BE [150, 200], which agrees with our measurements of 0.79 eV for PEN (feature 2) and 0.85 eV for PFP (feature 4). Obviously, upon the initial PEN deposition (1 Å), this peak disappears and new HOMO peaks (feature 1 and 5) emerge, which are identified as PEN signals. The HOMO peak corresponding to feature 1 is the same as the PFP-PEN bilayer. For 2 Å PEN deposition, new bilayer peaks arise (feature 4) and the spectrum shows the same features as the 2 Å PFP / PEN system. In agreement with the XSW analysis of the bilayers, we conclude that with PEN deposited on mono-PFP / Au(111), PEN molecules have partially moved into the first layer on Au(111). The surprisingly weak HOMO peak (feature 1), again, is considered as the peak derived from the PEN/PFP mixture. Overall, the UPS data represent a superposition of the HOMO signals of PEN and PFP molecules as well as the mixed bilayer, similar to the observations on HOPG substrates [28]. For specific HOMO and work function (WF) values of each thickness, we refer to Tab. 5.3.

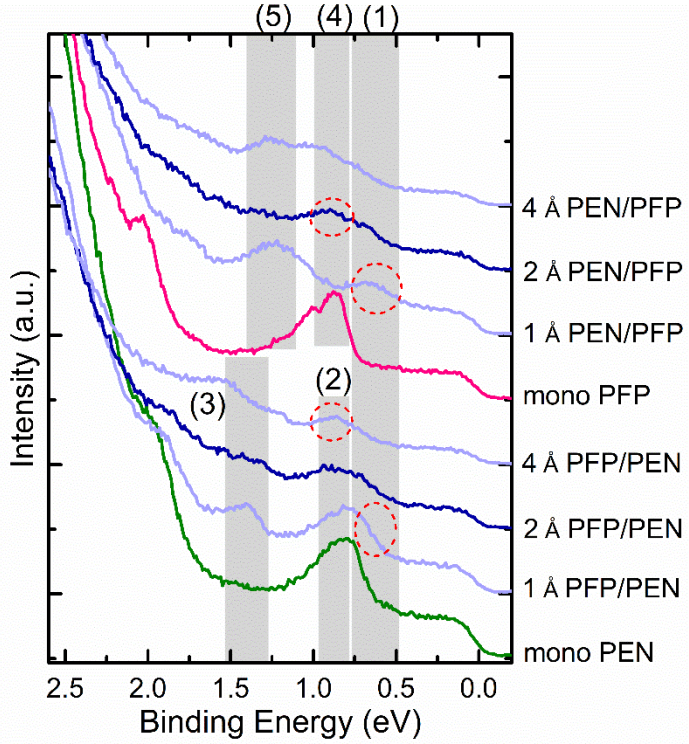

Figure 5.8: UP spectra for stepwise deposited COMs on Au(111). Green curve is the PEN monolayer, red curve the PFP monolayer, blue the mixture and the darker blue the bilayers.

Table 5.3: Summary of work function (WF) and valence band (VB, taken from HOMO onset) binding energies extracted from UPS measurements.

/ eV		**bare Au**	*	**2 Å**	**4 Å**	**8 Å**	**16 Å**	**32 Å**
PEN	VB	*	*	0.57	0.59	0.48	0.49	0.52
	WF	5.56	*	4.84	4.70	4.67	4.68	4.72
PFP	VB	*	*	0.74	0.66	0.60	0.68	0.78
	WF	5.55	*	5.20	5.07	5.04	5.03	5.04
		bare Au	**adlayer**	**1 Å**	**2 Å**	**4 Å**	**8 Å**	**32 Å**
PFP-PEN	VB	*	0.53	0.56	0.49	0.56	0.53	0.55
	WF	5.55	4.80	4.52	4.75	4.78	4.80	4.83
PEN-PFP	VB	*	0.72	0.44	0.49	0.55	0.54	0.45
	WF	5.54	5.24	4.94	4.81	4.77	4.77	4.77

5.4 Discussion

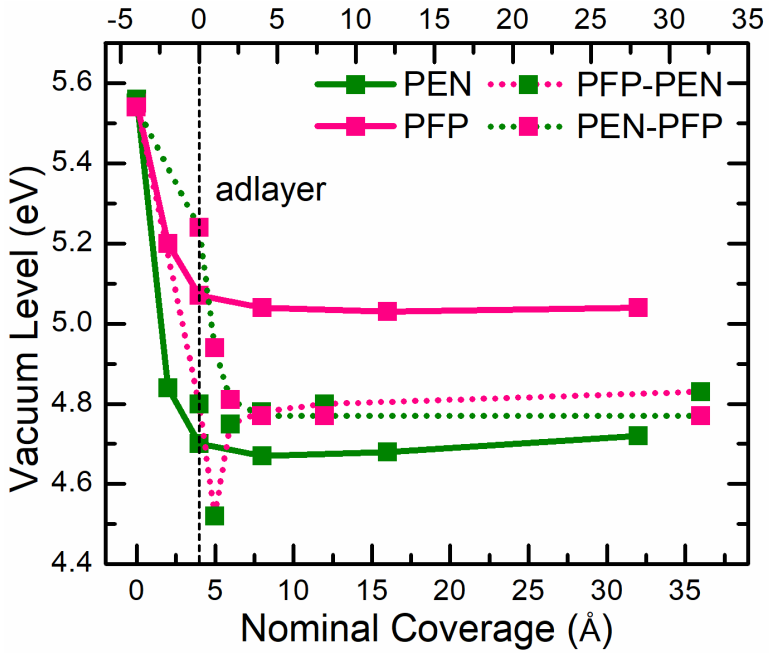

Figure 5.9: Coverage-dependent evolution of the vacuum level with respect to the corresponding Fermi level for the investigated bilayer on Au(111), as well as the coverage-dependent pure films. The vertical line shows the adlayer information, while monolayer PEN in PFP-PEN bilayer and monolayer PFP in PEN-PFP bilayer.

The vacuum level (VL) position with increasing film coverage (Fig. 5.9) provides further insight into the interfacial interaction strength at the PEN-PFP mixture interface and the morphology of the thin films. As shown in Fig. 5.9, the PEN and PFP pure films grown on Au(111) are essentially the same as the previous studies [150, 200], the VL shift generated with more than 4 Å deposition is ascribed as the push-back effect. The total VL shifts in the two molecules are 0.84 eV and 0.51 eV, respectively. In the mixture systems (dashed curves), with the adlayer (PEN or PFP monolayer) deposited on the substrate, the VLs are shifted as in the pure films. However, further deposition of the second molecules triggers the VL shifts to the similar values in the figure, which further demonstrates the same behavior of the two bilayers upon deposition sequential, likely the 1:1 mixture.

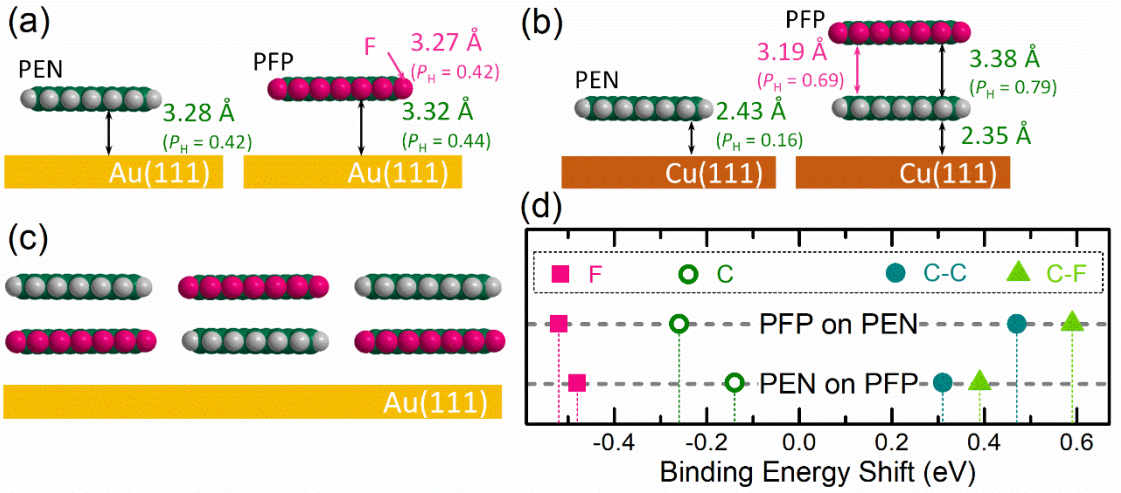

Figure 5.10: Molecular growth model of (a) PEN and PFP monolayers on Au(111), (b) PEN monolayer and PFP/PEN bilayer on Cu(111). This sketch is re-drawn with permission from Ref. [257]. The adsorption distances derived from XSW measurements are included. Pink value belongs to the fluorine atoms and green the carbon atoms. (c) The bilayer mixture on Au(111), (d) core-level shifts of PEN (hollow circles) and PFP (solid spots) in the bilayer mixtures on Au(111), with respect to the monolayer BE for the PEN and PFP molecules. All the core-level shifts determined by HR-XPS were measured at DLS, while the HOMO shifts were determined by UPS at Soochow University.

The results of the present work are schematically summarized in Fig. 5.10, i.e. the monolayer adsorption geometry with the element-specific adsorption distances of both molecules, a possible arrangement of PEN and PFP molecules in the mixed bilayer phase, and the observed core-level shifts in the mixtures. As discussed above, the monolayers of PEN and PFP on Au(111) are structurally well defined (see Fig. 5.10a) with typical physisorption distances of 3.28 Å for PEN and 3.32 Å for PFP as determined by the XSW measurements. Due to the strong chemisorption of PEN on Cu(111), sequential bilayer growth of PFP and PEN is facilitated on this substrate. The PFP-PEN distance of 3.38 Å on Cu(111), however, is typical for COMs interacting mostly via van-der-Waals forces. In contrast, PEN-PFP bilayers grown on Au(111) form a mixed phase (Fig. 5.10c). The C 1s core-level peaks of PEN (open symbols) shift to lower BE (−0.14 eV and −0.26 eV), while the two carbon species of PFP (solid symbols) shift to higher BE (approx. +0.5 eV). Notably, in both systems the F 1s signals, i.e. those corresponding to the strongly electro-negative species, shift by the same amount towards lower BE (approx. −0.5 eV).

As discussed above, both PEN-PFP bilayer systems on Au(111) feature a 1:1-mixed phase, i.e. similar to PEN:PFP blends in thicker films studied by optical or X-ray diffraction methods [12, 193, 258]. We believe that the opposite electrostatic quadrupole moments of PEN and PFP [11, 259, 260] promote the reordering on Au(111) – quite similar to what was recently reported for PEN:PFP heterostructures on the weakly interacting HOPG substrate with a valence band structure resembling the one shown in Fig. 5.8 for Au(111) [28]. Hence, considering the different behavior of the molecular bilayer system on different substrates we conclude that the mixed phase can form due to weaker molecule-substrate interactions as, for example, on Au(111). In contrast, for PEN and PFP bilayers grown on Cu(111) the strong molecule-substrate interaction suppresses the mixture formation and yields a stacked structure on the surface. The strong coupling of a PEN monolayer with Cu(111) hinders molecular exchange and a well-defined heterointerface is formed upon deposition of PFP.

5.5 Conclusion

In summary, we have studied the morphology of a typical conjugated D-A pair in bilayers and the electronic properties on Au(111) and Cu(111) using XSW, XPS and UPS. The data consistently show mixture formation within the PEN:PFP bilayers on Au(111), as it is hypothesized in view of the LEED and XSW results of the two bilayer systems. The arrangement and order in organic heterostructures affects the performance of (opto)electronic devices and, in general, the formation of mixed phases reduces device efficiency. Predicting the order in organic heterostructure is, thus, essential for rational device design. Our work shows that the intermixing tendency of PEN and PFP is quite strong and a chemisorbed first layer can be used to suppress this.

6. ORGANIC-ORGANIC INTERFACES: TIOPC-TRILAYERS

Titanyl-phthalocyanine (TiOPc, Fig. 6.1) molecules grown on Ag(111), which form an up-down bilayer with **0** net dipole [82, 261, 262], provide a nearly ideal organic and weakly-interacting contact layer for a precise study of the structural properties, interlayer spacing and possible intramolecular distortions, of such an organic-organic (O-O) interface without the substrate influence. By applying UPS and XPS, we have studied the valence state and core-level information of molecular thin films deposited onto a stable and ordered organic dipole layer, whereas the third molecular layer (F_{16}CuPc/P4O) has non-interaction with the substrate and presents the multilayer behaviour on the surface.

6.1 Introduction

Since the organic-organic (O-O) interface is the least understood in complex device architectures, thus it is the one that holds most potential for further efficiency improvements [225, 263, 264]. In this context, molecular heterostructures have attracted significant attention because of their functional properties [24, 31, 265, 266], especially for opto-electronic devices. While monolayer systems of conjugated organic molecules (COMs) on metals have been studied in much detail over the last decade [30, 39, 84, 118], as well as molecular bilayer heterostructures [26, 27, 102, 244], more complex architectures of these materials on surfaces are still mostly unexplored. Importantly, such heteromolecular structure contains few layers are the most basic realisation of an O-O interface, whose functional properties are essential for thicker films and device-like scenarios. Moreover, these systems allow to tune the energy barriers [31, 191] and/or influence the growth mode of subsequently deposited layers [60, 267], both aspects being crucial for an improved charge transport across the different interfaces.

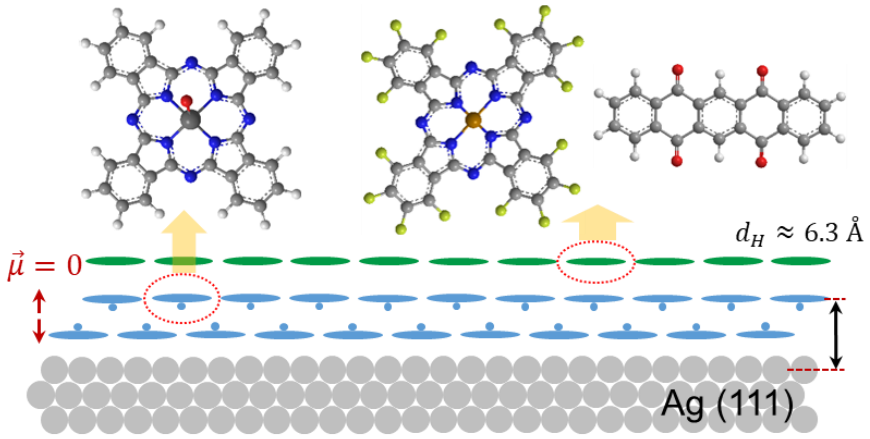

Figure 6.1: Schematics of the systems to have been studied. The bilayer of TiOPc (bi-TiOPc) on Ag(111) is stable and well ordered, which renders a suitable soft contact to study the trilayer systems with the target molecules, as shown F_{16}CuPc and P4O.

In this chapter, we have focused on the investigation of two trilayer systems on Ag(111), and pre-studied the thickness-dependent characteristics of TiOPc and F_{16}CuPc deposited on the same substrate. As demonstrated in Ref. [82, 261, 268], the strong interaction between the intrinsic dipoles of TiOPc induces an up-down (Fig. 6.1) layer-by-layer growth with remarkable order and thereby provides a stable, weakly interacting contact layer. To achieve this purpose, we employ UPS and XPS measurements on TiOPc-derived trilayers, as this molecule shows strong dipole-dipole interaction between the first and the second layer. Therefore, the dipole bilayer can prevent undesired molecular exchange and/or diffusion, becomes evident by different desorption temperatures and provides a practical method to prepare homogeneous and well-ordered bilayers by desorption. Indeed, LEED measurements show that the diffraction pattern changes upon formation of a closed second layer, which is used as a fingerprint for bilayer formation. Also, XSW measurements and DFT calculation have shown that the bilayer thickness is ~6.3 Å [82], which can be used as a reference for the subsequent deposition of a third layer. Exploiting the remarkable order shown by the TiOPc bilayer, we have deposited two different organic molecules, namely copper-hexadecafluorophthalocyanine (F_{16}CuPc) and 5,7,12,14-pentacenetetrone (P4O) (Fig. 6.1), which enables a comparison of their effect on the interface properties.

6.2 Electronic Properties: TiOPc and F_{16}CuPc on Ag(111)

The electronic properties of TiOPc and F_{16}CuPc pure films on Ag(111) determined by UPS and XPS have been investigated, as supported by LEED technique. Moreover, these results also provide reference parameters for the further characterization of trilayer systems.

6.2.1 Photoelectron Properties of TiOPc / Ag(111)

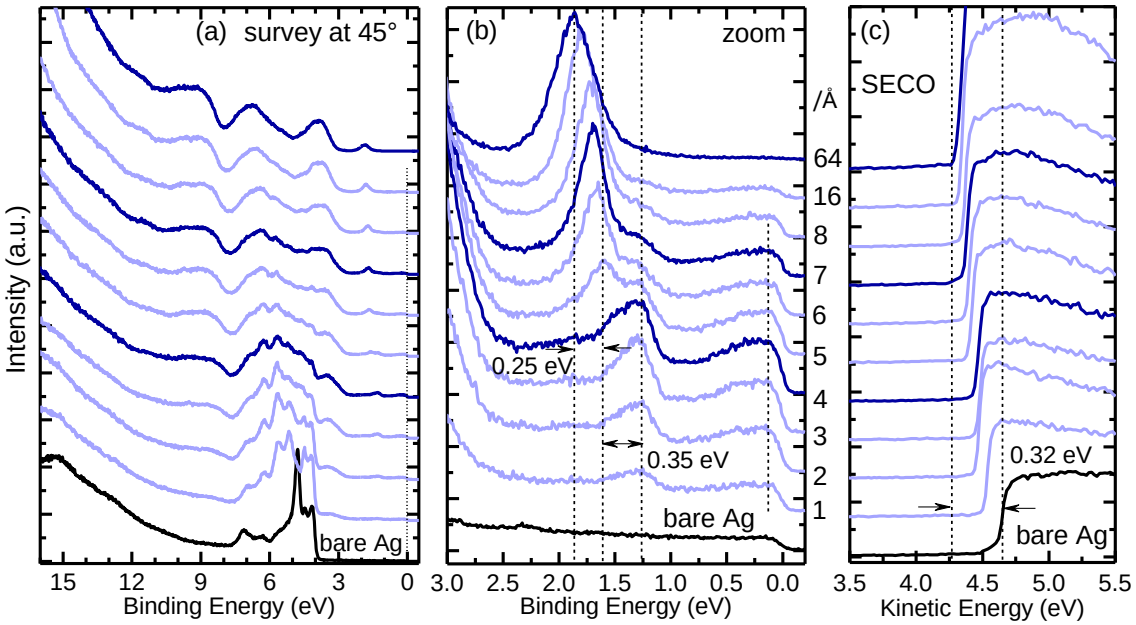

Figure 6.2: Coverage-dependent full valence band (a), zoom in valence band (b) and SECO (c) spectra of TiOPc deposited on Ag(111), valence band spectra are measured at 45°. In the figures, substrate are colored by black, monolayer (4 Å), bilayer (7 Å) and multilayer (64 Å) are highlighted by darker blue.

UPS measurements have been carried out to investigate valence band properties of TiOPc deposited on Ag(111), shown in Fig. 6.2. The overall valence band information, measured at the emission angle of 45°, are displayed in Fig. 6.2(a). With TiOPc deposition, silver d-band signals are gradually vanished, meanwhile organic characteristic peaks arise. Zoom in valence band spectra exhibit precise information of the HOMO satellites. As shown in Fig. 6.2(b), with TiOPc deposition, its HOMO peak continuously emerges, with peak center located at the BE of 1.27 eV. This peak reaches the maximum intensity with the nominal thickness of 4 Å (1ML), which indicates the contribution derived from the first monolayer, as well as other

π-conjugated molecules [150, 199, 200]. With additional TiOPc deposited, this HOMO peak decreases while the second HOMO peak arises at the BE of 1.62 eV, attributed to the second layer. Upon the thickness of 7 Å, the HOMO peak is shifted to the higher binding energy by 0.25 eV up to 64 Å due to the push-back effect [269]. Notably, a peak near Fermi edge (0.14 eV), known as the former LUMO (F-LUMO), becomes partially filled by charge transfer (CT) from the substrate [82, 100]. In the SECO spectra (Fig. 6.2c), the work function has been shifted by 0.32 eV through the full range of thickness evolution. It stays constant when the thickness comes to 7 Å. The continuous shifting of vacuum level after a monolayer (4 Å) deposition is in line with the dipole bilayer geometry, a diverse packing mode with the oxygen atoms up and down [81, 268], which is the same as other phthalocyanine molecules [262, 270]. With initial deposition (less than 4 Å), the vacuum level shift can be described as a combination of push-back effect [226, 271] and CT on the surface, together with the induced molecular dipole moment [82, 220, 261].

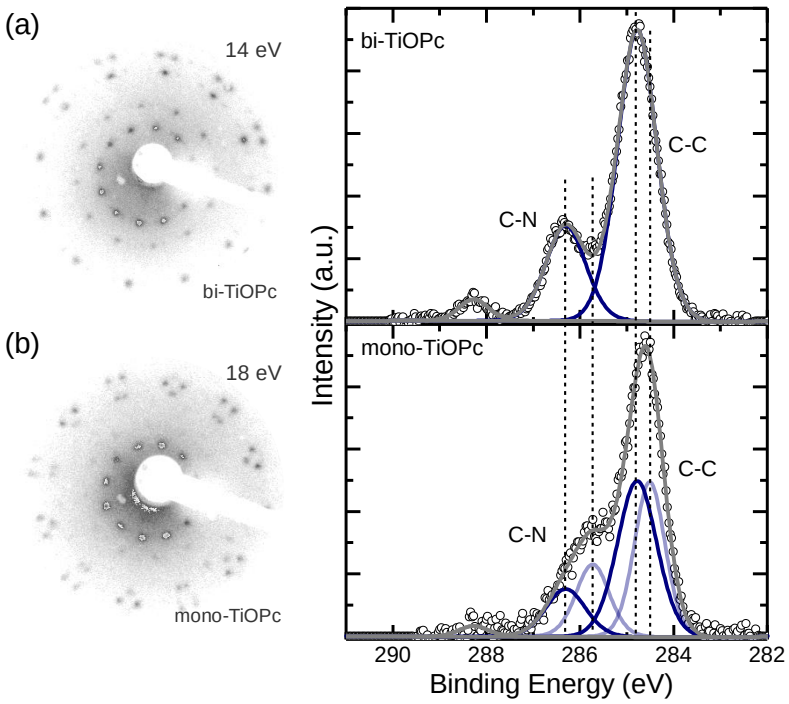

Figure 6.3: Comparison of (a) mono- and (b) bi- layer TiOPc on Ag(111), both LEED patterns and C 1s core levels are displayed. The lighter curves in C 1s spectra show monolayer contributions and the darker curves show multilayer (in this case second layer) contributions.

After discussed the valence band properties of TiOPc on Ag(111), the core-level and planar structures of monolayer and bilayer are shown in Fig. 6.3. When looking at LEED patterns, it is clear that different diffraction patterns are observed, which gives us the indication to figure out mono- and bi- layer films on Ag(111), as reported by Ref. [81, 272]. From the XPS results, the chemisorption of this molecule can be proved: in the bilayer curve (Fig. 6.3a), two contributions from two carbon species are depicted, carbon bound to another carbon atom (C-C) and carbon bound to a nitrogen atom (C-N), which are located at the BE of 284.78 eV and 286.31 eV, respectively. Additionally, a small contribution at the BE of 288.27 eV denotes to a shake-up peak (Section 3.2.2). In Fig. 6.3(b), the C 1s core-level spectrum of monolayer TiOPc on Ag(111) represents complicated results, while chemisorbed molecules in contact with substrate can be distinguished (light blue curves, at BE of 284.78 eV and 286.31 eV) due to the screening effect [22]. The light blue curves belong to the monolayer contribution, and the dark blue the multilayer contribution. To compare with the bilayer TiOPc spectrum, the fitting results of C-C (284.88 eV) and C-N (286.45 eV) peaks in the multilayer spectra, Fig. 6.4, remain identical, as same as other chemisorption molecules on Ag [199, 273].

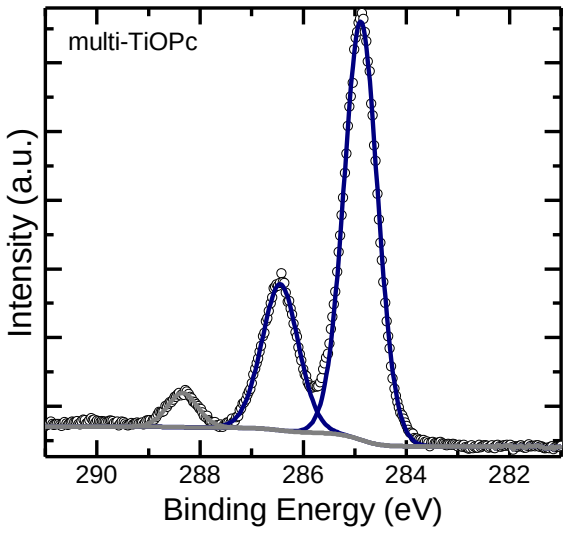

Figure 6.4: XPS of C 1s core level of multilayer (nominal thickness 64 Å) TiOPc deposited on Ag(111).

The real-time XPS data are recorded to confirm the desorption temperature of TiOPc molecules. We have prepared a sample with roughly 4ML (nominal thickness 16 Å) TiOPc on Ag(111), then heated up the sample and carried out XPS measurements simultaneously (Fig. 6.5). According to our results, the multilayer

desorbed at 360 K and the second layer desorbed at 510 K, a temperature gap of 150 K is observed to get bilayer (2ML) thickness. Compared to other desorption processes [79, 245], it indicates that the first two monolayers form a dipole bilayer with each other, since the strong interaction bilayer requires higher temperature to break the coupling strength. The recorded temperature points are then used to prepare the bi-TiOPc template samples.

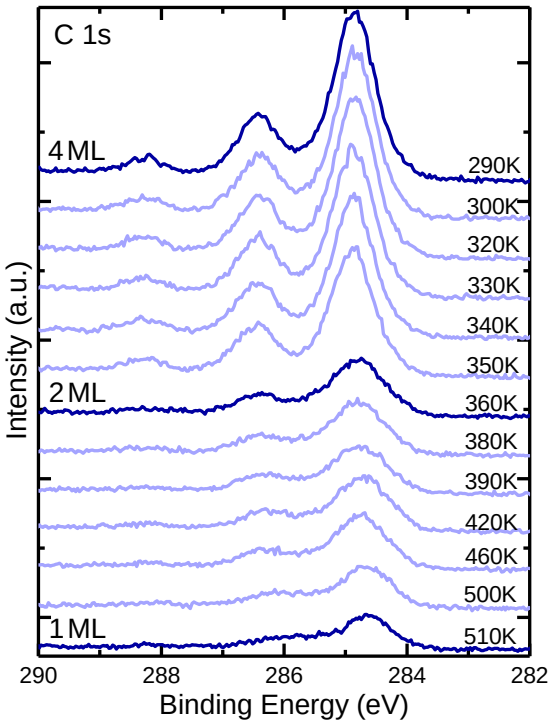

Figure 6.5: Real-time XPS of the C 1s core-level signal during the desorption of TiOPc multilayer. The initial nominal coverage is 16 Å (4ML, four monolayers).

6.2.2 Photoelectron Properties of F_{16}CuPc / Ag(111)

The coverage resolution of F_{16}CuPc / Ag(111) has been performed, shown in Fig. 6.6. In Fig. 6.6(a), the same as TiOPc growth behaviour, the silver features slightly vanished with F_{16}CuPc deposition. Particularly, a peak around the binding energy between 9 eV and 11 eV is ascribed to the fluorination features [150], as being discussed in the UPS technique section, which is in analogy with perfluorinated copper-phthalocyanine molecules [102].

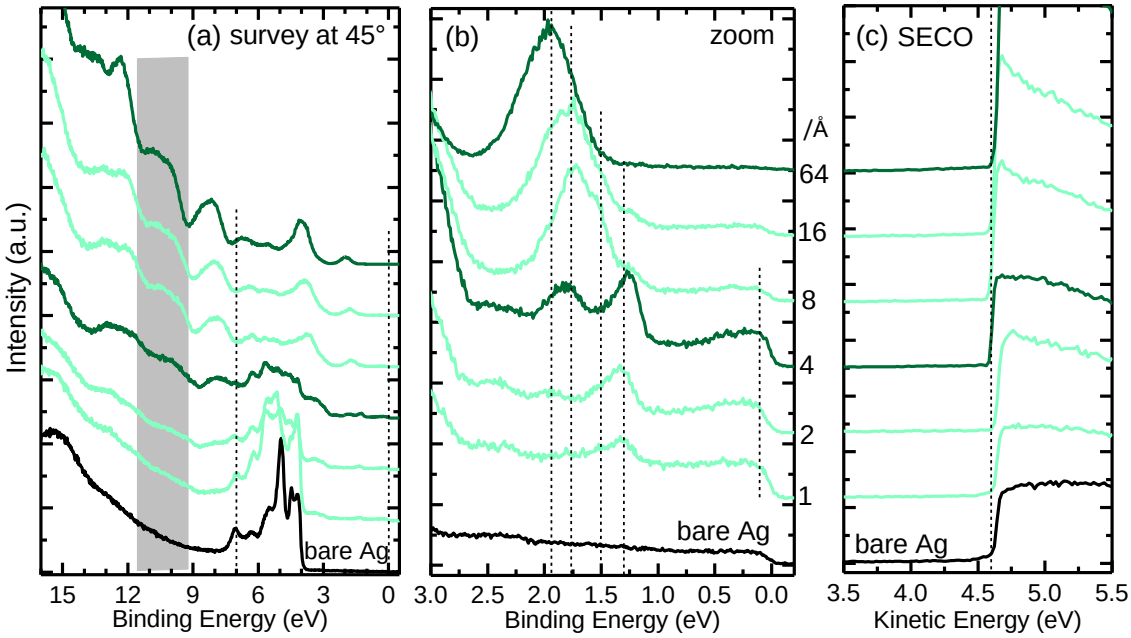

Figure 6.6: Coverage-dependent full valence band (a), zoom in valence band (b) and SECO (c) spectra of $F_{16}CuPc$ deposited on Ag(111), valence band spectra are measured at 45°. In the figures, substrate are colored by black, monolayer (4 Å) and multilayer (64 Å) are highlighted by darker green.

In Fig. 6.6(b), with initial deposition of $F_{16}CuPc$, its HOMO peak already appears located at the binding energy of 1.30 eV (Tab. 6.3 the onset BE position). By comparison, a small peak near Fermi edge (0.11 eV) arises which is assigned to the F-LUMO peak, same as TiOPc on Ag(111) (Fig. 6.2), representing charge transfer between $F_{16}CuPc$ and Ag surface [186]. With more $F_{16}CuPc$ deposition, the intensity of HOMO peak increases, as well as the F-LUMO. Up to monolayer thickness (4 Å), the HOMO peak holds the strongest intensity, indicating the monolayer HOMO contribution. Moreover, the F-LUMO exaggerates to the highest intensity with this thickness, and submerges with further deposition. With the thickness of 8 Å $F_{16}CuPc$ on Ag(111), the HOMO peak located at 1.30 eV decreases and its neighboring HOMO peak (1.77 eV) increases, leading to the second layer contribution of the HOMO orbital. Up to the final thickness (64 Å), there is only one broad peak at the binding energy of 1.94 eV. The valence band spectra indicate a chemisorption behavior of $F_{16}CuPc$ on Ag(111). Therefore, the non-shifting vacuum level, Fig. 6.6(c), would be due to the mixed contribution of charge transfer and push-back effect [198].

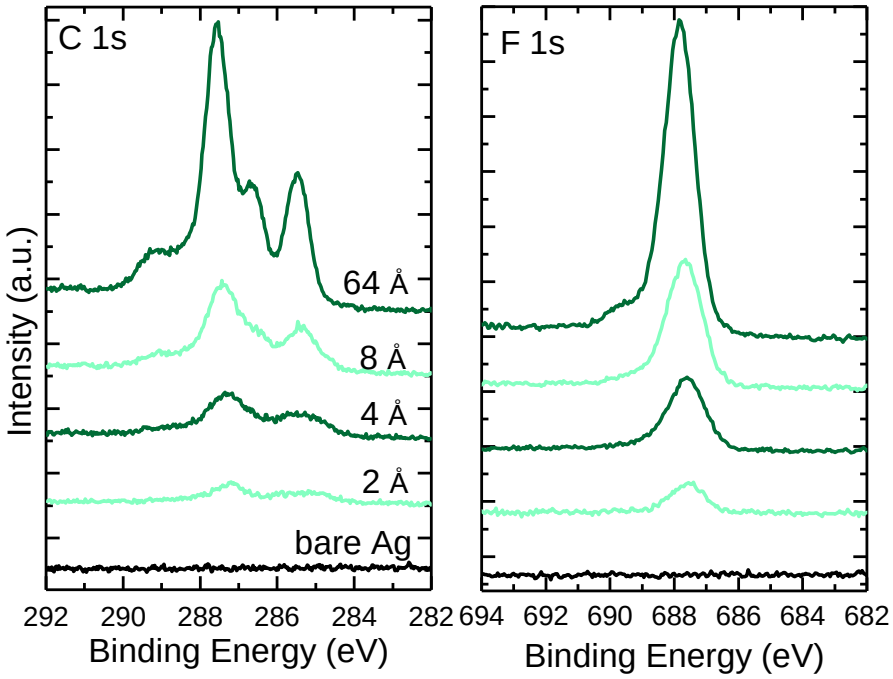

Figure 6.7: Thickness dependent XPS core-level spectra of C 1s (a) and F 1s (b). The $F_{16}CuPc$ monolayer (4 Å) and multilayer (48 Å) are highlighted by dark green and bare substrate the black curve.

The thickness dependent core-level spectra measured by XPS are depicted in Fig. 6.7. In both figures, the core-level spectra recorded with the bare Ag(111) (black curves) are, as no molecules adsorb on the surface, near horizontal. With deposition of the $F_{16}CuPc$ molecules, its carbon and fluorine signals gradually appear, the spectra also confirm the existence of $F_{16}CuPc$ adsorbed on Ag(111). In the C 1s core-level spectra (Fig. 6.7a), the intensity arises with further deposition, meanwhile, different carbon species are obtained due to a complex spectrum in the final thickness. The coverages of nominal thickness 4 Å (mono-), 8 Å (bi-) and 48 Å (multi-) $F_{16}CuPc$ on Ag(111) are further analysed by CasaXPS [162] to classify different carbon contributions (Fig. 6.8). In Fig. 6.7(b), only a main peak is observed in F 1s spectra, as there is one species of fluorine in this molecule, and the intensity increases with further deposition.

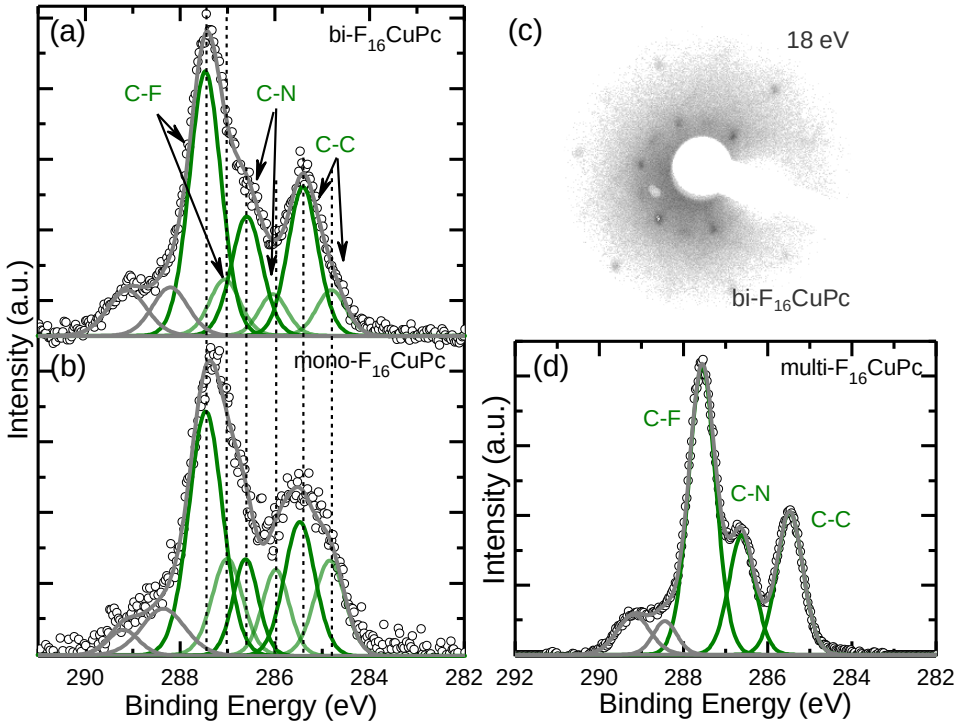

Figure 6.8: Comparison of (a) mono- (b) bi- and (d) multi- layer F_{16}CuPc on Ag(111), (c) LEED pattern of bi-F_{16}CuPc measured at the beam energy of 18 eV is displayed. The lighter curves in C 1s spectra show monolayer contributions and the darker curves show multilayer (in this case second layer) contributions.

In Fig. 6.8, the C 1s core-level (a, b, d) spectra and a LEED pattern (c) are displayed. In the LEED pattern, with the periodic diffracted spots been seen, it reveals an ordered intermolecular structure form by F_{16}CuPc on Ag(111). Moreover, STM study carried out of F_{16}CuPc on Ag(111) [73, 211, 274] indicates a well-ordered monolayer structure of this sample, in agreement with the structural LEED pattern. For the XPS spectra, as both mono- and bi-layer thicknesses are more complicated than that of F_{16}CuPc on Au(111) [102], the multilayer spectrum has been fitted as the reference. In Fig. 6.8(d), three distinctive peaks occupying most of the spectrum area are attributed to C-C, C-N and C-F contributions, located at the binding energy of 285.48 eV, 286.62 eV and 287.56 eV, respectively. The two small peaks at higher binding energy are the shake-up contributions. As of a multilayer coverage, the fitting results indicate mainly multilayer contribution, thus we apply the fitting results on the monolayer (Fig. 6.8a) and bilayer (Fig. 6.8b) spectra. From the figure, except the shake-up domains at higher binding energies, the rest area is fitted into six peak: three the monolayer peaks (lighter green) and other three the multilayer

peaks (darker green), which fit well in both spectra. Therefore, the three peaks located at the binding energy of 284.84 eV (C-C), 285.98 (C-N) and 287.00 eV (C-F) are ascribed as the monolayer contribution, in analogy to the chemisorption behavior [166, 205, 216].

6.3 Trilayer Properties: F_{16}CuPc and P4O monolayers on bi-TiOPc

Having characterized the core-level information and valence band properties of TiOPc and F_{16}CuPc on Ag(111), details of P4O on Ag(111) the readers are referred to Ref. [26, 97], we now start to discuss the trilayer structures. To obtain the well-formed dipole TiOPc bilayer structures, roughly 20 Å TiOPc was vacuum-sublimed onto silver substrate and the sample was heated up to 360 K to desorb extra layer. Subsequently, F_{16}CuPc and P4O were deposited on the bi-TiOPc film.

6.3.1 Photoelectron Properties of F_{16}CuPc / bi-TiOPc / Ag(111)

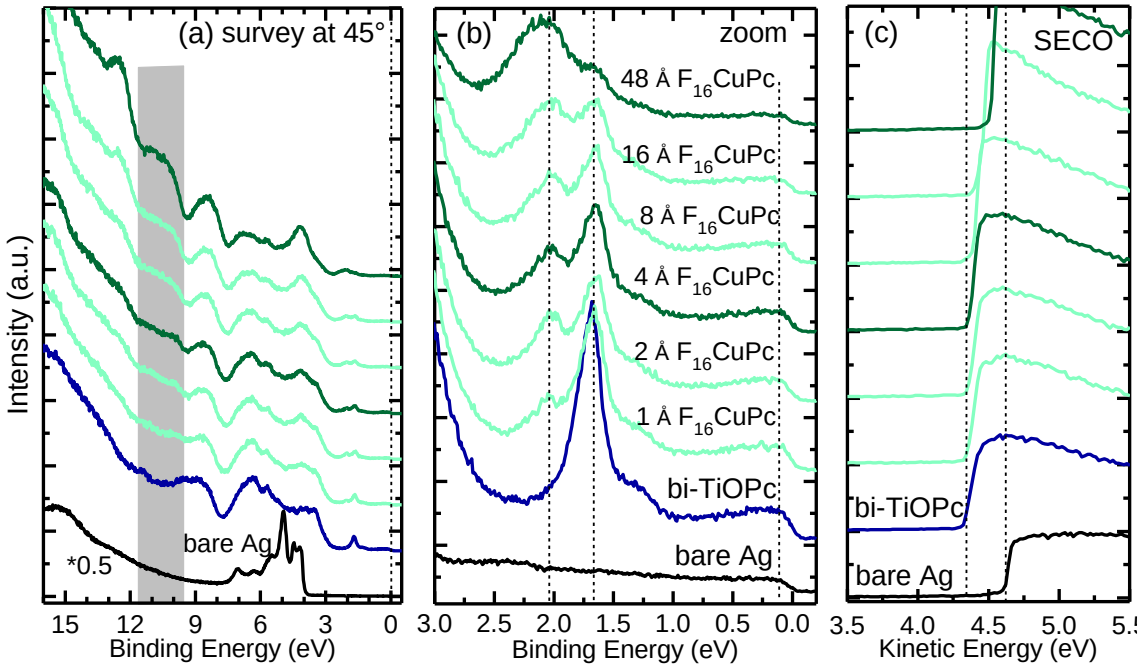

Figure 6.9: Coverage-dependent full valence band (a) and zoom in valence band (b) and SECO (c) spectra of F_{16}CuPc on bi-TiOPc / on Ag(111), valence band spectra are measured at 45°. In the figures, substrate are colored by black, bi-TiOPc the blue curve, F_{16}CuPc monolayer (4 Å) and multilayer (64 Å) are highlighted by darker green.

In Fig. 6.9(a), the UPS full scans recorded at 45° are as shown. The substrate features decrease in intensity with the increasing coverage of organic molecules, leaving only the molecular features in the spectra. It can be extracted, therefore, that the bi-TiOPc (blue curves in both figures) is completely closed on Ag(111), as the silver features are barely observed in the blue curve, showing the interruption function of the dipole bilayer. Furthermore, the fluorinated feature at 45° appears at the binding energy between 9 eV and 11 eV (grey vertical column). In Fig. 6.9(b), the bi-TiOPc HOMO peak located at the BE of 1.68 eV gradually decreases with F_{16}CuPc deposition, as the penetration depth of UPS technique limits. Meanwhile, a small peak (centered at 2.05 eV) arises with F_{16}CuPc deposited on the dipole bilayer, while it broads at the final coverage (48 Å). Compared to Fig. 6.6(b), the HOMO peak of F_{16}CuPc is attributed to the multilayer signal. As no monolayer feature of F_{16}CuPc can be observed, this molecule has no interaction with Ag substrate despite the chemisorption on the F_{16}CuPc/Ag(111) interface. In Fig. 6.9(c), the vacuum levels of F_{16}CuPc / bi-TiOPc on Ag(111) remain similar as on the F_{16}CuPc on Ag(111), as the WF is shifted from 4.61 eV (bare Ag) to 4.32 eV by bilayer TiOPc deposition and remains constant with initial F_{16}CuPc deposition (up to monolayer thickness). When the coverage of F_{16}CuPc is higher than a monolayer, this molecule dominates the WF and finally leads it back to 4.51 eV. Excluding the interaction with silver substrate, F_{16}CuPc is presenting its multilayer behavior with the template TiOPc bilayer, as the WF value is similar compared with Fig. 6.6(c).

The thickness dependent XPS measurements of C 1s and F 1s core-levels are displayed in Fig. 6.10. In the figure, with the dipole bilayer TiOPc (blue curves) on Ag(111), only carbon peaks are observed and the fluorine region keeps flat. With monolayer (nominal thickness 4 Å) F_{16}CuPc deposition, there are changes in the C 1s core-level (fitting results in Fig. 6.11), and the fluorine signal arises compared to the flat curve (bi-TiOPc). This phenomenon indicates the adsorption of F_{16}CuPc molecules on the sample, as the fluorine atoms only exit in this molecule. Further deposition of F_{16}CuPc, as expected, leads to a continuous variation of C 1s spectra, the F_{16}CuPc signal (Fig. 6.11) has overtaken the TiOPc contributions with further deposition, meanwhile its F 1s curve increases in intensity, which confirms the existence of F_{16}CuPc molecules.

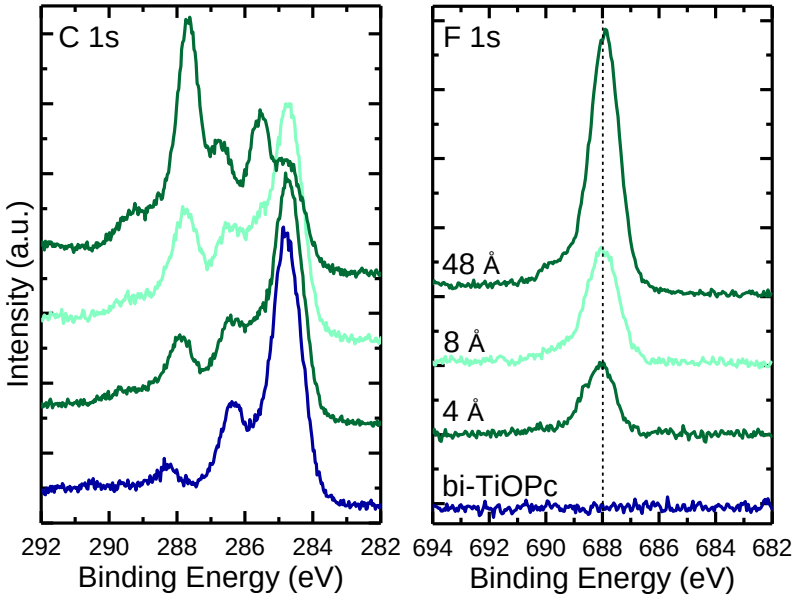

Figure 6.10: Thickness dependent XPS core-level spectra of C 1s (a) and F 1s (b). The bi-TiOPc curves are colored blue, and with further deposition of F_{16}CuPc, its monolayer (4 Å) and multilayer (48 Å) are highlighted by dark green, which is the F_{16}CuPc / bi-TiOPc (the target trilayer) and muilt- F_{16}CuPc / bi-TiOPc, respectively.

The fitting results of C 1s spectra are shown in Fig. 6.11 and the bi-TiOPc figure (Fig. 6.11a) is replotted for comparison. According to the bi-TiOPc spectrum, the trilayer system (Fig. 6.11b) is fitted into the two molecular contributions, while the area contributed by TiOPc molecules (blue curves) remains the same binding energy position as in Fig. 6.11(a). For the rest area, three peaks attributed to three species of carbon atoms in F_{16}CuPc are fitted and are identical with the multilayer behaviour of F_{16}CuPc / Ag(111) (Fig. 6.8). On the other hand, the two shake-up peaks at higher binding energies are respectively belonging to both molecules, the one located at 288.44 eV to the TiOPc molecules and the one at 289.52 eV to the F_{16}CuPc molecules. With more F_{16}CuPc deposited on the trilayer film, Fig. 6.11(c) and (d), this fitting mode can be applied, showing the same behaviour of F_{16}CuPc molecules on the bi-TiOPc / Ag(111) surface, which is due to the isolation function by strong dipole TiOPc bilayer. The fitting results of different species of carbon signal are summarized in Tab. 6.1.

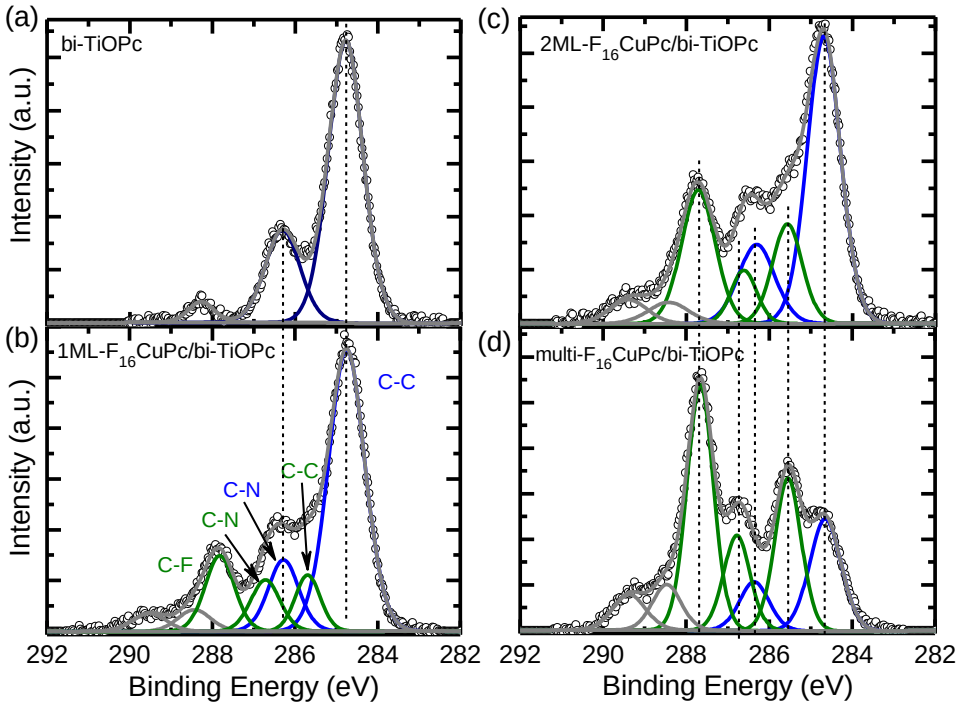

Figure 6.11: C 1s core-level spectra of (a) bi-TiOPc, (b) 1ML-F_{16}CuPc / bi-TiOPc, as well as (c) 2ML-F_{16}CuPc and (d) multilayer F_{16}CuPc on bi-TiOPc/Ag(111). The blue curves are attributed to TiOPc contribution, and green curves the F_{16}CuPc. Note that ML means monolayer.

Table 6.1: Fitting results of each peak supported for Fig. 6.11, due to the high resolution of XPS measurements, five distinctive contributions of the two molecules can be obtained.

/eV	TiOPc		F_{16}CuPc		
	C-C	C-N	C-C	C-N	C-F
bi-TiOPc	284.77	286.31	-	-	-
trilayer	284.77	286.31	285.69	286.72	287.82
2ML-F_{16}CuPc	284.69	286.31	285.57	286.62	287.71
multi- F_{16}CuPc	284.64	286.36	285.54	286.78	287.66

6.3.2 Photoelectron Properties of P4O / bi-TiOPc / Ag(111)

In the UPS full scans, Fig. 6.12(a), the substrate features decrease in intensity systematically with the increasing coverage of organic molecules, leaving only the molecular features in the spectra. From the spectra, it can be figured out that the HOMO peak generated by bi-TiOPc molecules remains the same binding energy position with P4O deposition. For details, Fig. 6.12(b) provides the zoom in valence band spectra, with coverage-dependent P4O on bi-TiOPc / Ag(111). As shown in the figure, a HOMO peak (centered at ~1.69 eV BE) dominates to TiOPc molecular

feature in the spectra. With P4O deposited on bi-TiOPc film, this peak decreases (1 Å P4O) and then increases (more than 2 Å P4O). Based on the previous studies [26, 97], P4O HOMO peaks are located at relatively higher BE positions (~3 eV), which is overlapped with the TiOPc signal in this trilayer regime so that it is difficult to determine the P4O valence band. In Fig. 6.12(c), TiOPc bilayer triggers the WF shifting to lower kinetic energy (4.32 eV), and P4O molecules further cause a weak shift back to higher kinetic energy (4.37 eV), as pure P4O film on Ag(111) has the WF at the kinetic energy of 4.65 eV. It can be concluded that a different growth morphology of P4O molecules on the bi-TiOPc dipole layer, which needs further investigations on this model. However, the UPS data show significant discrepancy with the chemisorption behaviour of P4O on Ag(111) [26, 97], while P4O on Ag illustrates a mono- and multilayer HOMO peak centered at 3.01 eV and ~4.1 eV.

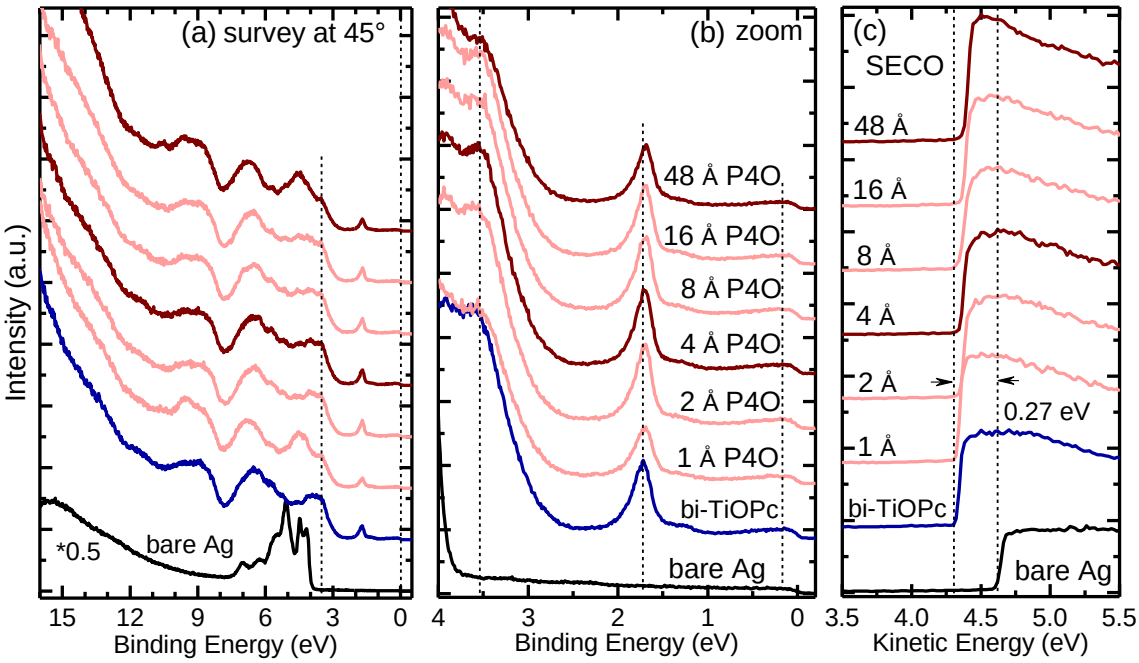

Figure 6.12: Coverage-dependent full valence band (a), zoom in valence band (b) and SECO (c) spectra of P4O on bi-TiOPc / on Ag(111), valence band spectra are measured at 45°. In the figures, substrate are colored by black, bi-TiOPc the blue curve, P4O monolayer (4 Å) and multilayer (64 Å) are highlighted by darker red.

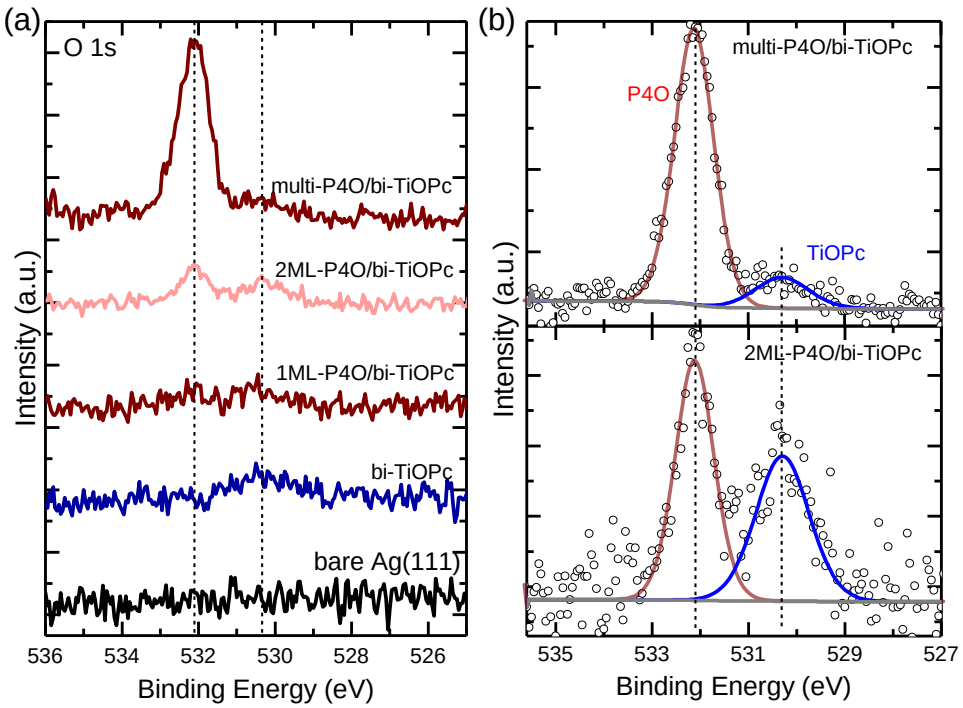

Figure 6.13: O 1s core-level spectra of multi-P4O / bi-TiOPc / Ag(111), 2ML-P4O / bi-TiOPc / Ag(111). (a) Comparison of different film thicknesses on Ag(111) substrate, (b) fitting results of two coverages.

In Fig. 6.13, the O 1s core-level signals are exhibited with the signals contained in both molecules (Fig. 6.1). The thickness dependent spectra in Fig. 6.13(a) show the evolution of oxygen signals with deposition of P4O molecules on the bi-TiOPc film. The O 1s peak at higher BE position increases with P4O deposition, thus the different contributions from these two molecules can be figured out (dashed vertical lines). The dashed line at lower BE indicates the TiOPc contribution and the higher BE peak the P4O contribution. Two spectra in this figure are fitted, as shown in Fig. 6.13(b). In the multi-P4O / bi-TiOPc spectrum, as the main contribution (BE position 532.12 eV) belong to the P4O molecules, the peak located at lower BE (530.30 eV) is attributed to TiOPc bilayer. The P4O oxygen peak remains the same as the multilayer contributions as in the references [26, 97]. This fitting mode is also applied in the 2ML-P4O / bi-TiOPc film on Ag(111), and the two domains fit well with the multi-P4O / bi-TiOPc spectrum.

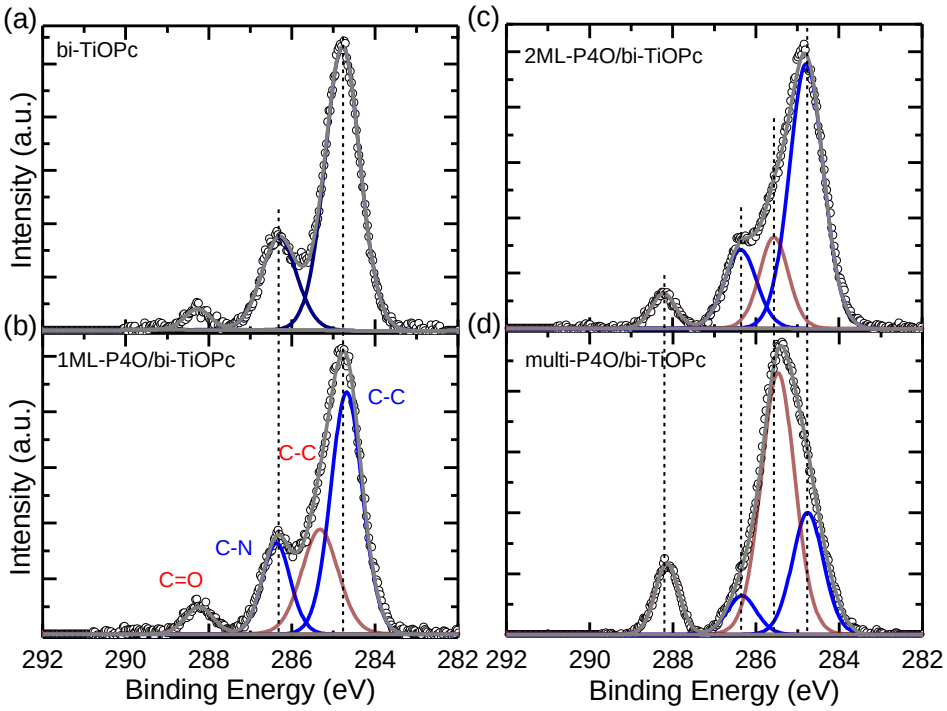

Figure 6.14: C 1s core-level spectra of (a) bi-TiOPc, (b) 1ML-P4O / bi-TiOPc, as well as (c) 2ML-P4O and (d) multilayer P4O on bi-TiOPc/Ag(111). The blue curves are attributed to TiOPc contribution, and red curves the P4O.

The fitting results of C 1s core-level spectra have been displayed in Fig. 6.14, and the detailed numbers are summarized in Tab. 6.2. For comparison, the bi-TiOPc fitting result is shown in Fig. 6.14(a). In the trilayer regime (1ML P4O/bi-TiOPc in Fig. 6.14b), we applied the fitting results (two blue curves) of bi-TiOPc on Ag(111), while the other area is then fitted into two peaks (red curves) which are dominated by two carbon species in the P4O molecules, as C-C and C=O, according to the previous studies [26, 97]. When compared to the previous reports [26, 27], the carbon signals indicate a multilayer behaviour of the P4O molecules on the bi-TiOPc layer on Ag(111). Further deposition of P4O molecules, Fig. 6.14(c, d), meanwhile, only induces to the increasing in intensity of P4O carbon signals without any shift of the peaks, which proves the same chemical environment of P4O molecules on the bilayer template surface.

To summarize the P4O / bi-TiOPc trilayer behaviour on Ag substrate, the dipole bilayer is certainly resolved the interactions between P4O molecules and Ag substrate, as reported chemisorption between them. A multilayer molecular

behaviour in the trilayer has been investigated, which is identical as the multilayer growth of pure P4O films on Ag(111).

Table 6.2: Fitting results of each C 1s peak supported for Fig. 6.18, thanks to the high resolution of XPS measurements, the distinctive contributions of the two molecules are determined.

/eV	TiOPc		P4O	
	C-C	C-N	C-C	C=O
bi-TiOPc	284.77	286.34	-	-
trilayer	284.68	286.37	285.31	288.23
2ML-P4O	284.79	286.37	285.56	288.22
multi-P4O	284.76	286.34	285.46	288.14

6.4 Discussion

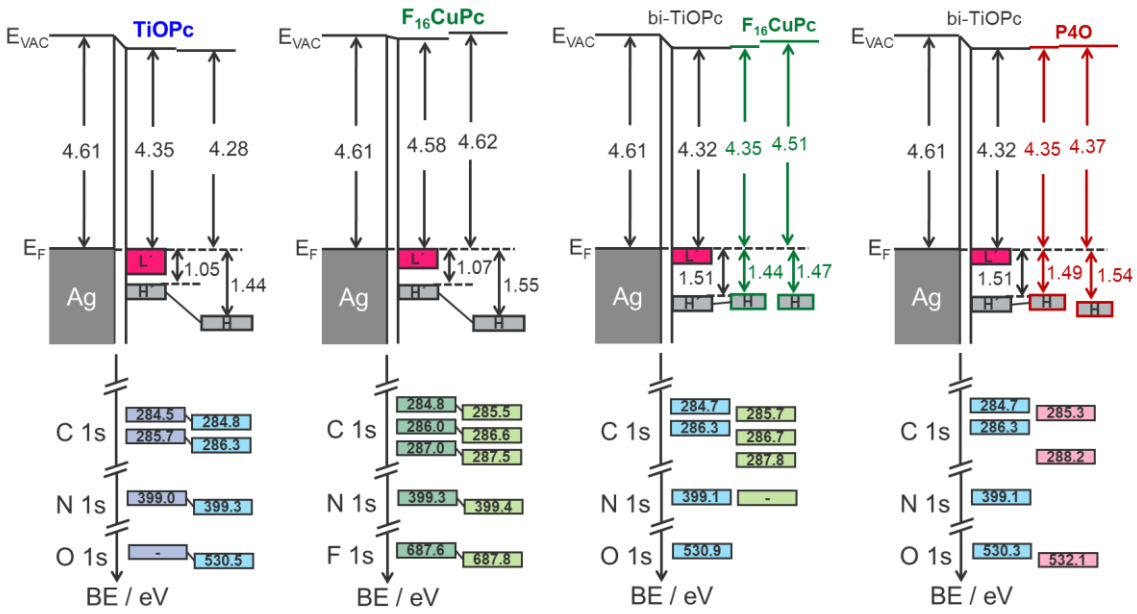

Figure 6.15: Schematics of energy level diagram and core-level positions of the interface among the four samples have been studied. On the left the Ag(111) substrate with its work function and Fermi level (E_F)are displayed. Each middle panel corresponds to a monolayer (or TiOPc bilayer) and reports the position of the HOMO and C 1s, N 1s, O 1s (F 1s) core-levels. The energy positions of HOMO (H) and the partially filled former LUMO (L') are deduced from UPS. The core-level binding energy position of C 1s, N 1s and O 1s (F 1s) are deduced from XPS.

The results of the present study are schematically summarized in Fig. 6.15 and Tab. 6.3. In Fig. 6.15, the four samples to be studied follow the order been discussed

in the former sections. In the left panel, the Ag(111) substrate is maintained at the same condition with the identical WF (4.61 eV). The electronic structure of TiOPc on Ag(111) substrate indicates a typical chemisorption behaviour: the LUMO-derived features in the monolayer is well pronounced and below the Fermi level of Ag(111). This predominates that the electrons transfer from the substrate into the former LUMO. Consequently, such a directed charge transfer leads to an interface dipole, which increases the vacuum level. However, for this sample, the vacuum level decreases by 0.26 eV, which can be caused by the combined function of charge transfer and push-back effect. Sustaining decreasing of the WF after monolayer growth indicates the different growth direction of the dipole molecule, the up-down dipole bilayer formation. In the bottom, the XPS core-levels are displayed. According to the C 1s, N 1s and O 1s core-level differences, it is then applied to distinguish the mono- and multi- layer contributions. For F_{16}CuPc molecules on Ag(111), only slightly shift of the work function is observed with monolayer thickness and has been shifted back in the multilayer thickness, revealing the larger net electron transfer from the substrate compared with TiOPc. As the layer-by-layer growth of F_{16}CuPc on Ag(111) has been proved by STM images [275], the core-level positions determined by XPS measurements further supply the way to identify the molecular behaviour of F_{16}CuPc in the trilayer system. As shown in Fig. 6.15, its C 1s signals have been well investigated and shows a shift to higher binding energy of ~ 0.6 eV of all three carbon species. However, the nitrogen and fluorine reveal smaller shift compared to the carbon species.

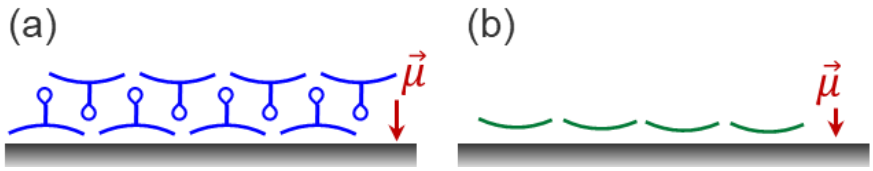

Figure 6.16: Schematics of first and second layer growth mode according to the previous studies. (a) TiOPc on Ag(111) [82], (b) F_{16}CuPc on Ag(111) [201], intramolecular distortion is indicated by molecular dipole moment.

In general, vacuum-level shifts ΔVL at organic-metal interfaces can have two contributions [22, 102, 198]:

$$\Delta VL = \Delta\Phi_{dip} + \Delta\Phi_{bond}$$

In this equation, $\Delta\Phi_{bond}$ contains the effect of the molecule-metal interaction, which is mainly caused by push-back effect and charge transfer. In Fig. 6.15, the ΔVL of TiOPc on Ag(111) is -0.32 eV over the whole deposition process. Moreover, the C 1s core-level shift in Fig. 6.3 indicates the screening effect, which is -0.10 eV. The rest of the contribution turns to molecular dipole moment (Fig. 6.16a) and charge transfer (L'), of which we cannot define the exactly number in our measurements. When F_{16}CuPc is deposited on Ag(111), the VL remains constant (0.01 eV in Fig. 6.15, smaller than the setup resolution). However, the same effects result the constant VLs, i.e. molecular dipole moment, charge transfer, screening effect. Moreover, the carbon core-level has been shifted by -0.64 eV according to the XPS results. When comparing the two molecules on Ag(111), the molecular dipole moment (Fig. 6.16) of TiOPc is relatively larger than that of F_{16}CuPc, Ti=O bond vs intramolecular distortion. On the other hand, the screening effect of F_{16}CuPc dominates more in the vacuum level during growth. Nevertheless, without a thorough theoretical study on both molecules, it is hard to quantify all the effects on the VL shifts.

In the trilayer systems, since the bi-TiOPc dipole layer is obtained by desorption process, as investigated by previous studies [261, 276], it can be confirmed as a well-ordered bilayer on Ag(111). In particular, the F-LUMO is still visible in the TiOPc bilayer but with weaker intensity compared to its monolayer coverage. With deposition of monolayer F_{16}CuPc molecules, another HOMO peak arises, which is in line with the multilayer behaviour of F_{16}CuPc compared to thickness dependent results of F_{16}CuPc / Ag(111). Moreover, the more F_{16}CuPc deposition also leads to a higher WF, as well as its multilayer properties on the same substrate. In the core-levels, likewise, the three carbon species are in good agreement with the pure film grown on Ag. The nitrogen core-level is not possible to fit due to the same chemical environment in both phthalocyanine molecules. In the P4O / bi-TiOPc trilayer, despite the minor variation determined by UPS (WF and HOMO position), XPS results derive meaningful results: for the C 1s core-level results, the bilayer TiOPc signals remain the same as in the F_{16}CuPc / bi-TiOPc trilayer. According to both C 1s and O 1s core-level spectra, monolayer P4O on the sample reveals its multilayer behaviour, which can be explained by the isolate function regarding to the well-

ordered TiOPc dipole bilayer. It can be concluded that in the two trilayer systems, F_{16}CuPc and P4O exhibit the same multilayer properties, despite their chemisorption features directly on Ag(111).

Table 6.3: Summary of work function (WF) and valence band (VB, HOMO onset) binding energies extracted from UPS measurements. The fifth sample, F_{16}CuPc / TiOPc bilayer is also included for comparison, more discussion see Appendix C.

/eV		bare Ag	adlayer	1 Å	2 Å	4 Å	8 Å	16 Å	48Å	64 Å
F_{16}CuPc	VB	-	-	1.00	1.08	1.07	1.38	1.35	-	1.55
	WF	4.61	-	4.61	4.62	4.58	4.58	4.60	-	4.62
TiOPc	VB	-	-	1.01	0.99	1.05	1.50	1.42	-	1.44
	WF	4.61	-	4.51	4.44	4.43	4.33	4.31	-	4.28
P4O/bi-TiOPc	VB	-	1.49	1.51	1.53	1.54	1.53	1.52	1.54	-
	WF	4.62	4.32	4.32	4.34	4.35	4.35	4.37	4.37	-
F_{16}CuPc/bi-TiOPC	VB	-	1.51	1.51	1.48	1.49	1.48	1.48	1.47	-
	WF	4.61	4.32	4.34	4.35	4.35	4.38	4.40	4.51	-
F_{16}CuPc/ TiOPc	VB	-	0.97	1.08	1.11	1.10	1.07	-	-	-
	WF	4.62	4.5	4.51	4.46	4.39	4.33	-	-	-

6.5 Conclusion

To conclude, we have carried out studies on coverage-dependent deposition of TiOPc / Ag(111) and F_{16}CuPc / Ag(111), particularly focused studies on the properties of two trilayers, F_{16}CuPc / bi-TiOPc and P4O / bi-TiOPc on Ag(111). Our measurements have shown that both TiOPc and F_{16}CuPc molecules are chemisorbed on Ag(111), as indicated by UPS and XPS, where a filled F-LUMO is observed as well as different contributions of C 1s core-level spectra. When the trilayer is assembled, non-interaction between the second molecules (F_{16}CuPc / P4O) and Ag(111) occurs as they exhibit the multilayer adsorption behaviours, even both molecules are chemisorbed on Ag(111). This result, on the other hand, shows ordered growth on the chemisorptive substrate in the trilayers, with a strong dipole bilayer as the template. However, further experimental research, like STM and XSW measurements, will be more helpful to fully understand the trilayer systems. In particular, for cases studied here, it is possible to interrupt even the chemisorption mechanism, by building a strong enough template layer, in this case a dipole molecular bilayer. In the future, there is the possibility to carry out studies on the

ideal crystalline coinage metal electrodes, in order to study intrinsic molecular properties without any limitation from the substrate.

Part III

Summary and Outlook

7. SUMMARY AND OUTLOOK

Since the invention of (opto)electronic devices, plenty of scientists have been attracted to explore and improve their properties. For many electronic devices, we have to fully understand their core issues, which is the electronic properties and structural information on the surface and interfaces, in order to continuously improve the efficiency and discover/synthesize suitable materials.

7.1 Summary

In this thesis, based on the excellent techniques, we have carried out studies on three inequivalent groups of heterostructures, which present three possibilities of the growth behavior on the molecular scale. In the unique UHV systems, UPS, XPS, XSW and LEED measurements are adopted as the exploring tools. Accordingly, two bilayer systems are studied with these experimental methods, as the first case shows orderly growth behavior, which gives us the opportunity to overall study the behavior of the specific molecule. Apart from that, in the second group of bilayer systems, donor-acceptor counterparts present a mixed adsorption mode in spite of the weakly interaction substrate. To further study the heterostructures, the trilayer is introduced to prevent the influence from substrate.

According to the detailed analysis of the mentioned experimental research, the results are summarized in the following:

As a widely used electron acceptor material, F_{16}CuPc is studied with it monolayer regime on Au(111), as well as its bilayer regimes on the same substrate, with P4O and PTCDI as the insertion layer. As measured and analyzed by XSW technique, the intrinsic planar molecule (F_{16}CuPc) shows a significant distortion on Au(111) with its central Cu atom located below and F atoms above the average adsorption distance, C atoms in three species are in analogy with this trend. With the intermediate layer inserted, P4O or PTCDI monolayer, F_{16}CuPc adsorbs with an inverted distortion as the second layer on Au(111). The XPS results only indicate the physisorption of the three molecules on the substrate, however, UPS results gives us

the valence band information and the vacuum level shift. By analyzing UPS data, the molecular dipole moment has been considered in accordance with the XSW results. Overall, we have shown that also in the physisorptive regime, the substrate plays a crucial role in the conformation of adsorbates.

Since the weaker interacting bilayers allow us to understand the behavior of specific molecules, we took the donor-acceptor (PEN-PFP) counterparts to focus on their bilayer properties. The PEN-PFP bilayers have been grown on Au(111), with different grown orders. By photoelectron spectroscopy (UPS and XPS) studies, the valence band with its various HOMO contributions and the core-level shifts confirm the mixture formation within the PEN: PFP bilayers, the same as other weakly interacting substrate (HOPG). Further evidence has been found by XSW, as it is also hypothesized in view of the same XSW results of the two bilayer systems. Since the arrangement in organic molecules is of most important for controlling the (opto)electronic devices, and the molecular diffusion might be detrimental to some devices. Predicting the order in organic heterostructure is, thus, essential for rational device design.

As the bilayer samples demonstrate substrate influencing and molecular mixture appearance not only on the chemisorptive but also on the physisorptive substrate, we managed a way to prevent the influence from substrate. By this purpose, a dipole TiOPc-bilayer has been introduced as the template layer. Moreover, F_{16}CuPc and P4O are studied growing on the dipole bilayer on Ag(111) substrate. Both of them has been investigated to be chemisorbed on Ag(111), and display a physisorption behavior on the TiOPc-bilayer, whereas only multilayer signals have been observed. In particular, the P4O molecules on bi-TiOPc / Ag(111) are suggested a different morphology instead of general flat-lying layer by layer growth, which needs further investigation on this system. In general, we demonstrate a method to prevent the interaction from organic molecules to the substrate. Moreover, this experiment also shows that the substrate can only effect until the second layer, even the charge transfer happens in the first layer. The fundamental studies on the organic molecules can either consider an interruption layer or ignore the interface interaction by counting the behavior of the third layer. From the device

prospect, a modification layer on the metal electrode can be employed to reach the required property.

In conclusion, the growth behavior of organic molecules varies dramatically within the variety of organic molecules and substrates, only few cases are studied in this work. However, our work generally include different phenomena which could occur among these interfaces, i.e. orderly bilayer growth, molecular exchange/mixture and the block function by dipole bilayer. Therefore, we hope our studies can motivate more research on the molecular growth, as well as interface electronic properties, in case to further enhance the efficiency of (opto)electronic devices.

7.2 Outlook

In this research, we employed photoelectron spectroscopy based techniques, to study the adsorption behavior and electronic structures of the interface in the heterostructures. Generally, the inert substrate is used to avoid any effect by strong interaction, as well as employing the dipole bilayer to block the interaction. For organic molecules on the coinage metal substrates, we have investigated the adsorption properties, molecular arrangement and of the utmost the intermolecular effect in the heterostructures. For several specific molecules, we have carried out the research and determined the conclusion. However, the work in the thesis is not perfect, since there are still numerous uncertainties and challenges that require further research and verification.

In the beginning, OSCs represent diverse electronic structures, which require fundamental research. Meanwhile the new materials are synthesized, and need more research on the growth behavior and electronic properties.

Secondly, it has become one of the main reasons that different molecular morphology can influence the device properties. When it turns to the nano-sized materials, the setup is extremely demanding, as well as ultra-high vacuum technology. Both the development of the setup and the exploration of the organic molecular materials are worth sparing no effort to discover. As the major technique employed in this thesis, XSW technique is facing many limitations, e.g. its

measurement depth is only a nanometer, which limits a device-like sample to be studied.

Last but not the least, the work carried out in this thesis only determines preliminary results on the growth behavior of the heterostructures, while there are more concepts on the intramolecular variation that need to be considered. For different materials and different substrates, there are many unanswered questions on their interfaces. Only until scientists have thoroughly understood the characterization of these materials and mutual effect between heterostructures, could that provide a solid and powerful theoretical basis for the applications of devices in the future.

APPENDIX

A. Bilayer Formation: Molecular Exchange

The results presented in this section were published in Ref. [26]. The results shown in this section are the continuous study from the author's master thesis, in collaboration with Prof. Schreiber, and have been finished during the PhD study.

As introduced in Section 2.2, the indicator is generated with the studied two bilayers, that CuPc / P4O bilayer forms the ordered formation, and CuPc / P2O bilayer the molecular exchange process, shown in Fig. A.1, with molecular chemical structures in the figure.

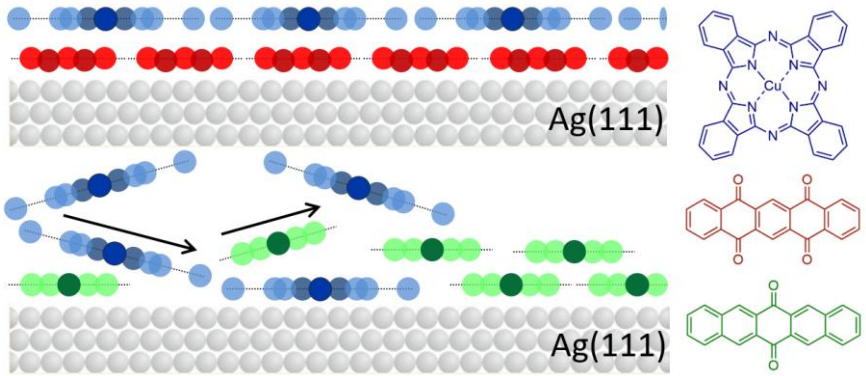

Figure A.1: Bilayer formation (top) vs molecular exchange (bottom). In both cases, CuPc (blue) has been vacuum-sublimed on a closed monolayer of P4O (red) and P2O (green) on Ag(111). On the right side, the chemical structures of CuPc, P4O and P2O are shown.

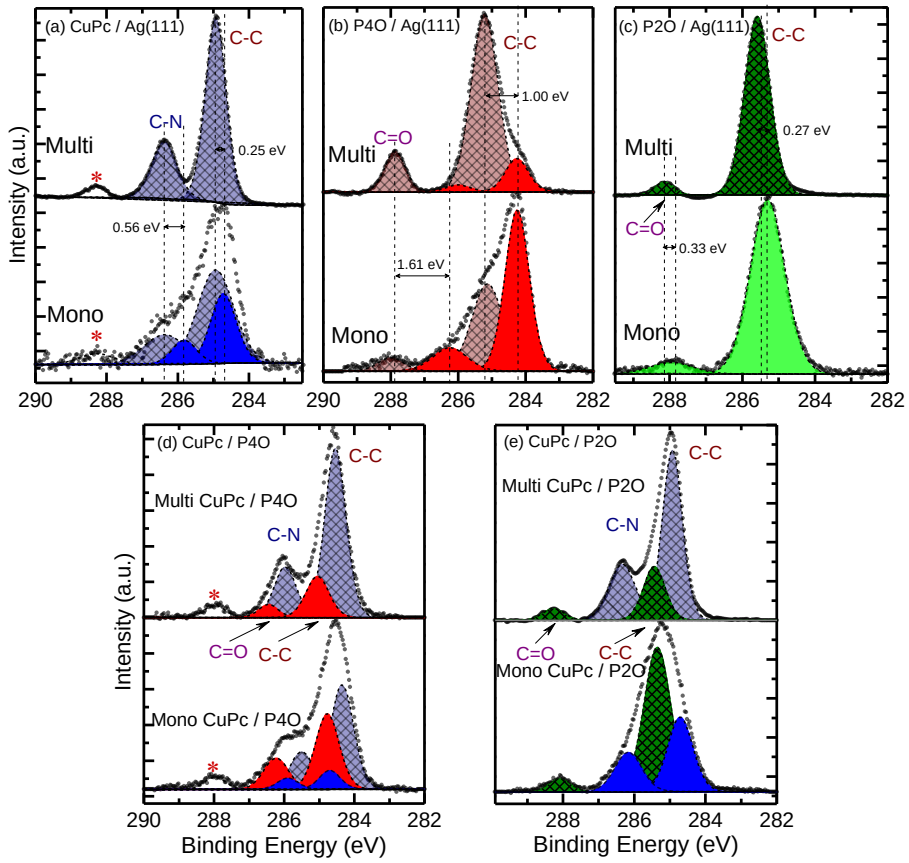

Figure A.2: C 1s core-level spectra for homostructures (top row, CuPc in blue, P4O in red, and P2O in green) and heterostructures (bottom row). The nominal coverages are 48 Å (multi) and 4 Å (mono). The fits are color-coded to mark contributions from the different COMs and to distinguish between monolayer (full color) and multilayer (pale color with pattern) contributions. The red star (*) marks a shake-up satellite of CuPc. For the heterostructures, CuPc was deposited on a PxO monolayer prepared via annealing a thick film.

C 1s core-level spectra of CuPc, P4O, P2O on Ag(111), shown in Fig. A.2(a-c), and the CuPc / P4O, CuPc / P2O heterostructures in Fig. A.2(d, e), respectively. In Fig. A.2(a-c), the core-level BE positions are highlighted by vertical dashed lines, where the core-level shift can be easily determined and compared. In Fig. A.2(d, e), monolayer PxO is prepared by desorption process with roughly four monolayers (nominal thickness 16 Å) thicknesses, and the CuPc molecules are deposited subsequently. Since it is hard to disentangle the different carbon contributions between PxO and CuPc molecules, we refrain further discussion on the spectra.

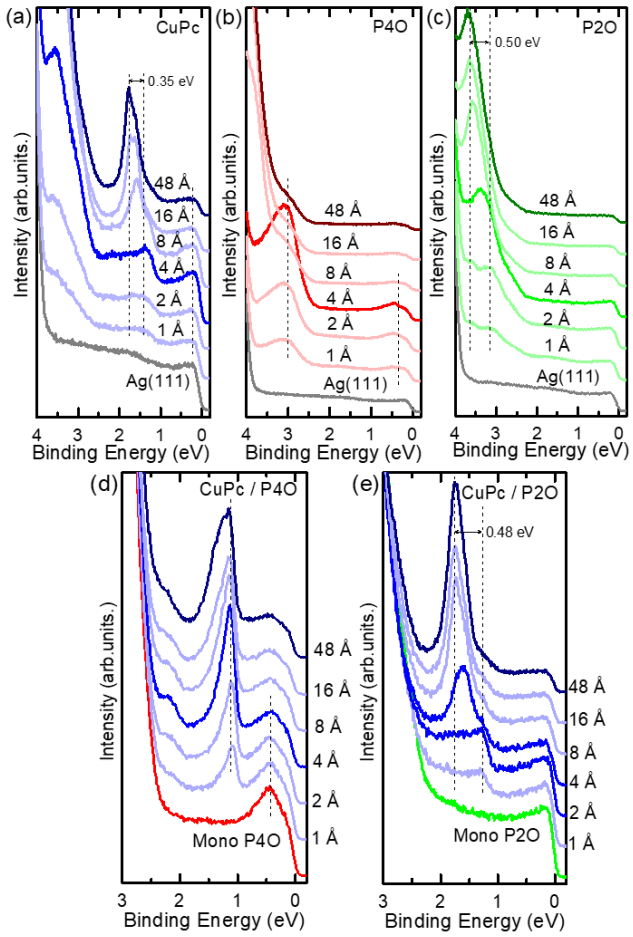

Figure A.3: (a-c) UP spectra for stepwise deposited COMs on Ag(111). Monolayer and multilayer spectra are highlighted by darker lines. (d, e) UP spectra for stepwise deposited CuPc on monolayers of PxO / Ag(111) (prepared by thermally desorbing the multilayers). For CuPc on P2O / Ag(111), also the first CuPc spectrum dominated by multilayer features is highlighted. Vertical lines highlight the position of the HOMO and the F-LUMO.

The valence band spectra for CuPc, P4O, P2O on Ag(111) have been displayed in Fig. A.3(a-c), and the CuPc / P4O, CuPc / P2O heterostructures in Fig. A.3(d, e), respectively. In Fig. A.3(a, b), the F-LUMO peaks near Fermi edge indicate the charge transfer between the COMs and Ag interface, therefore the two molecules are chemisorbed on Ag(111). Meanwhile, no clear peaks can be seen in Fig. A.3(c), the physisorption is determined, reveal a weaker interaction of P2O on Ag(111) than that of CuPc. The heterostructure spectra of CuPc / P4O only exhibit multilayer HOMO peak of CuPc molecules, while its monolayer HOMO peak appears in the CuPc / P2O bilayers.

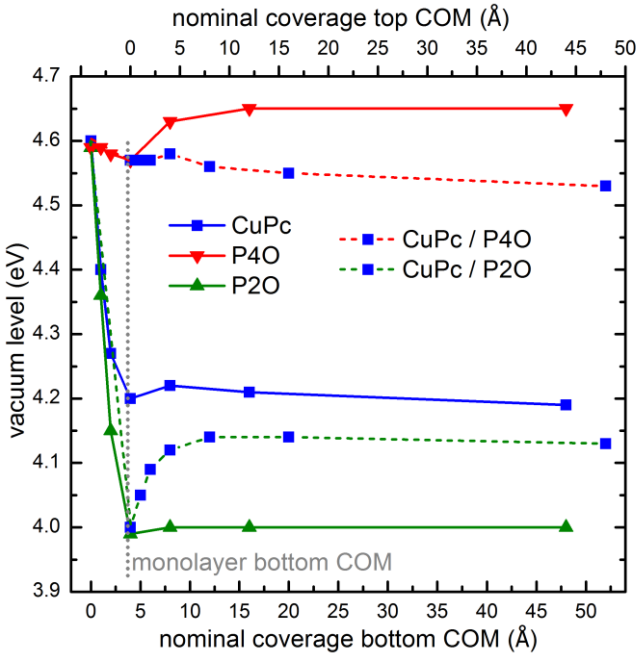

Figure A.4: Coverage-dependent evolution of vacuum levels wrt the Fermi level for all investigated thin films on Ag(111). "Bottom" and "top" COM denote the deposition sequence and not the actual arrangement of the thin films. The solid lines correspond to the homomolecular systems and are referred to the bottom abscissa. The dashed lines describe the heteromolecular systems created upon the deposition of increasing coverages of CuPc (referred to the top abscissa) on a full monolayer of PxO.

The vacuum level position with increasing film coverage (Fig. A.4) provides the insight into the interfacial interaction strength at the organic / metal and organic / organic interfaces. The solid curves represent the pure films grown on Ag(111), we can determine the ΔVL through these curves. Moreover, deposition of CuPc on P4O / Ag (111) does not result in notable changes of the weak coupling at this interface. Deposition of CuPc on P2O / Ag(111) increases the VL due to the charge transfer between CuPc and Ag(111). The shift saturates for a nominal CuPc coverage of 8 Å is almost the same as the value of CuPc deposited directly on Ag(111).

B. F4PEN Adsorption Properties on Ag(111)

The results presented in this section were published in Ref. [277]. The results shown in this section are followed by Dr. Antoni Franco-Cañellas. Full data set of this section can be found in the dissertation of Dr. Franco-Cañellas, Universität Tübingen, 2018 [177]. Part of these data has been published on *Phys. Rev. Mater.*, 2018 and can be found in the **List of Publications**. Further analysis has been carried out on the unpublished part and finally been published.

We have studied the structural and electronic properties of 2,3,9,10-tetrafluoropentacene (F4PEN) on Ag(111) via XSW, LEED, UPS and XPS. Fluorination is believed to decrease the coupling strength between the substrate and the adsorbate [28, 31, 227]. In this context, pentacene (PEN) and perfluorinated pentacene (PFP) have almost identical optical gaps in thin films (1.85 eV and 1.75 eV) [109, 246] and the experimental gas phase IEs (measured by UPS) are 6.59 eV [278] and 7.50 eV [279], so that partially fluorinated pentacene -F4PEN- come up to our mind. As this molecule has been verified to be physisorbed on Au(111) [280] and chemisorbed on Cu(111) [206], the intermediate substrate Ag(111) is chosen in the current work.

The determination of vertical adsorption heights of F4PEN in (sub)monolayers on Ag(111) relies on high resolution core-level spectra which are shown in Fig. B. 1. Following the assignment of F4PEN core-levels on Cu(111) [206], the C 1s peak centered at 287.29 eV binding energy (BE) is assigned to carbon atoms bound to fluorine atoms (C-F) and the main peak centered at 284.88 eV to carbon atoms in the backbone of F4PEN (C-C). The symmetric F 1s peak is centered at 687.47 eV. Figure B.1 shows the photoelectron yield. F4PEN adsorbs in an essentially planar geometry with averaged vertical adsorption distances of around 3.00 Å for carbon and fluorine atoms. The bonding distances are summarized in Table B. 1 together with literature values of PEN and PFP. In general, the adsorption distance of F4PEN in (sub)monolayers on Ag(111) is similar to that of PEN and PFP on the same substrate. Due to the lower coherent fraction (f_H) values obtained in this system, a possible tilting mode has been determined according to Ref. [198], shown in Fig. B.2.

Viewed along the short molecular axis, the fluorine atoms are separated into two species, one is higher than average d_H (3.05 Å) and the other one is lower. The tilted angle is approximately 20°, for specific numbers see Fig. B.2. However, since the f_H can be influenced by a variety of factors, e.g. static effect and molecular dynamics, Fig. B.2 only suggests the ideal situation without any other effects.

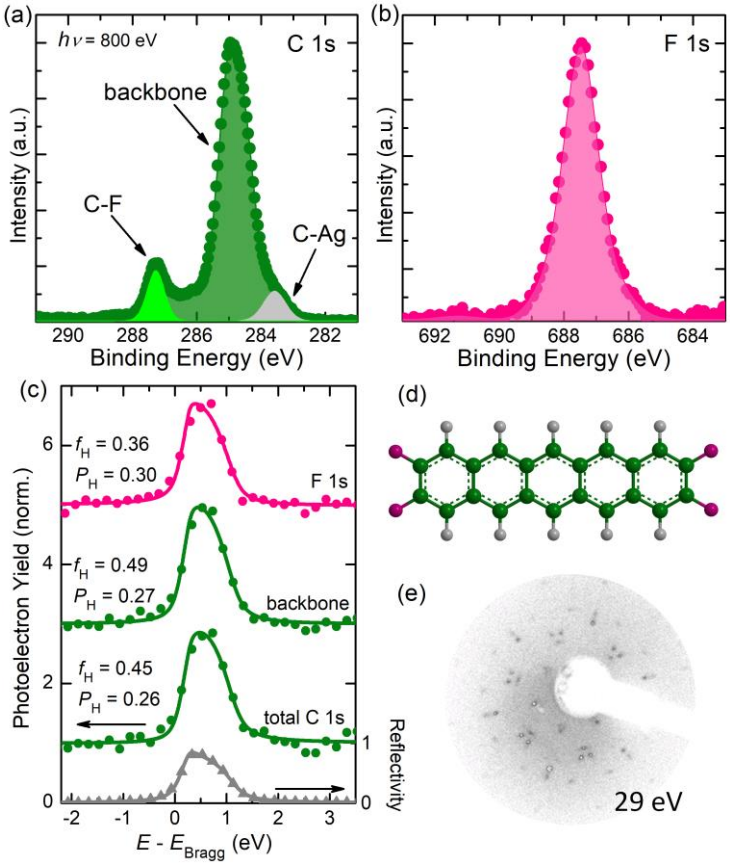

Figure B.1: (a) C 1s and (b) F 1s core-levels of F4PEN in monolayers on Ag(111) measured at DLS. (c) Reflectivity and photoelectron yield (Y_p) as function of photon energy ($h\upsilon$) relative to Bragg-energy (E_{Bragg} = 2630 eV) for a (sub)monolayer (<2 Å) F4PEN thin film on Ag(111). For each element the coherent position (P_H) and the coherent fraction (f_H) are given. (d) Chemical structure of F4PEN. (e) LEED patterns for F4PEN on Ag(111) with nominal thickness of 4 Å, measured at 295K with a beam energy of 29 eV. The LEED pattern is almost the same as PEN on Cu(111) [200].

Table B.1. Summary of element-specific vertical adsorption heights (d_H/Å) of (fluorinated) pentacene in (sub)monolayers on Ag(111) measured with the XSW technique. Values for PEN and PFP are taken from Refs. [281] and [282], respectively.

coverage	element	PEN	F4PEN	PFP
low	C	2.98	3.00	3.16
	F	-	3.05	3.16
high	C	3.12	2.97	-
	F	-	2.93	-

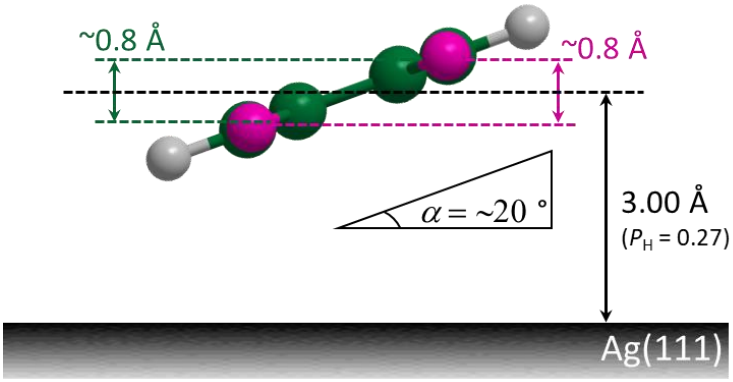

Figure B.2: The sketch of F4PEN adsorbed on Ag(111) explaining the relatively low f_H values in the experiment. Our simulation suggests that the molecules are tilted less than ~20° around the long molecular axis. The schematic show a view along the long molecular axis of F4PEN (molecular size ~ 5.44*16.28 Å²).

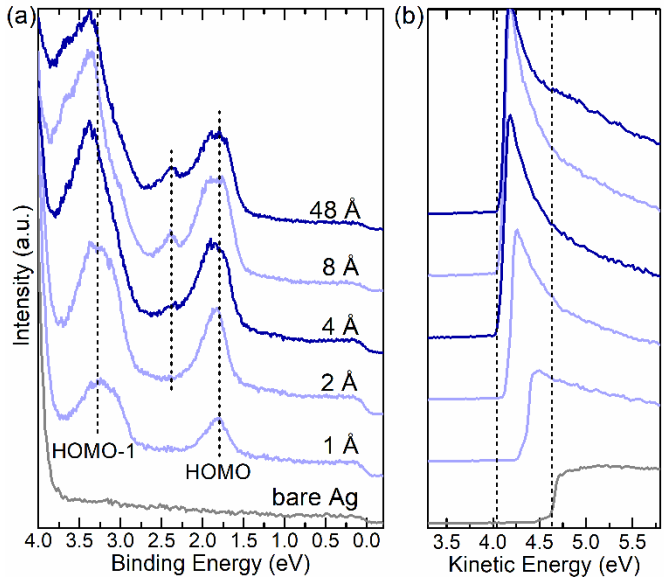

Figure B.3: Valence band (a) and secondary electron (b) region of UPS spectra of F4PEN on Ag(111). In (a) the nominal mass thickness is denoted.

Figure B.3 shows the UPS valence band region (a) and the SCEO spectra (b). The valence band can be determined into HOMO (~ 1.56 eV) and HOMO-1 (~ 2.83 eV) levels. For thicknesses of 4 Å and higher a third peak emerges at the high BE shoulder of the HOMO-derived peak. Interestingly, the BE maxima of these two peaks do not change with increasing coverage (as highlighted by vertical lines in Fig. B.3), while they broaden simultaneously. The HOMO-1 peak shows a shift to higher BE with increasing coverage, indicating a deeper lying valence electron feature. The SECO spectra (Fig. B.3b) allow us to determine the VL position above E_F, which is reduced from an initial value of 4.62 eV (bare Ag) to 4.05 eV for the monolayer (nominal thickness 4 Å) F4PEN coverage and keeps constant. The VL decrease of 0.57 eV is similar to that of PEN and PFP thin films on the same substrate [200, 282] and can be mainly ascribed to the so-called push-back effect [225, 226, 283].

In conclusion, in the monolayer regime on Ag(111) (partial) fluorination of pentacene does not notably affect the adsorption geometry and the energy-level alignment. This unexpected finding is most likely due to the interplay of substrate, induction and electrostatic contributions to solid state polarization. Our results show that the rational of "decoupling by fluorination" requires a threshold of organic-metal interaction strength as can be seen by monolayers of the PEN, F4PEN and PFP on Cu(111), which are, indeed, distinctively different [206, 227]. Moreover, the strong intramolecular polar C-F bond has an eminent impact on the multilayer structure of the pentacene derivatives on Ag(111), which are π-stacked for PFP and F4PEN, whereas PEN adopts a herringbone arrangement. For PFP this has been ascribed to attractive quadrupole interactions between adjacent PFP molecules [209, 284] and it seems to be the case for partial fluorination, as well. The differences in thin film structure are also reflected in the electronic structures, which are distinctively different in multilayers on Ag(111). Our results highlight that even in the case of weak organic-metal interaction, the fluorine substitution significantly affects organic thin film growth beyond the first layer as well as the multilayer electronic structure.

C. F_{16}CuPc / TiOPc Bilayer on Ag(111)

As discussed in Chapter 6, the trilayer structures have been studied by photoelectron spectroscopy techniques, indicating a new method to block chemisorption by inserting a dipole bilayer. Meanwhile, we also grew a bilayer on Ag(111) substrate, which is F_{16}CuPc / TiOPc bilayer. The UPS and XPS data are shown here to further characterize the molecular properties.

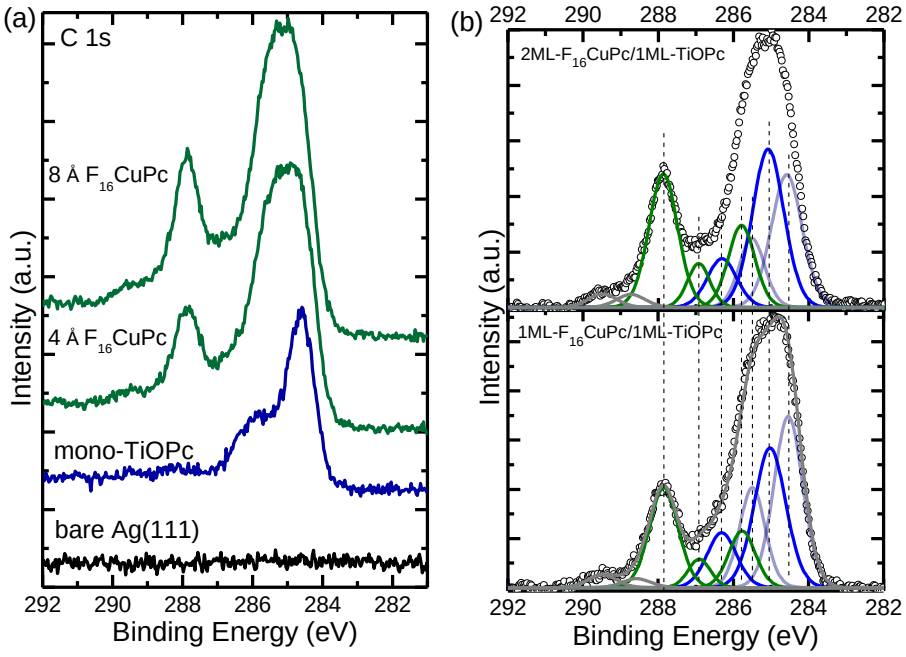

Figure C.1: C 1s core-level spectra of mono-TiOPc, 1ML (4 Å) and 2ML (8 Å) F_{16}CuPc on mono-TiOPc, the bare Ag(111) is shown as well. (a) Comparison of different COM film on Ag(111) substrate, (b) the fitting results of the heterostructures.

The XPS results of C 1s core-level spectra (Fig. C.1) are first shown to present the general information of this bilayer. In Fig. C.1(a), the comparison of different thicknesses are exhibited, no signals in the bare Ag(111) curve and continuously changes with molecular deposition. With mono-TiOPc deposited, C 1s signals appear and the main peak broadens with monolayer (1ML / 4 Å) F_{16}CuPc, and a small peak arises at higher binding energy, while these are due to the F_{16}CuPc contributions. As shown in Fig. C.1(b), the fitting results of 1ML-F_{16}CuPc / 1ML-TiOPc and 2ML F_{16}CuPc / 1ML-TiOPc on Ag substrate, respectively. In the figure, we fitted the

spectra according to the Chapter 6 and the mono-TiOPc results, the green curves belong to the F_{16}CuPc molecules and blue curves the TiOPc molecules. In addition, the chemisorbed TiOPc on Ag(111) can be distinguished by different interaction environment, as some molecules have charge transfer with the substrate are shown in lighter blue and the rest are in darker blue. No further interaction between the two molecules can be obtained as the different fitting curves remain the same position, as highlighted by the vertical lines.

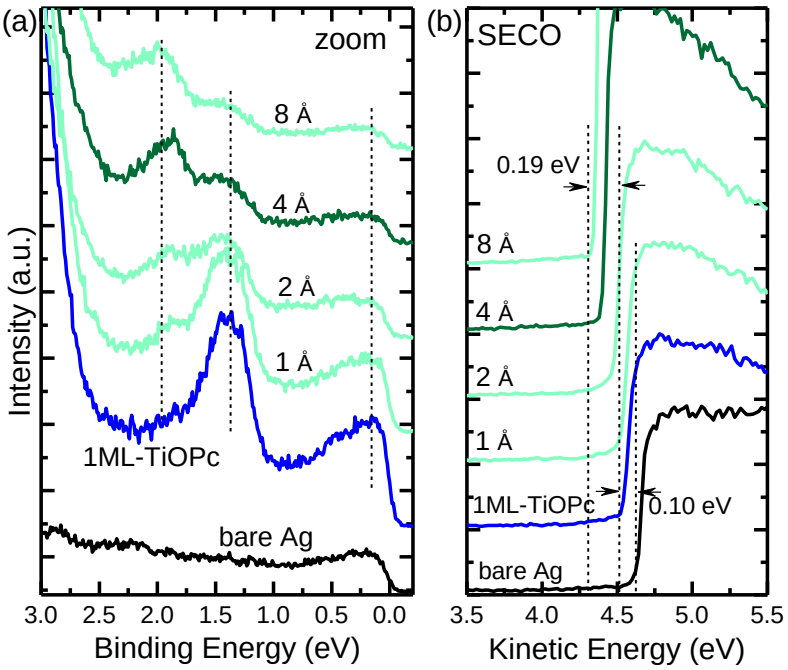

Figure C.2: (a) Zoom in valence band and (b) SECO spectra of thickness-dependent F_{16}CuPc deposited on mono-TiOPc / Ag(111). In the figures, substrate are colored by black, mono-TiOPc the blue curve, F_{16}CuPc monolayer (4 Å) is highlighted by darker green.

Figure C.2 represents the valence band (a) and vacuum level shift (b) results. As shown in Fig. B.2(a), the monolayer HOMO peak can be determined in the 1ML-TiOPc spectrum, which is broadening at the binding energy of roughly 1.35 eV. With F_{16}CuPc deposited, this broad peak decreases and the other peak at higher binding energy (1.96 eV) arises. Compared to the coverage-dependent measurement of F_{16}CuPc on Ag(111), this is assigned to the multilayer HOMO contribution of the molecule. The brief discussion indicate an orderly bilayer growth morphology of the

sample we prepared. However, in Fig. C.2(b), the VL is shifted from 4.64 eV (bare Ag) to 4.52 eV (1ML TiOPc), and it is shifting with F_{16}CuPc deposition up to the final coverage. This varies to the trilayer geometry as F_{16}CuPc molecules lead the WF back to lower kinetic energy. As being observed the multilayer growth of F_{16}CuPc molecules, the continuous shifting of VL needs to be carefully considered. When we compare these results with bi-TiOPc / Ag(111), as the second layer of TiOPc molecules also causes the continuously VL shift, we consider the same packing mode of F_{16}CuPc on the TiOPc layer (Fig. C.3).

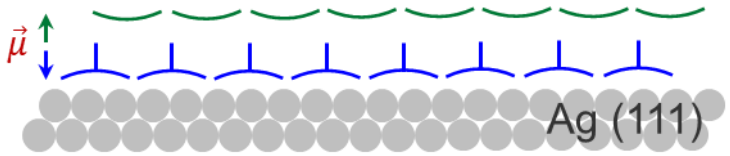

Figure C.3: Sketch of F_{16}CuPc / TiOPc bilayer growth geometry determined by the photoelectron spectroscopy results. The molecular dipole moments ($\vec{\mu}$) are adopted with the same color code of each molecule. Blue structure is referred to TiOPc molecules and green structure is referred to F_{16}CuPc molecules.

To briefly summarize the growth mode of F_{16}CuPc / TiOPc on Ag(111), an ordered bilayer is formed as deposition steps, as shown in Fig. B.3. The UPS and XPS measurements have proved this behavior. In particular, the VL shift can be ascribed as the replaced packing mode from bi-TiOPc system, the F_{16}CuPc molecules are assigned the identical behavior, the molecular dipole moment (green arrow), same as the second TiOPc layer on the mono-TiOPc layer.

LIST OF ABBREVIATIONS

Miscellaneous

BE	binding energy
CL	core-level
COM	conjugated organic material
CT	charge transfer
D-A	donor-acceptor
d_H	adsorption distance
DOS	density of state
EA	electron affinity
E_F	Fermi level
e-gun	electron gun
EIB	electron injection barrier
E_K	kinetic energy
ELA	energy level alignment
E_{vac}, VL	vacuum level
FWHM	the full width at half maximum
HIB	hole injection barrier
HOMO	highest occupied molecular orbital
IE	ionization energy
LUMO	lowest unoccupied molecular orbital
MCP	microchannel plate
OFET	organic field effect transistor
OLED	organic light emission diode
OMBD	organic molecule beam deposition
OPV	organic photovoltaic
Org.	organic
OSC	organic semiconductor
P_H	coherent position
QCM	quartz crystal microbalance
SECO	secondary electron cut-off
UHV	ultra-high vacuum
UV	ultraviolet
VB	valence band
WF, Φ	work function
Y_P	photoelectron yield

Materials

CuPc	copper-phthalocyanine
F_{16}CuPc	copper-hexadecafluorophthalocyanine
P2O	6,13-pentacenequinone
P4O	5,7,12,14-pentacenetetrone
PEN	pentacene
PFP	perfluoropentacene
PTCDA	perylene-3,4,9,10-tetracarboxylic dianhydride
PTCDI	perylene-3,4,9,10-tetracarboxylic diimide
TCNQ	tetracyanoquinodimethane
TiOPc	titanyl-phthalocyanine
Ag	silver
Au	gold
Cu	copper
Mg	magnesium
HOPG	highly oriented pyrolytic graphite

Experimental Methods

ARUPS	angle-resolved ultraviolet photoelectron spectroscopy
HXPS	hard X-ray photoelectron spectroscopy
LEED	low-energy electron diffraction
NIXSW	normal-incidence X-ray standing wave
SXPS	soft X-ray photoelectron spectroscopy
TDD	theory of dynamical diffraction
XPS	X-ray photoelectron spectroscopy

BIBLIOGRAPHY

[1] S.R. Forrest, The path to ubiquitous and low-cost organic electronic appliances on plastic, Nature, 428 (2004) 911-918.
[2] I. McCulloch, Organic Electronics, Adv. Mater., 25 (2013) 1811-1812.
[3] C.W. Tang, S.A. VanSlyke, Organic electroluminescent diodes, Appl. Phys. Lett., 51 (1987) 913-915.
[4] A. Dodabalapur, L. Torsi, H.E. Katz, Organic Transistors: Two-Dimensional Transport and Improved Electrical Characteristics, Science, 268 (1995) 270.
[5] K. Kudo, D. Xing Wang, M. Iizuka, S. Kuniyoshi, K. Tanaka, Schottky gate static induction transistor using copper phthalocyanine films, Thin Solid Films, 331 (1998) 51-54.
[6] F. Würthner, M. Stolte, Naphthalene and perylene diimides for organic transistors, Chemical Communications, 47 (2011) 5109-5115.
[7] A. Tan, P. Zhang, Tailoring the Growth and Electronic Structures of Organic Molecular Thin Films, J. Phys.: Condens. Matter, 31 (2019) 503001.
[8] S.R. Forrest, M.E. Thompson, Introduction: Organic Electronics and Optoelectronics, Chem. Rev., 107 (2007) 923-925.
[9] J.X. Tang, C.S. Lee, S.T. Lee, Electronic structures of organic/organic heterojunctions: From vacuum level alignment to Fermi level pinning, J. Appl. Phys., 101 (2007).
[10] P.I. Djurovich, E.I. Mayo, S.R. Forrest, M.E. Thompson, Measurement of the lowest unoccupied molecular orbital energies of molecular organic semiconductors, Org. Electron., 10 (2009) 515-520.
[11] G. Heimel, I. Salzmann, S. Duhm, N. Koch, Design of Organic Semiconductors from Molecular Electrostatics, Chem. Mater., 23 (2011) 359-377.
[12] A. Hinderhofer, F. Schreiber, Organic-Organic Heterostructures: Concepts and Applications, ChemPhysChem, 13 (2012) 628-643.
[13] A. Hinderhofer, T. Hosokai, C. Frank, J. Novák, A. Gerlach, F. Schreiber, Templating Effect for Organic Heterostructure Film Growth: Perfluoropentacene on Diindenoperylene, J. Phys. Chem. C, 115 (2011) 16155-16160.
[14] S. Difley, L.-P. Wang, S. Yeganeh, S.R. Yost, T.V. Voorhis, Electronic Properties of Disordered Organic Semiconductors via QM/MM Simulations, Acc. Chem. Res., 43 (2010) 995-1004.
[15] S. Verlaak, P. Heremans, Molecular microelectrostatic view on electronic states near pentacene grain boundaries, Phys. Rev. B, 75 (2007) 115127.
[16] S.M. Ryno, M.K. Ravva, X. Chen, H. Li, J.-L. Brédas, Molecular Understanding of Fullerene – Electron Donor Interactions in Organic Solar Cells, Adv. Electron. Mater., 7 (2017) 1601370.
[17] Y. Qian, X. Zhang, L. Xie, D. Qi, B.K. Chandran, X. Chen, W. Huang, Stretchable Organic Semiconductor Devices, Adv. Mater., 28 (2016) 9243-9265.
[18] O. Ostroverkhova, Organic Optoelectronic Materials: Mechanisms and Applications, Chem. Rev., 116 (2016) 13279-13412.

[19] M. Ajdari, T. Schmitt, M. Hoffmann, F. Maass, H. Reiss, U.H.F. Bunz, A. Dreuw, P. Tegeder, Electronic Properties of 6,13-Diazapentacene Adsorbed on Au(111): A Quantitative Determination of Transport, Singlet and Triplet States, and Electronic Spectra, J. Phys. Chem. C, 124 (2020) 13196-13205.
[20] P.T.P. Ryan, P.L. Lalaguna, F. Haag, M.M. Braim, P. Ding, D.J. Payne, J.V. Barth, T.L. Lee, D.P. Woodruff, F. Allegretti, D.A. Duncan, Validation of the Inverted Adsorption Structure for Free-base Tetraphenyl Porphyrin on Cu(111), Chem. Commun., 56 (2020) 3681-3684.
[21] C. Gu, J.L. Zhang, S. Sun, X. Lian, Z. Ma, H. Mao, L. Guo, Y. Wang, W. Chen, Molecular-Scale Investigation of the Thermal and Chemical Stability of Monolayer PTCDA on Cu(111) and Cu(110), ACS Appl. Mater. Interfaces, 12 (2020) 22327-22334.
[22] E. Zojer, T.C. Taucher, O.T. Hofmann, The Impact of Dipolar Layers on the Electronic Properties of Organic/Inorganic Hybrid Interfaces, Adv. Mater. Interfaces, 6 (2019) 1900581.
[23] M. Nam, M. Cha, H.H. Lee, K. Hur, K.-T. Lee, J. Yoo, I.K. Han, S.J. Kwon, D.-H. Ko, Long-term efficient organic photovoltaics based on quaternary bulk heterojunctions, Nat. Commun., 8 (2017) 14068.
[24] V. Belova, P. Beyer, E. Meister, T. Linderl, M.U. Halbich, M. Gerhard, S. Schmidt, T. Zechel, T. Meisel, A.V. Generalov, A.S. Anselmo, R. Scholz, O. Konovalov, A. Gerlach, M. Koch, A. Hinderhofer, A. Opitz, W. Brutting, F. Schreiber, Evidence for Anisotropic Electronic Coupling of Charge Transfer States in Weakly Interacting Organic Semiconductor Mixtures, J. Am. Chem. Soc., 139 (2017) 8474-8486.
[25] G. Duva, L. Pithan, C. Zeiser, B. Reisz, J. Dieterle, B. Hofferberth, P. Beyer, L. Bogula, A. Opitz, S. Kowarik, A. Hinderhofer, A. Gerlach, F. Schreiber, Thin-Film Texture and Optical Properties of Donor/Acceptor Complexes. Diindenoperylene/F6TCNNQ vs Alpha-Sexithiophene/F6TCNNQ, J. Phys. Chem. C, 122 (2018) 18705-18714.
[26] Q. Wang, A. Franco-Cañellas, P. Ji, C. Bürker, R.-B. Wang, K. Broch, P.K. Thakur, T.-L. Lee, H. Zhang, A. Gerlach, L. Chi, S. Duhm, F. Schreiber, Bilayer Formation vs Molecular Exchange in Organic Heterostructures: Strong Impact of Subtle Changes in Molecular Structure, J. Phys. Chem. C, 122 (2018) 9480-9490.
[27] B. Stadtmüller, M. Gruenewald, J. Peuker, R. Forker, T. Fritz, C. Kumpf, Molecular Exchange in a Heteromolecular PTCDA/CuPc Bilayer Film on Ag(111), J. Phys. Chem. C, 118 (2014) 28592-28602.
[28] G. D'Avino, S. Duhm, R.G. Della Valle, G. Heimel, M. Oehzelt, S. Kera, N. Ueno, D. Beljonne, I. Salzmann, Electrostatic Interactions Shape Molecular Organization and Electronic Structure of Organic Semiconductor Blends, Chem. Mater., 32 (2020) 1261-1271.
[29] S. Thussing, L. Fernandez, P. Jakob, Thermal Stability and Interlayer Exchange Processes in Heterolayers of TiOPc and PTCDA on Ag(111), J. Phys.: Condens. Matter, 31 (2019) 134002.
[30] S. Braun, W.R. Salaneck, M. Fahlman, Energy-Level Alignment at Organic/Metal and Organic/Organic Interfaces, Adv. Mater., 21 (2009) 1450-1472.
[31] E. Goiri, P. Borghetti, A. El-Sayed, J.E. Ortega, D.G. de Oteyza, Multi-Component Organic Layers on Metal Substrates, Adv. Mater., 28 (2016) 1340-1368.

[32] M. Schwarze, W. Tress, B. Beyer, F. Gao, R. Scholz, C. Poelking, K. Ortstein, A.A. Günther, D. Kasemann, D. Andrienko, K. Leo, Band Structure Engineering in Organic Semiconductors, Science, 352 (2016) 1446-1449.
[33] N. Arora, M.I. Dar, A. Hinderhofer, N. Pellet, F. Schreiber, S.M. Zakeeruddin, M. Grätzel, Perovskite solar cells with CuSCN hole extraction layers yield stabilized efficiencies greater than 20%, Science, 358 (2017) 768-771.
[34] E.D. Glowacki, M. Irimia-Vladu, M. Kaltenbrunner, J. Gsiorowski, M.S. White, U. Monkowius, G. Romanazzi, G.P. Suranna, P. Mastrorilli, T. Sekitani, S. Bauer, T. Someya, L. Torsi, N.S. Sariciftci, Hydrogen-bonded semiconducting pigments for air-stable field-effect transistors, Adv. Mater., 25 (2013) 1563-1569.
[35] Q. Xin, S. Duhm, F. Bussolotti, K. Akaike, Y. Kubozono, H. Aoki, T. Kosugi, S. Kera, N. Ueno, Accessing Surface Brillouin Zone and Band Structure of Picene Single Crystals, Phys. Rev. Lett., 108 (2012) 226401.
[36] H. Ishii, K. Seki, Energy level alignment at organic/metal interfaces studied by UV photoemission: breakdown of traditional assumption of a common vacuum level at the interface, IEEE Trans. Electron Devices, 44 (1997) 1295-1301.
[37] R. Otero, A.L. Vázquez de Parga, J.M. Gallego, Electronic, structural and chemical effects of charge-transfer at organic/inorganic interfaces, Surf. Sci. Rep., 72 (2017) 105-145.
[38] M. Oehzelt, K. Akaike, N. Koch, G. Heimel, Energy-level alignment at organic heterointerfaces, Sci. Adv., 1 (2015) e1501127.
[39] A. Franco-Cañellas, S. Duhm, A. Gerlach, F. Schreiber, Binding and Electronic Level Alignment of π-Conjugated Systems on Metals, Rep. Prog. Phys., 83 (2020) 066501.
[40] D. Cahen, A. Kahn, Electron Energetics at Surfaces and Interfaces: Concepts and Experiments, Adv. Mater., 15 (2003) 271-277.
[41] R.A. Baragiola, Principles and applications of ion-induced auger electron emission from solids, Radiation Effects, 61 (1982) 47-72.
[42] J. Braun, The theory of angle-resolved ultraviolet photoemission and its applications to ordered materials, Rep. Prog. Phys., 59 (1996) 1267-1338.
[43] M.T. Greiner, M.G. Helander, W.-M. Tang, Z.-B. Wang, J. Qiu, Z.-H. Lu, Universal energy-level alignment of molecules on metal oxides, Nat. Mater., 11 (2011) 76.
[44] P.A. Damiano, J.R. Johnson, Mirror force induced wave dispersion in Alfvén waves, Phys. Plasmas, 20 (2013) 062901.
[45] J.-P. Yang, F. Bussolotti, S. Kera, N. Ueno, Origin and role of gap states in organic semiconductor studied by UPS: as the nature of organic molecular crystals, J. Phys. D: Appl. Phys., 50 (2017) 423002.
[46] H. Ishii, K. Sugiyama, E. Ito, K. Seki, Energy Level Alignment and Interfacial Electronic Structures at Organic/Metal and Organic/Organic Interfaces, Adv. Mater., 11 (1999) 605-625.
[47] K. Hong, J.W. Lee, S.Y. Yang, K. Shin, H. Jeon, S.H. Kim, C. Yang, C.E. Park, Lower hole-injection barrier between pentacene and a 1-hexadecanethiol-modified gold substrate with a lowered work function, Org. Electron., 9 (2008) 21-29.
[48] G. Horowitz, The organic transistor: state-of-the-art and outlook, Eur. Phys. J. Appl. Phys., 53 (2011) 33602.

[49] I.M. Vitomirov, A. Raisanen, L.J. Brillson, C.L. Lin, D.T. McInturff, P.D. Kirchner, J.M. Woodall, Temperature-dependent composition, ordering, and band bending at GaP(100) surfaces, J. Vac. Sci. Technol. A, 11 (1993) 841-847.
[50] F. Schreiber, Structure and growth of self-assembling monolayers, Prog. Surf. Sci., 65 (2000) 151-257.
[51] F. Schreiber, Organic Molecular Beam Deposition: Growth Studies Beyond the First Monolayer, Phys. Stat. Sol. (a), 201 (2004) 1037-1054.
[52] H. Ishii, K. Kudo, T. Nakayama, N. Ueno, Electronic Processes in Organic Electronics : Bridging Nanostructure, Electronic States and Device Properties, Springer Verlag, Japan, Tokyo, Japan, 2015.
[53] K. Seki, H. Yanagi, Y. Kobayashi, T. Ohta, T. Tani, UV photoemission study of dye/AgBr interfaces in relation to spectral sensitization, Phys. Rev. B, 49 (1994) 2760-2767.
[54] G. Gensterblum, K. Hevesi, B.Y. Han, L.M. Yu, J.J. Pireaux, P.A. Thiry, R. Caudano, A.A. Lucas, D. Bernaerts, S. Amelinckx, G. Van Tendeloo, G. Bendele, T. Buslaps, R.L. Johnson, M. Foss, R. Feidenhans'l, G. Le Lay, Growth mode and electronic structure of the epitaxial C60(111)/GeS(001) interface, Phys. Rev. B, 50 (1994) 11981-11995.
[55] A. Franco-Cañellas, Q. Wang, K. Broch, D.A. Duncan, P.K. Thakur, L. Liu, S. Kera, A. Gerlach, S. Duhm, F. Schreiber, Metal-Organic Interface Functionalization via Acceptor End Groups: PTCDI on Coinage Metals, Phys. Rev. Mater., 1 (2017) 013001.
[56] N. Aghdassi, Q. Wang, R.R. Ji, B. Wang, J. Fan, S. Duhm, Ultraviolet Photoelectron Spectroscopy Reveals Energy-Band Dispersion for Pi-stacked 7,8,15,16-tetraazaterrylene Thin Films in a Donor-Acceptor Bulk Heterojunction, Nanotechnology, 29 (2018) 194002.
[57] M. Samadi Khoshkhoo, H. Peisert, T. Chassé, M. Scheele, The role of the density of interface states in interfacial energy level alignment of PTCDA, Org. Electron., 49 (2017) 249-254.
[58] M. Oehzelt, N. Koch, G. Heimel, Organic semiconductor density of states controls the energy level alignment at electrode interfaces, Nat. Commun., 5 (2014) 4174.
[59] R.A. Street, Electronic Structure and Properties of Organic Bulk-Heterojunction Interfaces, Adv. Mater., 28 (2016) 3814-3830.
[60] J. Yang, D. Yan, T.S. Jones, Molecular Template Growth and Its Applications in Organic Electronics and Optoelectronics, Chem. Rev., 115 (2015) 5570-5603.
[61] X. Zhang, Z. Shao, X. Zhang, Y. He, J. Jie, Surface Charge Transfer Doping of Low-Dimensional Nanostructures toward High-Performance Nanodevices, Adv. Mater., 28 (2016) 10409-10442.
[62] K. Akaike, M.V. Nardi, M. Oehzelt, J. Frisch, A. Opitz, C. Christodoulou, G. Ligorio, P. Beyer, M. Timpel, I. Pis, F. Bondino, K. Moudgil, S. Barlow, S.R. Marder, N. Koch, Effective Work Function Reduction of Practical Electrodes Using an Organometallic Dimer, Adv. Funct. Mater., 26 (2016) 2493-2502.
[63] P. Amsalem, A. Wilke, J. Frisch, J. Niederhausen, A. Vollmer, R. Rieger, K. Müllen, J.P. Rabe, N. Koch, Interlayer molecular diffusion and thermodynamic equilibrium in organic heterostructures on a metal electrode, J. Appl. Phys., 110 (2011) 113709.
[64] L. Zhang, F.-S. Zu, Y.-L. Deng, F. Igbari, Z.-K. Wang, L.-S. Liao, Origin of Enhanced Hole Injection in Organic Light-Emitting Diodes with an Electron-Acceptor Doping Layer: p-Type Doping or Interfacial Diffusion?, ACS Appl. Mater. Interfaces, 7 (2015) 11965-11971.

[65] J. Li, C.W. Rochester, I.E. Jacobs, S. Friedrich, P. Stroeve, M. Riede, A.J. Moulé, Measurement of Small Molecular Dopant F4TCNQ and C60F36 Diffusion in Organic Bilayer Architectures, ACS Appl. Mater. Interfaces, 7 (2015) 28420-28428.
[66] S. Duhm, I. Salzmann, B. Bröker, H. Glowatzki, R.L. Johnson, N. Koch, Interdiffusion of molecular acceptors through organic layers to metal substrates mimics doping-related energy level shifts, Appl. Phys. Lett., 95 (2009) 093305.
[67] L. Sun, C. Liu, D. Queteschiner, G. Weidlinger, P. Zeppenfeld, Layer inversion in organic heterostructures, Phys. Chem. Chem. Phys., 13 (2011) 13382-13386.
[68] J.M. Gallego, D. Ecija, N. Martín, R. Otero, R. Miranda, An STM study of molecular exchange processes in organic thin film growth, Chem. Commun., 50 (2014) 9954-9957.
[69] B. Stadtmüller, T. Sueyoshi, G. Kichin, I. Kröger, S. Soubatch, R. Temirov, F.S. Tautz, C. Kumpf, Commensurate Registry and Chemisorption at a Hetero-organic Interface, Phys. Rev. Lett., 108 (2012) 106103.
[70] F. Sellam, T. Schmitz-Hübsch, M. Toerker, S. Mannsfeld, H. Proehl, T. Fritz, K. Leo, C. Simpson, K. Müllen, LEED and STM investigations of organic–organic heterostructures grown by molecular beam epitaxy, Surf. Sci., 478 (2001) 113-121.
[71] M. Gruenewald, C. Sauer, J. Peuker, M. Meissner, F. Sojka, A. Schöll, F. Reinert, R. Forker, T. Fritz, Commensurism at electronically weakly interacting phthalocyanine/PTCDA heterointerfaces, Phys. Rev. B, 91 (2015) 155432.
[72] B. Stadtmüller, M. Willenbockel, S. Schröder, C. Kleimann, E.M. Reinisch, T. Ules, S. Soubatch, M.G. Ramsey, F.S. Tautz, C. Kumpf, Modification of the PTCDA-Ag Bond by Forming a Heteromolecular Bilayer Film, Phys. Rev. B, 91 (2015) 155433.
[73] C. Kleimann, B. Stadtmüller, S. Schröder, C. Kumpf, Electrostatic Interaction and Commensurate Registry at the Heteromolecular F16CuPc–CuPc Interface, J. Phys. Chem. C, 118 (2014) 1652-1660.
[74] P. Borghetti, D.G. de Oteyza, C. Rogero, E. Goiri, A. Verdini, A. Cossaro, L. Floreano, J.E. Ortega, Molecular-Level Realignment in Donor–Acceptor Bilayer Blends on Metals, J. Phys. Chem. C, 120 (2016) 5997-6005.
[75] X. Bouju, C. Mattioli, G. Franc, A. Pujol, A. Gourdon, Bicomponent Supramolecular Architectures at the Vacuum–Solid Interface, Chem. Rev., 117 (2017) 1407-1444.
[76] A. El-Sayed, P. Borghetti, E. Goiri, C. Rogero, L. Floreano, G. Lovat, D.J. Mowbray, J.L. Cabellos, Y. Wakayama, A. Rubio, J.E. Ortega, D.G. de Oteyza, Understanding Energy-Level Alignment in Donor-Acceptor/Metal Interfaces from Core-Level Shifts, ACS Nano, 8 (2013) 6914-6920.
[77] Y. Wakayama, On-surface molecular nanoarchitectonics: From self-assembly to directed assembly, Jpn. J. Appl. Phys., 55 (2016) 1102AA.
[78] C. Henneke, J. Felter, D. Schwarz, F.S. Tautz, C. Kumpf, Controlling the Growth of Multiple Ordered Heteromolecular Phases by Utilizing Intermolecular Repulsion, Nat. Mater., 16 (2017) 628-633.
[79] S. Thussing, P. Jakob, Thermal Stability and Interlayer Exchange Processes in Heterolayers of CuPc and PTCDA on Ag(111), J. Phys. Chem. C, 121 (2017) 13680-13691.
[80] D.A. Egger, V.G. Ruiz, W.A. Saidi, T. Bučko, A. Tkatchenko, E. Zojer, Understanding Structure and Bonding of Multilayered Metal–Organic Nanostructures, J. Phys. Chem. C, 117 (2013) 3055-3061.

[81] L. Fernández, S. Thussing, A. Mänz, G. Witte, A.X. Brion-Rios, P. Cabrera-Sanfelix, D. Sanchez-Portal, P. Jakob, Structural and Vibrational Properties of the TiOPc Monolayer on Ag(111), J. Phys. Chem. C, 121 (2017) 1608-1617.
[82] I. Kröger, B. Stadtmüller, C. Kumpf, Submonolayer and multilayer growth of titaniumoxide-phthalocyanine on Ag(111), New J. Phys., 18 (2016) 113022.
[83] L. Kilian, A. Hauschild, R. Temirov, S. Soubatch, A. Schöll, A. Bendounan, F. Reinert, T.L. Lee, F.S. Tautz, M. Sokolowski, E. Umbach, Role of Intermolecular Interactions on the Electronic and Geometric Structure of a Large π-Conjugated Molecule Adsorbed on a Metal Surface, Phys. Rev. Lett., 100 (2008) 136103.
[84] S. Duhm, A. Gerlach, I. Salzmann, B. Bröker, R.L. Johnson, F. Schreiber, N. Koch, PTCDA on Au(111), Ag(111) and Cu(111): Correlation of Interface Charge Transfer to Bonding Distance, Org. Electron., 9 (2008) 111-118.
[85] Y. Zou, L. Kilian, A. Schöll, T. Schmidt, R. Fink, E. Umbach, Chemical bonding of PTCDA on Ag surfaces and the formation of interface states, Surf. Sci., 600 (2006) 1240-1251.
[86] W. Liu, S.N. Filimonov, J. Carrasco, A. Tkatchenko, Molecular switches from benzene derivatives adsorbed on metal surfaces, Nat. Commun., 4 (2013) 2569.
[87] S. Jakobs, A. Narayan, B. Stadtmüller, A. Droghetti, I. Rungger, Y.S. Hor, S. Klyatskaya, D. Jungkenn, J. Stöckl, M. Laux, O.L.A. Monti, M. Aeschlimann, R.J. Cava, M. Ruben, S. Mathias, S. Sanvito, M. Cinchetti, Controlling the Spin Texture of Topological Insulators by Rational Design of Organic Molecules, Nano Lett., 15 (2015) 6022-6029.
[88] R.J. Maurer, V.G. Ruiz, J. Camarillo-Cisneros, W. Liu, N. Ferri, K. Reuter, A. Tkatchenko, Adsorption structures and energetics of molecules on metal surfaces: Bridging experiment and theory, Prog. Surf. Sci., 91 (2016) 72-100.
[89] M. Hollerer, D. Luftner, P. Hurdax, T. Ules, S. Soubatch, F.S. Tautz, G. Koller, P. Puschnig, M. Sterrer, M.G. Ramsey, Charge Transfer and Orbital Level Alignment at Inorganic/Organic Interfaces: The Role of Dielectric Interlayers, ACS Nano, 11 (2017) 6252-6260.
[90] V. Obersteiner, M. Scherbela, L. Hörmann, D. Wegner, O.T. Hofmann, Structure Prediction for Surface-Induced Phases of Organic Monolayers: Overcoming the Combinatorial Bottleneck, Nano Lett., 17 (2017) 4453-4460.
[91] D.P. Woodruff, Surface Structure Determination Using X-ray Standing Waves, Rep. Prog. Phys., 68 (2005) 743-798.
[92] J. Zegenhagen, Surface Structure Analysis with X-Ray Standing Waves, in: G. Bracco, B. Holst (Eds.) The X-Ray Standing Wave Technique, Springer Berlin Heidelberg, Springer Series in Surface Science, 2013, pp. 249-275.
[93] G. Zamborlini, D. Lüftner, Z. Feng, B. Kollmann, P. Puschnig, C. Dri, M. Panighel, G. Di Santo, A. Goldoni, G. Comelli, M. Jugovac, V. Feyer, C.M. Schneider, Multi-orbital charge transfer at highly oriented organic/metal interfaces, Nat. Commun., 8 (2017) 335.
[94] O.T. Hofmann, H. Glowatzki, C. Bürker, G.M. Rangger, B. Bröker, J. Niederhausen, T. Hosokai, I. Salzmann, R.P. Blum, R. Rieger, A. Vollmer, P. Rajput, A. Gerlach, K. Müllen, F. Schreiber, E. Zojer, N. Koch, S. Duhm, Orientation-Dependent Work-Function Modification Using Substituted Pyrene-Based Acceptors, J. Phys. Chem. C, 121 (2017) 24657-24668.
[95] L. Jiang, A.C. Papageorgiou, S.C. Oh, Ö. Sağlam, J. Reichert, D.A. Duncan, Y.-Q. Zhang, F. Klappenberger, Y. Guo, F. Allegretti, S. More, R. Bhosale, A. Mateo-Alonso, J.V. Barth,

Synthesis of Pyrene-Fused Pyrazaacenes on Metal Surfaces: Toward One-Dimensional Conjugated Nanostructures, ACS Nano, 10 (2016) 1033-1041.
[96] A. Ugolotti, S.S. Harivyasi, A. Baby, M. Dominguez, A.L. Pinardi, M.F. López, J.Á. Martín-Gago, G. Fratesi, L. Floreano, G.P. Brivio, Chemisorption of Pentacene on Pt(111) with a Little Molecular Distortion, J. Phys. Chem. C, 121 (2017) 22797-22805.
[97] G. Heimel, S. Duhm, I. Salzmann, A. Gerlach, A. Strozecka, J. Niederhausen, C. Burker, T. Hosokai, I. Fernandez-Torrente, G. Schulze, S. Winkler, A. Wilke, R. Schlesinger, J. Frisch, B. Broker, A. Vollmer, B. Detlefs, J. Pflaum, S. Kera, K.J. Franke, N. Ueno, J.I. Pascual, F. Schreiber, N. Koch, Charged and Metallic Molecular Monolayers Through Surface-Induced Aromatic Stabilization, Nat. Chem., 5 (2013) 187-194.
[98] M. Häming, M. Greif, C. Sauer, A. Schöll, F. Reinert, Electronic structure of ultrathin heteromolecular organic-metal interfaces: SnPc/PTCDA/Ag(111) and SnPc/Ag(111), Phys. Rev. B, 82 (2010) 235432.
[99] N. Ferri, A. Ambrosetti, A. Tkatchenko, Electronic Charge Rearrangement at Metal/Organic Interfaces Induced by Weak van der Waals Interactions, Phys. Rev. Mater., 1 (2017) 026003.
[100] I. Kröger, B. Stadtmüller, C. Stadler, J. Ziroff, M. Kochler, A. Stahl, F. Pollinger, T.-L. Lee, J. Zegenhagen, F. Reinert, C. Kumpf, Submonolayer growth of copper-phthalocyanine on Ag(111), New J. Phys., 12 (2010) 083038.
[101] L. Romaner, G. Heimel, J.-L. Brédas, A. Gerlach, F. Schreiber, R.L. Johnson, J. Zegenhagen, S. Duhm, N. Koch, E. Zojer, Impact of Bidirectional Charge Transfer and Molecular Distortions on the Electronic Structure of a Metal-Organic Interface, Phys. Rev. Lett., 99 (2007) 256801.
[102] Q. Wang, A. Franco-Cañellas, J. Yang, J. Hausch, S. Struzek, M. Chen, P.K. Thakur, A. Gerlach, S. Duhm, F. Schreiber, Heteromolecular Bilayers on a Weakly Interacting Substrate: Physisorptive Bonding and Molecular Distortions of Copper-Hexadecafluorophthalocyanine, ACS Appl. Mater. Interfaces, 12 (2020) 14542-14551.
[103] Y. Liu, D. Ikeda, S. Nagamatsu, T. Nishi, N. Ueno, S. Kera, Impact of molecular orbital distribution on photoelectron intensity for picene film, J. Electron Spectrosc. Relat. Phenom., 195 (2014) 287-292.
[104] C. Bürker, A. Franco-Cañellas, K. Broch, T.L. Lee, A. Gerlach, F. Schreiber, Self-Metalation of 2H-Tetraphenylporphyrin on Cu(111) Studied with XSW: Influence of the Central Metal Atom on the Adsorption Distance, J. Phys. Chem. C, 118 (2014) 13659-13666.
[105] P. Puschnig, S. Berkebile, A.J. Fleming, G. Koller, K. Emtsev, T. Seyller, J.D. Riley, C. Ambrosch-Draxl, F.P. Netzer, M.G. Ramsey, Reconstruction of Molecular Orbital Densities from Photoemission Data, Science, 326 (2009) 702.
[106] H. Peisert, J. Uihlein, F. Petraki, T. Chassé, Charge transfer between transition metal phthalocyanines and metal substrates: The role of the transition metal, J. Electron Spectrosc. Relat. Phenom., 204 (2015) 49-60.
[107] M. Willenbockel, D. Lüftner, B. Stadtmüller, G. Koller, C. Kumpf, S. Soubatch, P. Puschnig, M.G. Ramsey, F.S. Tautz, The interplay between interface structure, energy level alignment and chemical bonding strength at organic–metal interfaces, Phys. Chem. Chem. Phys., 17 (2015) 1530-1548.

[108] S. Sharifzadeh, A. Biller, L. Kronik, J.B. Neaton, Quasiparticle and optical spectroscopy of the organic semiconductors pentacene and PTCDA from first principles, Phys. Rev. B, 85 (2012) 125307.
[109] A. Hinderhofer, U. Heinemeyer, A. Gerlach, S. Kowarik, R.M. Jacobs, Y. Sakamoto, T. Suzuki, F. Schreiber, Optical Properties of Pentacene and Perfluoropentacene Thin Films, J. Chem. Phys., 127 (2007) 194705.
[110] Y. Sakamoto, T. Suzuki, M. Kobayashi, Y. Gao, Y. Fukai, Y. Inoue, F. Sato, S. Tokito, Perfluoropentacene: High-Performance p-n Junctions and Complementary Circuits with Pentacene, J. Am. Chem. Soc., 126 (2004) 8130-8140.
[111] I. Salzmann, R. Opitz, S. Rogaschewski, J.P. Rabe, N. Koch, B. Nickel, Phase separation in vacuum codeposited pentacene/6,13-pentacenequinone thin films, Phys. Rev. B, 75 (2007) 174108.
[112] K.H. Lee, H.S. Lee, K. Lee, T. Ha, J.H. Kim, S. Im, An Almost Transparent Image Pixel with a Pentacene/ZnO Photodiode, a Pentacene Thin-Film Transistor, and a 6,13-Pentacenequinone Phosphor Layer, Adv. Mater., 23 (2011) 1231-1236.
[113] D.R.T. Zahn, G.N. Gavrila, M. Gorgoi, The transport gap of organic semiconductors studied using the combination of direct and inverse photoemission, Chem. Phys., 325 (2006) 99-112.
[114] C. Shen, A. Kahna, Electronic structure, diffusion, and p-doping at the Au/F16CuPc interface, J. Appl. Phys., 90 (2001).
[115] R. Murdey, N. Sato, M. Bouvet, Frontier Electronic Structures in Fluorinated Copper Phthalocyanine Thin Films Studied Using Ultraviolet and Inverse Photoemission Spectroscopies, Molecular Crystals and Liquid Crystals, 455 (2006) 211-218.
[116] D. Placencia, W. Wang, R.C. Shallcross, K.W. Nebesny, M. Brumbach, N.R. Armstrong, Organic Photovoltaic Cells Based On Solvent-Annealed, Textured Titanyl Phthalocyanine/C60 Heterojunctions, Adv. Funct. Mater., 19 (2009) 1913-1921.
[117] H. Yanagi, S. Chen, P.A. Lee, K.W. Nebesny, N.R. Armstrong, A. Fujishima, Dye-Sensitizing Effect of TiOPc Thin Film on n-TiO2 (001) Surface, J. Phys. Chem., 100 (1996) 5447-5451.
[118] S. Kera, T. Hosokai, S. Duhm, Characteristics of Organic–Metal Interaction: A Perspective from Bonding Distance to Orbital Delocalization, J. Phys. Soc. Jpn., 87 (2018) 061008.
[119] C. Bürker, N. Ferri, A. Tkatchenko, A. Gerlach, J. Niederhausen, T. Hosokai, S. Duhm, J. Zegenhagen, N. Koch, F. Schreiber, Exploring the bonding of large hydrocarbons on noble metals: Diindoperylene on Cu(111), Ag(111), and Au(111), Phys. Rev. B, 87 (2013) 165443.
[120] Q. Wang, Q. Xin, R.-B. Wang, M. Oehzelt, N. Ueno, S. Kera, S. Duhm, Picene thin films on metal surfaces: Impact of molecular shape on interfacial coupling, Phys. Status Solidi RRL, 11 (2017) 1700012.
[121] C.D. Sheraw, T.N. Jackson, D.L. Eaton, J.E. Anthony, Functionalized Pentacene Active Layer Organic Thin-Film Transistors, Adv. Mater., 15 (2003) 2009-2011.
[122] C.D. Sheraw, L. Zhou, J.R. Huang, D.J. Gundlach, T.N. Jackson, M.G. Kane, I.G. Hill, M.S. Hammond, J. Campi, B.K. Greening, J. Francl, J. West, Organic thin-film transistor-driven polymer-dispersed liquid crystal displays on flexible polymeric substrates, Appl. Phys. Lett., 80 (2002) 1088-1090.

[123] J.B. Goodenough, Spin-Orbit-Coupling Effects in Transition-Metal Compounds, Phys. Rev., 171 (1968) 466-479.
[124] R.J. Radwanski, R. Michalski, Z. Ropka, A. Blaut, Crystal-field interactions and magnetism in rare-earth transition-metal intermetallic compounds, Phys B: Condens. Matter, 319 (2002) 78-89.
[125] J.T. Tates, Experimental Innovations in Surface Science, Second Edition ed., Springer, Cham 2015.
[126] A. Chambers, Modern Vacuum Physics, CRC Press2005.
[127] H.E. Farnsworth, R.E. Schlier, T.H. George, R.M. Burger, Ion Bombardment-Cleaning of Germanium and Titanium as Determined by Low-Energy Electron Diffraction, J. App. Phys., 26 (1955) 252-253.
[128] K. Vedam, Characterization of Defects in Real Surfaces by Ellipsometry, Surf. Sci., 56 (1976) 221-236.
[129] A. Schöll, F. Schreiber, Chapter 24 - Thin Films of Organic Molecules: Interfaces and Epitaxial Growth, Elsevier2018, pp. 551-570.
[130] A.S. Yuwono, P.S. Lammers, Odor pollution in the environment and the detection instrumentation, Agric. Eng., Int. CIGR J., 6 (2004).
[131] J.A. Greer, M.D. Tabat, C. Lu, Future trends for large-area pulsed laser deposition, Nucl. Instrum. Methods Phys. Res. B, 121 (1997) 357-362.
[132] M.A. Leitch-Devlin, D.A. Williams, Sticking coefficients for atoms and molecules at the surfaces of interstellar dust grains, Mon. Not. R. Astron. Soc., 213 (1985) 295-306.
[133] F. Herrán, C. Le Guet, A. Favre, F. Gaillard, Validation, improvement and implementation of sorption mathematical models using a quartz crystal microbalance (QCM), Microelectron. Eng., 149 (2016) 106-112.
[134] S. Suga, A. Sekiyama, Photoelectron Spectroscopy: Bulk and Surface Electronic Structures, Heidelberg, Springer, Berlin, 2014.
[135] H.F. Dylla, Development of ultrahigh and extreme high vacuum technology for physics research, J. Vac. Sci. Technol. A, 21 (2003) S25-S33.
[136] A.Z. Moshfegh, Vacuum Technology: Principles and Applications, Physics and Technology of Thin Films, World Scientific2004, pp. 11-27.
[137] F. Reinert, S. Hüfner, Photoemission spectroscopy—from early days to recent applications, New J. Phys., 7 (2005) 97-97.
[138] A. Damascelli, Z. Hussain, Z.-X. Shen, Angle-resolved photoemission studies of the cuprate superconductors, Rev. Mod. Phys., 75 (2003) 473-541.
[139] D.P. Woodruff, T.A. Delchar, Modern techniques of surface science, Cambridge Univ. Press, New York, NY (United States), United States, 1994.
[140] H. Offenbacher, D. Lüftner, T. Ules, E.M. Reinisch, G. Koller, P. Puschnig, M.G. Ramsey, Orbital tomography: Molecular band maps, momentum maps and the imaging of real space orbitals of adsorbed molecules, J. Electron. Spectrosc. Relat. Phenom., 204 (2015) 92-101.
[141] F.J. Himpsel, Angle-resolved measurements of the photoemission of electrons in the study of solids, Adv. Phys., 32 (1983) 1-51.
[142] Y. Nakayama, S. Kera, N. Ueno, Photoelectron spectroscopy on single crystals of organic semiconductors: experimental electronic band structure for optoelectronic properties, J. Mater. Chem. C, 8 (2020) 9090-9132.

[143] S. Hüfner, Photoelectron Spectroscopy: Principles and Applications, Third edition ed., New York: Springer, Berlin, 2003.
[144] H. Hertz, Ueber einen Einfluss des ultravioletten Lichtes auf die electrische Entladung, Ann. Phys., 267 (1887) 983-1000.
[145] A. Einstein, Über einen die Erzeugung und Verwandlung des Lichtes betreffenden heuristischen Gesichtspunkt, Ann. Phys., 322 (1905) 132-148.
[146] B. Lv, T. Qian, H. Ding, Angle-resolved photoemission spectroscopy and its application to topological materials, Nat. Rev. Phys., 1 (2019) 609-626.
[147] S. Kera, H. Yamane, N. Ueno, First-Principles Measurements of Charge Mobility in Organic Semiconductors: Valence Hole–Vibration Coupling in Organic Ultrathin Films, Prog. Surf. Sci., 84 (2009) 135-154.
[148] Q. Wang, J. Yang, A. Franco-Cañellas, C. Bürker, J. Niederhausen, P. Dombrowski, F. Widdascheck, T. Breuer, G. Witte, A. Gerlach, S. Duhm, F. Schreiber, Pentacene/Perfluoropentacene Bilayers on Au(111) and Cu(111): Impact of Organic-Metal Coupling Strength on Molecular Structure Formation, (2020) Submitted.
[149] R.-R. Ji, Q. Wang, J.-X. Hu, S. Duhm, Impact of Room Temperature on Pentacene Thin Film Growth and Electronic Structure, Can. J. Chem., 95 (2017) 1130-1134.
[150] N. Koch, A. Vollmer, S. Duhm, Y. Sakamoto, T. Suzuki, The Effect of Fluorination on Pentacene/Gold Interface Energetics and Charge Reorganization Energy, Adv. Mater., 19 (2007) 112-116.
[151] C.S. Fadley, Angle-resolved x-ray photoelectron spectroscopy, Prog. Surf. Sci., 16 (1984) 275-388.
[152] C. Papp, H.-P. Steinrück, In situ high-resolution X-ray photoelectron spectroscopy – Fundamental insights in surface reactions, Surf. Sci. Rep., 68 (2013) 446-487.
[153] H. Sezen, S. Suzer, XPS for chemical- and charge-sensitive analyses, Thin Solid Films, 534 (2013) 1-11.
[154] P.S. Bagus, E.S. Ilton, C.J. Nelin, The interpretation of XPS spectra: Insights into materials properties, Surf. Sci. Rep., 68 (2013) 273-304.
[155] J. Cazaux, Secondary electron emission and fundamentals of charging mechanisms in XPS, J. Electron. Spectrosc. Relat. Phenom., 178-179 (2010) 357-372.
[156] S. Svensson, B. Eriksson, N. Mårtensson, G. Wendin, U. Gelius, Electron shake-up and correlation satellites and continuum shake-off distributions in X-Ray photoelectron spectra of the rare gas atoms, J. Electron Spectrosc. Relat. Phenom., 47 (1988) 327-384.
[157] J.F. Moulder, W.F. Stickle, P.E. Sobol, K.D. Bomben, Handbook of X-Ray Photoelectron Spectroscopy: A Reference Book of Standard Spectra for Identification and Interpretation of XPS Data, Physical Electronics Division, Perkin-Elmer Corporation1992.
[158] O. Travnikova, K.J. Børve, M. Patanen, J. Söderström, C. Miron, L.J. Sæthre, N. Mårtensson, S. Svensson, The ESCA molecule—Historical remarks and new results, J. Electron Spectrosc. Relat. Phenom., 185 (2012) 191-197.
[159] T.I.T. Okpalugo, P. Papakonstantinou, H. Murphy, J. McLaughlin, N.M.D. Brown, High resolution XPS characterization of chemical functionalised MWCNTs and SWCNTs, Carbon, 43 (2005) 153-161.
[160] D. Briggs, G. Beamson, XPS studies of the oxygen 1s and 2s levels in a wide range of functional polymers, Anal. Chem., 65 (1993) 1517-1523.

[161] S. Hüfner, S. Schmidt, F. Reinert, Photoelectron spectroscopy—An overview, Nucl. Instrum. Meth. A, 547 (2005) 8-23.
[162] Casa Software Ltd, CasaXPS: Processing Software for XPS, AES, SIMS and More, http://www.casaxps.com/, 2018.
[163] D.A. Shirley, High-Resolution X-Ray Photoemission Spectrum of the Valence Bands of Gold, Phy. Rev. B, 5 (1972) 4709-4714.
[164] J. Végh, The Shirley background revised, J. Electron Spectrosc. Relat. Phenom., 151 (2006) 159-164.
[165] A. Proctor, Data Analysis Techniques in X-ray Photoelectron Spectroscopy, Anal. Chem., 54 (1982) 13-19.
[166] P. Borghetti, A. El-Sayed, E. Goiri, C. Rogero, J. Lobo-Checa, L. Floreano, J. Enrique Ortega, D. G. de Oteyza, Spectroscopic Fingerprints of Work-Function-Controlled Phthalocyanine Charging on Metal Surfaces, ACS Nano, 8 (2014).
[167] H. Peisert, M. Knupfer, T. Schwieger, G.G. Fuentes, D. Olligs, J. Fink, T. Schmidt, Fluorination of copper phthalocyanines: Electronic structure and interface properties, J. Appl. Phys., 93 (2003) 9683-9692.
[168] S. Sinha, A.K.M.M. Islam, M. Vorokhta, M. Mukherjee, Interaction at the F16CuPc/TiO2 Interface: A Photoemission and X-ray Absorption Study, J. Phys. Chem. C, 121 (2017) 3365-3372.
[169] Y. Taki, O. Takai, XPS structural characterization of hydrogenated amorphous carbon thin films prepared by shielded arc ion plating, Thin Solid Films, 316 (1998) 45-50.
[170] N.H. Turner, A.M. Single, Determination of peak positions and areas from wide-scan XPS spectra, Surf. Interface Anal., 15 (1990) 215-222.
[171] J. Zegenhagen, Surface Structure Determination with X-ray Standing Waves, Surf. Sci. Rep., 18 (1993) 202-271.
[172] J. Zegenhagen, X-ray Standing Waves Technique: Fourier Imaging Active Sites, Jpn. J. Appl. Phys., 58 (2019) 110502.
[173] M.J. Bedzyk, X-Ray Standing Wave Techniques, Encyclopedia of Condensed Matter Physics, Elsevier Inc2005, pp. 330-341.
[174] B.W. Batterman, H. Cole, Dynamical Diffraction of X Rays by Perfect Crystals, Rev. Mod. Phys., 36 (1964) 681-717.
[175] A. Authier, Dynamical Theory of X-Ray Diffraction, Oxford University Press, Oxford, 2003.
[176] A. Gerlach, C. Bürker, T. Hosokai, F. Schreiber, X-Ray Standing Waves and Surfaces X-Ray Scattering Studies of Molecule–Metal Interfaces, in: N. Koch, N. Ueno, A.T.S. Wee (Eds.) The Molecule–Metal Interface, Wiley-VCH, Weinheim, Germany, 2013, pp. 153-172.
[177] A. Franco-Cañellas, Impact of partial nitrogen and fluorine substitution on the interface properties of pi-conjugated molecules adsorbed on inorganic substrates, Eberhard Karls Universität Tübingen, 2018.
[178] M.A. Hove, W.H. Weinberg, C.-M. Chan, Low-energy electron diffraction: experiment, theory and surface structure determination, Springer, Berlin, 1986.
[179] H. Lüth, Solid Surfaces, Interfaces and Thin Films, Springer, Berlin, 2010.
[180] G. Held, Low-energy electron diffraction: crystallography of surfaces and interfaces in: R. Schafer, P. C. Schmidt (Eds.), Wiley-VCH2012, pp. 631-649.

[181] R.V. Mom, C. Hahn, L. Jacobse, L.B.F. Juurlink, LEED analysis of a nickel cylindrical single crystal, Surf. Sci., 613 (2013) 15-20.
[182] N. Memmel, Monitoring and Modifying Properties of Metal Surfaces by Electronic Surface States, Surf. Sci. Rep., 32 (1998) 91-163.
[183] K.E. Hermann, M.A. Van Hove, LEEDpat, http://www.fhi-berlin.mpg.de/KHsoftware/LEEDpat/, 2014.
[184] N.V. Skorodumova, S.I. Simak, Spatial configurations of monoatomic gold chains, Comput. Mater. Sci., 17 (2000) 178-181.
[185] Diamond Light Source, Beamline Layout, https://www.diamond.ac.uk/Instruments/Structures-and-Surfaces/I09/Beamline-layout.html, 2020.
[186] K. Akaike, A. Onishi, Y. Wakayama, K. Kanai, Structural Disordering upon Formation of Molecular Heterointerfaces, J. Phys. Chem. C, 123 (2019) 12242-12248.
[187] K. Akaike, N. Koch, G. Heimel, M. Oehzelt, The Impact of Disorder on the Energy Level Alignment at Molecular Donor-Acceptor Interfaces, Adv. Mater. Interfaces, 2 (2015) 1-6.
[188] E. Goiri, M. Matena, A. El-Sayed, J. Lobo-Checa, P. Borghetti, C. Rogero, B. Detlefs, J. Duvernay, J.E. Ortega, D.G. de Oteyza, Self-Assembly of Bicomponent Molecular Monolayers: Adsorption Height Changes and Their Consequences, Phys. Rev. Lett., 112 (2014) 117602.
[189] N. Ueno, S. Kera, Electron spectroscopy of functional organic thin films: Deep insights into valence electronic structure in relation to charge transport property, Prog. Surf. Sci., 83 (2008) 490-557.
[190] X.-Q. Shi, Y. Li, M.A. Van Hove, R.-Q. Zhang, Interactions between Organics and Metal Surfaces in the Intermediate Regime between Physisorption and Chemisorption, J. Phys. Chem. C, 116 (2012) 23603-23607.
[191] M.G. Betti, A. Kanjilal, C. Mariani, H. Vázquez, Y.J. Dappe, J. Ortega, F. Flores, Barrier Formation at Organic Interfaces in a Cu(100)-benzenethiolate-pentacene Heterostructure, Phys. Rev. Lett., 100 (2008) 027601.
[192] A.K. Geim, I.V. Grigorieva, Van der Waals Heterostructures, Nature, 499 (2013) 419-425.
[193] A. Hinderhofer, C. Frank, T. Hosokai, A. Resta, A. Gerlach, F. Schreiber, Structure and Morphology of Coevaporated Pentacene-Perfluoropentacene Thin Films, J. Chem. Phys., 134 (2011) 104702.
[194] S. Duhm, G. Heimel, I. Salzmann, H. Glowatzki, R.L. Johnson, A. Vollmer, J.P. Rabe, N. Koch, Orientation-Dependent Ionization Energies and Interface Dipoles in Ordered Molecular Assemblies, Nat. Mater., 7 (2008) 326-332.
[195] O. Bauer, J. Ikonomov, C.H. Schmitz, M. Willenbockel, S. Soubatch, F.S. Tautz, M. Sokolowski, Adsorption of 3,4,9,10-Perylenetetracarboxylic Acid Dianhydride on the Cu3Au(111) Surface Studied by Normal-Incidence X-ray Standing Waves, J. Phys. Chem. C, 122 (2018) 10904-10917.
[196] P.J. Blowey, L.A. Rochford, D.A. Duncan, D.A. Warr, T.L. Lee, D.P. Woodruff, G. Costantini, Probing the Interplay Between Geometric and Electronic Structure in a Two-Dimensional K-TCNQ Charge Transfer Network, Faraday Discuss., 204 (2017) 97-110.

[197] X. Crispin, V. Geskin, A. Crispin, J. Cornil, R. Lazzaroni, W.R. Salaneck, J.-L. Brédas, Characterization of the Interface Dipole at Organic/Metal Interfaces, J. Am. Chem. Soc., 124 (2002) 8131-8141.
[198] A. Gerlach, T. Hosokai, S. Duhm, S. Kera, O.T. Hofmann, E. Zojer, J. Zegenhagen, F. Schreiber, Orientational Ordering of Nonplanar Phthalocyanines on Cu(111): Strength and Orientation of the Electric Dipole Moment, Phys. Rev. Lett., 106 (2011) 156102.
[199] A. Yang, A. Franco-Cañellas, M. Sato, B. Wang, R.-B. Wang, H. Koike, I. Salzmann, P.K. Thakur, T.-L. Lee, L. Liu, S. Kera, A. Gerlach, K. Kanai, J. Fan, F. Schreiber, S. Duhm, Nitrogen Substitution Impacts Organic-Metal Interface Energetics, Phys. Rev. B, 94 (2016) 155426.
[200] M.C. Lu, R.B. Wang, A. Yang, S. Duhm, Pentacene on Au(111), Ag(111) and Cu(111): From Physisorption to Chemisorption, J. Phys.: Condens. Matter, 28 (2016) 094005.
[201] A. Gerlach, F. Schreiber, S. Sellner, H. Dosch, I.A. Vartanyants, B.C.C. Cowie, T.-L. Lee, J. Zegenhagen, Adsorption-Induced Distortion of F16CuPc on Cu(111) and Ag(111): An X-ray Standing Wave Study, Phys. Rev. B, 71 (2005) 205425.
[202] Y.-Y. Lo, J.-H. Chang, G. Hoffmann, W.-B. Su, C.-I. Wu, C.-S. Chang, A Comparative Study on the Adsorption Behavior of Pentacene and Perfluoropentacene Molecules on Au(111) Surfaces, Jpn. J. Appl. Phys., 52 (2013) 101601.
[203] J.L. Yang, S. Schumann, R.A. Hatton, T.S. Jones, Copper hexadecafluorophthalocyanine (F16CuPc) as an electron accepting material in bilayer small molecule organic photovoltaic cells, Org. Electron., 11 (2010) 1399-1402.
[204] J.L. Yang, S. Schumann, T.S. Jones, Nanowire-array films of copper hexadecafluorophthalocyanine (F16CuPc) fabricated by templated growth, J. Mater. Chem., 21 (2011) 5812-5816.
[205] D.G. de Oteyza, A. El-Sayed, J.M. Garcia-Lastra, E. Goiri, T.N. Krauss, A. Turak, E. Barrena, H. Dosch, J. Zegenhagen, A. Rubio, Y. Wakayama, J.E. Ortega, Copper-Phthalocyanine Based Metal–Organic Interfaces: The Effect of Fluorination, the Substrate, and its Symmetry, J. Chem. Phys., 133 (2010) 214703.
[206] A. Franco-Cañellas, Q. Wang, K. Broch, B. Shen, A. Gerlach, H.F. Bettinger, S. Duhm, F. Schreiber, Resolving Intramolecular-Distortion Changes Induced by the Partial Fluorination of Pentacene Adsorbed on Cu(111), Phys. Rev. Mater., 2 (2018) 044002.
[207] J.N. O'Shea, A. Saywell, G. Magnano, L.M.A. Perdigão, C.J. Satterley, P.H. Beton, V.R. Dhanak, Adsorption of PTCDI on Au(111): Photoemission and scanning tunnelling microscopy, Surf. Sci., 603 (2009) 3094-3098.
[208] J. Hieulle, F. Silly, Localized Intermolecular Electronic Coupling in Two-Dimensional Self-Assembled 3,4,9,10-Perylenetetracarboxylic Diimide Nanoarchitectures, J. Mater. Chem. C, 1 (2013) 4536-4539.
[209] M. Klues, G. Witte, Crystalline packing in pentacene-like organic semiconductors, CrystEngComm, 20 (2018) 63-74.
[210] D. Käfer, M. El Helou, C. Gemel, G. Witte, Packing of Planar Organic Molecules: Interplay of van der Waals and Electrostatic Interaction, Cryst. Growth Des., 8 (2008) 3053-3057.
[211] H. Huang, S.L. Wong, W. Chen, A.T.S. Wee, LT-STM Studies on Substrate-Dependent Self-Assembly of Small Organic Molecules, J. Phys. D: Appl. Phys., 44 (2011) 464005.

[212] M. Mura, F. Silly, G.A.D. Briggs, M.R. Castell, L.N. Kantorovich, H-Bonding Supramolecular Assemblies of PTCDI Molecules on the Au(111) Surface, J. Phys. Chem. C, 113 (2009) 21840-21848.
[213] C. Wang, D. Niu, Y. Zhao, S. Wang, C. Qian, H. Huang, H. Xie, Y. Gao, Interface Energy-Level Alignment between Black Phosphorus and F16CuPc Molecular Films, J. Phys. Chem. C, 123 (2019) 10443-10450.
[214] F. Evangelista, V. Carravetta, G. Stefani, B. Jansik, M. Alagia, S. Stranges, A. Ruocco, Electronic Structure of Copper Phthalocyanine: An Experimental and Theoretical Study of Occupied and Unoccupied Levels, J. Chem. Phys. , 126 (2007) 124709.
[215] A. El-Sayed, D.J. Mowbray, J.M. García-Lastra, C. Rogero, E. Goiri, P. Borghetti, A. Turak, B.P. Doyle, M. Dell'Angela, L. Floreano, Y. Wakayama, A. Rubio, J.E. Ortega, D.G. de Oteyza, Supramolecular Environment-Dependent Electronic Properties of Metal–Organic Interfaces, J. Phys. Chem. C, 116 (2012) 4780-4785.
[216] D.G. de Oteyza, J.M. García-Lastra, M. Corso, B.P. Doyle, L. Floreano, A. Morgante, Y. Wakayama, A. Rubio, J.E. Ortega, Customized Electronic Coupling in Self-Assembled Donor–Acceptor Nanostructures, Adv. Funct. Mater., 19 (2009) 3567-3573.
[217] S.K.M. Henze, O. Bauer, T.L. Lee, M. Sokolowski, F.S. Tautz, Vertical Bonding Distances of PTCDA on Au(111) and Ag(111): Relation to the Bonding Type, Surf. Sci., 601 (2007) 1566-1573.
[218] H. Yamane, A. Gerlach, S. Duhm, Y. Tanaka, T. Hosokai, Y.Y. Mi, J. Zegenhagen, N. Koch, K. Seki, F. Schreiber, Site-specific geometric and electronic relaxations at organic-metal interfaces, Phys. Rev. Lett., 105 (2010) 046103.
[219] P.J. Blowey, R.J. Maurer, L.A. Rochford, D.A. Duncan, J.H. Kang, D.A. Warr, A.J. Ramadan, T.L. Lee, P.K. Thakur, G. Costantini, K. Reuter, D.P. Woodruff, The Structure of VOPc on Cu(111): Does V=O Point Up, or Down, or Both?, J. Phys. Chem. C, 123 (2019) 8101-8111.
[220] S. Kera, H. Fukagawa, T. Kataoka, S. Hosoumi, H. Yamane, N. Ueno, Spectroscopic Evidence of Strong π-π Interorbital Interaction in a Lead-Phthalocyanine Bilayer Film Attributed to the Dimer Nanostructure, Phys. Rev. B, 75 (2007) 121305.
[221] M.-S. Liao, J.D. Watts, M.-J. Huang, S.M. Gorun, T. Kar, S. Scheiner, Effects of Peripheral Substituents on the Electronic Structure and Properties of Unligated and Ligated Metal Phthalocyanines, Metal = Fe, Co, Zn, J. Chem. Theory Comput., 1 (2005) 1201-1210.
[222] W. Wu, L.A. Rochford, S. Felton, Z. Wu, J.L. Yang, S. Heutz, G. Aeppli, T.S. Jones, N.M. Harrison, A.J. Fisher, Magnetic properties of copper hexadecaphthalocyanine (F16CuPc) thin films and powders, J. Appl. Phys., 113 (2013) 013914.
[223] T. Graber, F. Forster, A. Schöll, F. Reinert, Experimental determination of the attenuation length of electrons in organic molecular solids: The example of PTCDA, Surf. Sci., 605 (2011) 878-882.
[224] Y. Ozawa, Y. Nakayama, S.i. Machida, H. Kinjo, H. Ishii, Maximum probing depth of low-energy photoelectrons in an amorphous organic semiconductor film, J. Electron Spectrosc. Relat. Phenom., 197 (2014) 17-21.
[225] N. Koch, Organic electronic devices and their functional interfaces, ChemPhysChem, 8 (2007) 1438-1455.
[226] P.S. Bagus, V. Staemmler, C. Wöll, Exchangelike Effects for Closed-Shell Adsorbates: Interface Dipole and Work Function, Phys. Rev. Lett., 89 (2002) 096104.

[227] N. Koch, A. Gerlach, S. Duhm, H. Glowatzki, G. Heimel, A. Vollmer, Y. Sakamoto, T. Suzuki, J. Zegenhagen, J.P. Rabe, F. Schreiber, Adsorption-Induced Intramolecular Dipole: Correlating Molecular Conformation and Interface Electronic Structure, J. Am. Chem. Soc., 130 (2008) 7300-7304.
[228] K. Toyoda, I. Hamada, K. Lee, S. Yanagisawa, Y. Morikawa, Density functional theoretical study of pentacene/noble metal interfaces with van der Waals corrections: vacuum level shifts and electronic structures, J. Chem. Phys. , 132 (2010) 134703.
[229] M.-K. Fung, Y.-Q. Li, L.-S. Liao, Tandem Organic Light-Emitting Diodes, Adv. Mater., 28 (2016) 10381-10408.
[230] R.S. Gurney, D.G. Lidzey, T. Wang, A Review of Non-Fullerene Polymer Solar Cells: From Device Physics to Morphology Control, Rep. Prog. Phys., 82 (2019) 036601.
[231] G. Schweicher, G. Garbay, R. Jouclas, F. Vibert, F. Devaux, Y.H. Geerts, Molecular Semiconductors for Logic Operations: Dead-End or Bright Future?, Adv. Mater., 32 (2020) 1905909.
[232] M. Fahlman, S. Fabiano, V. Gueskine, D. Simon, M. Berggren, X. Crispin, Interfaces in organic electronics, Nat. Rev. Mater., 4 (2019) 627-650.
[233] A. Mänz, A. A. Hauke, G. Witte, Copper Phthalocyanine as Contact Layers for Pentacene Films Grown on Coinage Metals, J. Phys. Chem. C, 122 (2018) 2165-2172.
[234] X. Wu, R. Jia, J. Pan, X. Zhang, J. Jie, Roles of Interfaces in the Ideality of Organic Field-Effect Transistors, Nanoscale Horiz., 5 (2020) 454-472.
[235] X. Zhang, Z. Wang, X. Zhou, Z. Wang, L. Huang, L. Chi, High-Performance Bottom-Contact Organic Thin-Film Transistors by Improving the Lateral Contact, Adv. Electron. Mater., 3 (2017) 1700128.
[236] R. Forker, M. Gruenewald, F. Sojka, J. Peuker, P. Mueller, C. Zwick, T. Huempfner, M. Meissner, T. Fritz, Fraternal Twins: Distinction Between PbPc and SnPc by Their Switching Behaviour in a Scanning Tunnelling Microscope, J. Phys.: Condens. Matter, 31 (2019) 134004.
[237] B. Stadtmüller, S. Schröder, F.C. Bocquet, C. Henneke, C. Kleimann, S. Soubatch, M. Willenbockel, B. Detlefs, J. Zegenhagen, T.-L. Lee, F.S. Tautz, C. Kumpf, Adsorption Height Alignment at Heteromolecular Hybrid Interfaces, Phys. Rev. B, 89 (2014) 161407.
[238] K. Broch, J. Dieterle, F. Branchi, N.J. Hestand, Y. Olivier, H. Tamura, C. Cruz, V.M. Nichols, A. Hinderhofer, D. Beljonne, F.C. Spano, G. Cerullo, C.J. Bardeen, F. Schreiber, Robust Singlet Fission in Pentacene Thin Films with Tuned Charge Transfer Interactions, Nat. Commun., 9 (2018) 954.
[239] J. Lee, P. Jadhav, P.D. Reusswig, S.R. Yost, N.J. Thompson, D.N. Congreve, E. Hontz, T. Van Voorhis, M.A. Baldo, Singlet Exciton Fission Photovoltaics, Acc. Chem. Res., 46 (2013) 1300-1311.
[240] L. Zhao, R.I. Kaiser, W. Lu, M. Ahmed, M.M. Evseev, E.K. Bashkirov, V.N. Azyazov, C. Tönshoff, F. Reicherter, H.F. Bettinger, A.M. Mebel, A Free-Radical Prompted Barrierless Gas-Phase Synthesis of Pentacene, Angew. Chem. Int. Ed., 59 (2020) 11334-11338.
[241] P. Hurdax, M. Hollerer, P. Puschnig, D. Lüftner, L. Egger, M.G. Ramsey, M. Sterrer, Controlling the Charge Transfer across Thin Dielectric Interlayers, Adv. Mater. Interfaces, 7 (2020) 2000592.

[242] F. Anger, J.O. Ossó, U. Heinemeyer, K. Broch, R. Scholz, A. Gerlach, F. Schreiber, Photoluminescence Spectroscopy of Pure Pentacene, Perfluoropentacene, and Mixed Thin Films, J. Chem. Phys., 136 (2012) 054701.
[243] J. Dieterle, K. Broch, A. Hinderhofer, H. Frank, J. Novák, A. Gerlach, T. Breuer, R. Banerjee, G. Witte, F. Schreiber, Structural Properties of Picene–Perfluoropentacene and Picene–Pentacene Blends: Superlattice Formation versus Limited Intermixing, J. Phys. Chem. C, 119 (2015) 26339-26347.
[244] J.-Q. Zhong, X. Qin, J.-L. Zhang, S. Kera, N. Ueno, A.T.S. Wee, J. Yang, W. Chen, Energy Level Realignment in Weakly Interacting Donor-Acceptor Binary Molecular Networks, ACS Nano, 8 (2014) 1699-1707.
[245] T. Breuer, G. Witte, Thermally Activated Intermixture in Pentacene-Perfluoropentacene Heterostructures, J. Chem. Phys. , 138 (2013) 114901.
[246] S. Duhm, I. Salzmann, G. Heimel, M. Oehzelt, A. Haase, R. L. Johnson, J. P. Rabe, N. Koch, Controlling Energy Level Offsets in Organic/Organic Heterostructures Using Intramolecular Polar Bonds, Appl. Phys. Lett., 94 (2009) 033304.
[247] Y. Nakayama, R. Tsuruta, N. Moriya, M. Hikasa, M. Meissner, T. Yamaguchi, Y. Mizuno, T. Suzuki, T. Koganezawa, T. Hosokai, T. Ueba, S. Kera, Widely Dispersed Intermolecular Valence Bands of Epitaxially Grown Perfluoropentacene on Pentacene Single Crystals, J. Phys. Chem. Lett., 10 (2019) 1312-1318.
[248] V.O. Kim, K. Broch, V. Belova, Y.S. Chen, A. Gerlach, F. Schreiber, H. Tamura, R.G. Della Valle, G. D'Avino, I. Salzmann, D. Beljonne, A. Rao, R. Friend, Singlet Exciton Fission via an Intermolecular Charge Transfer State in Coevaporated Pentacene-Perfluoropentacene Thin Films, J. Chem. Phys., 151 (2019) 164706.
[249] A. Rinn, T. Breuer, J. Wiegand, M. Beck, J. Hubner, R.C. Doring, M. Oestreich, W. Heimbrodt, G. Witte, S. Chatterjee, Interfacial Molecular Packing Determines Exciton Dynamics in Molecular Heterostructures: The Case of Pentacene-Perfluoropentacene, ACS Appl. Mater. Interfaces, 9 (2017) 42020-42028.
[250] H. Mönig, J. Sun, Y.M. Koroteev, G. Bihlmayer, J. Wells, E.V. Chulkov, K. Pohl, P. Hofmann, Structure of the (111) Surface of Bismuth: LEED Analysis and First-Principles Calculations, Phys. Rev. B, 72 (2005) 085410.
[251] N. Koch, Energy Levels at Interfaces Between Metals and Conjugated Organic Molecules, J. Phys.: Condens. Matter, 20 (2008) 184008.
[252] W.H. Soe, C. Manzano, A. De Sarkar, N. Chandrasekhar, C. Joachim, Direct Observation of Molecular Orbitals of Pentacene Physisorbed on Au(111) by Scanning Tunneling Microscope, Phys. Rev. Lett., 102 (2009) 176102.
[253] D. Käfer, L. Ruppel, G. Witte, Growth of pentacene on clean and modified gold surfaces, Phys. Rev. B, 75 (2007) 085309.
[254] J.H. Kang, X.Y. Zhu, Pi-stacked pentacene thin films grown on Au(111), Appl. Phys. Lett., 82 (2003) 3248-3250.
[255] H. Glowatzki, G. Heimel, A. Vollmer, S.L. Wong, H. Huang, W. Chen, A.T.S. Wee, J.P. Rabe, N. Koch, Impact of Fluorination on Initial Growth and Stability of Pentacene on Cu(111), J. Phys. Chem. C, 116 (2012) 7726-7734.
[256] J. Götzen, C.H. Schwalb, C. Schmidt, G. Mette, M. Marks, U. Hofer, G. Witte, Structural evolution of perfluoro-pentacene films on Ag(111): transition from 2D to 3D growth, Langmuir, 27 (2011) 993-999.

[257] C. Bürker, Adsorption geometry of π-conjugated organic molecules on metal surfaces studied with the X-ray standing wave technique, Eberhard Karls Universität Tübingen, 2014.
[258] K. Broch, U. Heinemeyer, A. Hinderhofer, F. Anger, R. Scholz, A. Gerlach, F. Schreiber, Optical Evidence for Intermolecular Coupling in Mixed Films of Pentacene and Perfluoropentacene, Phys. Rev. B, 83 (2011) 245307.
[259] G. D'Avino, L. Muccioli, F. Castet, C. Poelking, D. Andrienko, Z.G. Soos, J. Cornil, D. Beljonne, Electrostatic Phenomena in Organic Semiconductors: Fundamentals and Implications for Photovoltaics, J. Phys.: Condens. Matter, 28 (2016) 433002.
[260] I. Salzmann, S. Duhm, G. Heimel, M. Oehzelt, R. Kniprath, R. L. Johnson, J. P. Rabe, N. Koch, Tuning the Ionization Energy of Organic Semiconductor Films: The Role of Intramolecular Polar Bonds, J. Am. Chem. Soc, 130 (2008) 12870-12871.
[261] S. Kera, Y. Yabuuchi, H. Yamane, H. Setoyama, K.K. Okudaira, A. Kahn, N. Ueno, Impact of an interface dipole layer on molecular level alignment at an organic-conductor interface studied by ultraviolet photoemission spectroscopy, Phys. Rev. B, 70 (2004).
[262] S. Kera, H. Yamane, H. Honda, H. Fukagawa, K.K. Okudaira, N. Ueno, Photoelectron fine structures of uppermost valence band for well-characterized ClAl-phthalocyanine ultrathin film: UPS and MAES study, Surf. Sci., 566-568 (2004) 571-578.
[263] W. Zhao, E. Salomon, Q. Zhang, S. Barlow, S.R. Marder, A. Kahn, Substrate-dependent electronic structure of an organic heterojunction, Phys. Rev. B, 77 (2008).
[264] C. Zhao, W. Wang, S. Yin, Y. Ma, Theoretical investigation on electronic, optical, and charge transport properties of 7,8,15,16-tetraazaterrylene and its derivatives with electron-attracting substituents, New J. Chem., 37 (2013).
[265] B. Stadtmüller, S. Schröder, C. Kumpf, Heteromolecular metal–organic interfaces: Electronic and structural fingerprints of chemical bonding, J. Electron. Spectrosc. Relat. Phenom., 204 (2015) 80-91.
[266] P. Beyer, D. Pham, C. Peter, N. Koch, E. Meister, W. Brütting, L. Grubert, S. Hecht, D. Nabok, C. Cocchi, C. Draxl, A. Opitz, State-of-Matter-Dependent Charge-Transfer Interactions between Planar Molecules for Doping Applications, Chem. Mater., 31 (2019) 1237-1249.
[267] P.S. Deimel, P. Feulner, J.V. Barth, F. Allegretti, Spatial decoupling of macrocyclic metal–organic complexes from a metal support: a 4-fluorothiophenol self-assembled monolayer as a thermally removable spacer, Phys. Chem. Chem. Phys., 21 (2019) 10992-11003.
[268] L. Fernández, S. Thussing, A. Manz, J. Sundermeyer, G. Witte, P. Jakob, The discrete nature of inhomogeneity: the initial stages and local configurations of TiOPc during bilayer growth on Ag(111), Phys. Chem. Chem. Phys., 19 (2017) 2495-2502.
[269] O.T. Hofmann, G.M. Rangger, E. Zojer, Reducing the Metal Work Function beyond Pauli Pushback: A Computational Investigation of Tetrathiafulvalene and Viologen on Coinage Metal Surfaces, J. Phys. Chem. C, 112 (2008) 20357-20365.
[270] H. Fukagawa, S. Hosoumi, H. Yamane, S. Kera, N. Ueno, Dielectric properties of polar-phthalocyanine monolayer systems with repulsive dipole interaction, Phys. Rev. B, 83 (2011).
[271] A. Terentjevs, M.P. Steele, M.L. Blumenfeld, N. Ilyas, L.L. Kelly, E. Fabiano, O.L.A. Monti, F. Della Sala, Interfacial Electronic Structure of the Dipolar Vanadyl

Naphthalocyanine on Au(111): “Push-Back” vs Dipolar Effects, J. Phys. Chem. C, 115 (2011) 21128-21138.
[272] A. Lerch, L. Fernandez, M. Ilyn, M. Gastaldo, M. Paradinas, M.A. Valbuena, A. Mugarza, A.B.M. Ibrahim, J. Sundermeyer, U. Höfer, F. Schiller, Electronic Structure of Titanylphthalocyanine Layers on Ag(111), J. Phys. Chem. C, 121 (2017) 25353-25363.
[273] A. Gerlach, S. Sellner, F. Schreiber, N. Koch, J. Zegenhagen, Substrate-dependent bonding distances of PTCDA: A comparative x-ray standing-wave study on Cu(111) and Ag(111), Phys. Rev. B, 75 (2007) 045401.
[274] L. Chen, H. Li, A. Thye Shen Wee, Nonlocal Chemical Reactivity at OrganicMetal Interfaces, ACS Nano, 3 (2009).
[275] H. Huang, W. Chen, A. Thye Shen Wee, Low-Temperature Scanning Tunneling Microscopy Investigation of Epitaxial Growth of F16CuPc Thin Films on Ag(111), J. Phys. Chem. C, 112 (2008).
[276] M. Kothe, F. Widdascheck, G. Witte, Titanylphthalocyanine Films on Ag(111): An Epitaxial Metal/Organic Heterosystem with an Exceptional Smooth Surface, J. Phys. Chem. C, 123 (2019) 6097-6106.
[277] Q. Wang, M.-T. Chen, A. Franco-Cañellas, B. Shen, T. Geiger, H. F. Bettinger, F. Schreiber, I. Salzmann, A. Gerlach, S. Duhm, Impact of Fluorination on Interface Energetics and Growth of Pentacene on Ag(111), Beilstein J. Nanotechnol., 11 (2020) 1361-1370.
[278] V. Coropceanu, M. Malagoli, D.A. da Silva Filho, N.E. Gruhn, T.G. Bill, J.L. Brédas, Hole- and Electron-Vibrational Couplings in Oligoacene Crystals: Intramolecular Contributions, Phys. Rev. Lett., 89 (2002) 275503.
[279] M.C.R. Delgado, K.R. Pigg, D.A. da Silva Filho, N.E. Gruhn, Y. Sakamoto, T. Suzuki, R.M. Osuna, J. Casado, V. Hernández, J.T.L. Navarrete, N.G. Martinelli, J. Cornil, R.S. Sánchez-Carrera, V. Coropceanu, J.-L. Brédas, Impact of Perfluorination on the Charge-Transport Parameters of Oligoacene Crystals, J. Am. Chem. Soc., 131 (2009) 1502-1512.
[280] S.-A. Savu, G. Biddau, L. Pardini, R. Bula, H.F. Bettinger, C. Draxl, T. Chassé, M.B. Casu, Fingerprint of Fractional Charge Transfer at the Metal/Organic Interface, J. Phys. Chem. C, 119 (2015) 12538-12544.
[281] S. Duhm, C. Bürker, J. Niederhausen, I. Salzmann, T. Hosokai, J. Duvernay, S. Kera, F. Schreiber, N. Koch, N. Ueno, A. Gerlach, Pentacene on Ag(111): correlation of bonding distance with intermolecular interaction and order, ACS Appl. Mater. Interfaces, 5 (2013) 9377-9381.
[282] S. Duhm, S. Hosoumi, I. Salzmann, A. Gerlach, M. Oehzelt, B. Wedl, T.-L. Lee, F. Schreiber, N. Koch, N. Ueno, S. Kera, Influence of Intramolecular Polar Bonds on Interface Energetics in Perfluoro-pentacene on Ag(111), Phys. Rev. B, 81 (2010) 045418
[283] A. Kahn, N. Koch, W. Gao, Electronic structure and electrical properties of interfaces between metals and π-conjugated molecular films, J. Polym. Sci. B Polym. Phys., 41 (2003) 2529-2548.
[284] I. Salzmann, A. Moser, M. Oehzelt, T. Breuer, X. Feng, Z. Juang, D. Nabok, R. G. Della Valle, S. Duhm, G. Heimel, A. Brillante, E. Venuti, I. Bilotti, C. Christodoulou, J. Frisch, P. Puschnig, C. Draxl, G. Witte, K. Müllen, N. Koch, Epitaxial Growth of π-Stacked Perfluoropentacene on Graphene-Coated Quartz, ACS Nano, 6 (2012) 10874-10883.

LIST OF PUBLICATIONS

[1] **Qi Wang**, Jiacheng Yang, Steffen Duhm, Alexander Gerlach and Frank Schreiber. Titanyl-phthalocyanine Based Trilayer: Organic-Organic Heterostructures. In preparation.

[2] **Qi Wang**, Jiacheng Yang, Antoni Franco-Cañellas, Christoph Bürker, Pierre Dombrowski, Felix Widdasckeck, Tobias Breuer, Gregor Witte, Alexander Gerlach, Steffen Duhm and Frank Schreiber. Pentacene/Perfluoropentacene Bilayers on Au(111) and Cu(111): Impact of Organic-Metal Coupling Strength on Vertical Molecular Order. Submitted.

[3] Jiacheng Yang, **Qi Wang**, Shanshan Wan, Di Wu, Mengting Chen, Stepan Kashtanov and Steffen Duhm. Photoelectron spectroscopy reveals molecular diffusion through physisorbed template layers on Au(111). In preparation.

[4] **Qi Wang**, Meng-Ting Chen, Antoni Franco-Cañellas, Bin Shen, Thomas Geiger, Holger F. Bettinger, Frank Schreiber, Alexander Gerlach and Steffen Duhm. Impact of Fluorination on Interface Energetics and Growth of Pentacene on Ag(111). *Beilstein Journal of Nanotechnology.* 2020, **11**, 1361-1370.

[5] **Qi Wang**, Antoni Franco-Cañellas, Jiacheng Yang, Julian Hausch, Samuel Struzek, Mengting Chen, Pardeep Kumar Thakur, Alexander Gerlach, Steffen Duhm, and Frank Schreiber. Heteromolecular Bilayers on a Weakly Interacting Substrate: Physisorptive Bonding and Molecular Distortions of Copper-hexadecafluorophthalocyanine. *ACS Applied Materials & Interfaces,* 2020, **12**, 14542-14551.

[6] **Qi Wang**, Antoni Franco-Cañellas, Penghui Ji, Christoph Bürker, Rong-Bin Wang, Katharina Broch, Pardeep Kumar Thakur, Tien-Lin Lee, Haiming Zhang, Alexander Gerlach, Lifeng Chi, Steffen Duhm and Frank Schreiber. Bilayer Formation vs. Molecular Exchange in Organic Heterostructures: Strong Impact of Subtle Changes in Molecular Structure. *The Journal of Physical Chemistry C*, 2018, **122**, 9480-9490.

[7] Nabi Aghdassi, **Qi Wang**, Ru-Ru Ji, Bin Wang, Jian Fan, and Steffen Duhm. Ultraviolet Photoelectron Spectroscopy Reveals Energy-Band Dispersion for π-stacked 7,8,15,16-Tetraazaterrylene Thin Films in a Donor-Acceptor Bulk Heterojunction. *Nanotechnology*, 2018, **29**, 194002.

[8] Antoni Franco-Cañellas, **Qi Wang**, Katharina Broch, Bin Shen, Alexander Gerlach, Holger. F. Bettinger, Steffen Duhm, and Frank Schreiber. Resolving Intramolecular-Distortion Changes Induced by the Partial Flurination of Pentacene Adsorbed on Cu(111). *Physical Review Materials*, 2018, **2**, 044002.

[9] Antoni Franco-Cañellas, **Qi Wang**, Katharina Broch, David A. Duncan, Pardeep Kumar Thakur, Lijia Liu, Satoshi Kera, Alexander Gerlach, Steffen Duhm, and Frank Schreiber. Fingerprints of Lateral and Vertical Order in Core-level Spectra of Organic Monolayers on Coinage Metals. *Physical Review Materials*, 2017, **1**(1):013001.

[10] **Qi Wang**, Qian Xin, Rong-Bin Wang, Martin Oehzelt, Nobuo Ueno, Satoshi Kera, and Steffen Duhm. Picene Thin Films on Metal Surfaces: Impact of Molecular Shape on Interfacial Coupling. *Physics Status Solidi: Rapid Research Letters*, 2017, **11**(5)1700012.

[11] Rongbin Wang, Chen Wu, Yun Hu, Jitao Li, Pengfei Shen, **Qi Wang**, Liangsheng Liao, Lijia Liu, and Steffen Duhm. CH3NH3PbI3-xClx under Different Fabrication Strategies: Electronic Structures and Energy-Level Alignment with an Organic Hole Transport Material. *ACS Applied Materials & Interfaces*, 2017, **9**, 7859-7865.

[12] Ru-Ru Ji, **Qi Wang**, Jia-Xin Hu and Steffen Duhm. Impact of Room Temperature on Pentacene Thin Film Growth and Electronic Structure. *Canadian Journal of Chemistry*, 2017, **95**, 1130-1134.

[13] Yanfeng Liu, Nabi Aghdassi, **Qi Wang**, Steffen Duhm, Yi Zhou, Bo Song. Solvent-Resistant ITO Work Function Tuning by an Acridine Derivative Enables High Performance Inverted Polymer Solar Cells. *Organic Electronics*, 2016, **35**, 6-11.

DEUTSCHE ZUSAMMENFASSUNG

Organische konjugierte Moleküle sind in den letzten Jahren zu einem der grundlegenden Materialien in der Halbleitergemeinschaft geworden. Bauelemente aus organischen Halbleitermaterialien (engl. *organic semiconductors,* OSC), wie z.B. organische Leuchtdioden (engl. *organic light-emmited diode,* OLED), organische Photovoltaikzellen (OPV) und organische Feldeffekt-transistoren (OFET), weisen im Vergleich zu anorganischen Pendants vergleichbare Wirkungsgrade und darüber hinaus überlegene Eigenschaften in Bezug auf geringes Gewicht, mechanische Flexibilität und niedrige Kosten auf. Diese Eigenschaften führen zu einem sehr großen Anwendungspotenzial für OSC-Bauelemente auf dem kommerziellen Markt. Um die Effizienz dieser Bauelemente weiter zu fördern, ist ein umfassendes Verständnis der Heteroübergänge zwischen verschiedenen OSC-Materialien von der Kristallstruktur bis zur elektronischen Struktur bestehen von entscheidender Bedeutung, da diese unvermeidlichen Übergänge eine entscheidende Rolle im Ladungsträgertransport spielen.

Um Informationen über die Struktureigenschaft (molekulare Adsorptionshöhe und Stapelanordnung) und über die elektronische Struktur von Heterostrukturen zu erhalten, werden in dieser Arbeit stehende Röntgenwellen (engl. *X-ray standing wave,* XSW), die niederenergetische Elektronenbeugung (engl. *Low-energy electron diffraction,* LEED), die hochauflösende Röntgen-Photoelektronenspektroskopie (engl. *High-resolution X-ray photoelectron spectroscopy,* HR-XPS) und die Ultraviolette Photoelektronen-spektroskopie (UPS) eingesetzt. Münzmetalle werden aufgrund ihrer guten Leitfähigkeit häufig als Elektroden an realen Geräten verwendet. Für prototypische Studien werden hier atomar reine Münzmetallkristalle verwendet, da ihre Oberflächen flach und geordnet sind. Die chemische Aktivität der Oberfläche von inertem [Au (111)] zu aktivem [Cu (111)] ändern kann sich jedoch ändern, was die Kopplungsstärke mit den nachfolgend abgeschiedenen OSC-Molekülen beeinflussen kann. Zu Beginn dieser Arbeit werden von Kupfer-Hexadecafluorphthalocyanin ($F_{16}CuPc$) abgeleitete Doppelschichten mit Zwischenschichten aus 5,7,12,14-Pentacentetron (P4O) und Perylen-3,4,9,10-

Tetracarboxyl-Diimin (PTCDI) auf Au(111) aufgebaut, um den Einfluss der Organisch-Metall-Wechselwirkungsstärke zu untersuchen. Es wurde festgestellt, dass die Doppelschichten gut geformt sind, und dass F_{16}CuPc Vergleich zu seiner Monoschichtstruktur eine umgekehrte intramolekulare Verzerrung aufweist. Zweitens wird ein Donor-Akzeptor-Gegenstück (D-A), Pentacen-Perfluorpentacen (PEN-PFP), eingesetzt, um die Doppelschicht-Bildung auf dem gleichen Substrat weiter zu untersuchen. Es hat sich jedoch gezeigt, dass die molekulare Mischung trotz des Substrats mit schwacher Wechselwirkung auftritt. Schließlich wurde eine kompliziertere Heterostruktur, die Dreifachschicht, auf Ag(111) eingesetzt. Diese bestehend aus einer Doppelschicht Titanylphthalocyanin (TiOPc) mit verschwindendem Nettodipol und einer darauf adsorbierten dritten organischen Molekularschicht (F_{16}CuPc, P4O). Es wurde weder eine intramolekulare Verzerrung noch ein molekularer Austausch beobachtet, was bedeutet, dass eine ideale organisch-organische Grenzfläche existiert. Durch den Einsatz der leistungsstarken Techniken XSW, HR-XPS und UPS haben wir Zugang zu den elektronischen und strukturellen Informationen mehrerer Heterostrukturen auf den Münzmetallsubstraten erhalten, was sowohl angewandte als auch Grundlagenforschungen auf dem Gebiet der OSC anregen und fördern könnte.

Schlüsselwörter: Heterostruktur, Adsorptionseigenschaft, elektronische Charakteristik, Stehende Röntgenwelle, Röntgen-Photoelektronenspektroskopie, Ultraviolett-Photoelektronenspektroskopie

ACKNOWLEDGEMENTS

I am using this opportunity to express my gratitude to everyone who supported me throughout these three years of my PhD study.

Firstly, I would like to thank Prof. Frank Schreiber for giving me the opportunity to do my PhD in his group, for his inspiring supervision and trust. I also appreciate PD Dr. Fajun Zhang for agreeing to serve as the second reporter.

I must acknowledge China Scholarship Council for the financial support to accomplish my study abroad. Precious thanks to the materially and spiritually care during COVID-19 period from Chinese Consulate in Frankfurt am Main and Chinese Student Union in Tübingen.

I am also grateful to thank Prof. Steffen Duhm, who was my master supervisor and is the close collaborator to generously share his knowledge and equipment. Thanks to our Tübingen collaborators, Prof. Holger Bettinger and J. Prof. Katharina Broch for giving me the opportunity to work and learn from them.

Dr. Alexander Gerlach deserves my special thanks, for his precious and patient help and advice, without him this work would not have been the same.

The experiments at the beamline I09 of the Diamond Light Source have been an indispensable part of this work and has become possible by the excellent facilities and the support of its staff, especially Dr. Tien-Lin Lee, Dr. Pardeep Kumar Thakur and Dr. David A. Duncan.

Also, very warm thanks to Dr. Antoni Franco-Cañellas, who enormously helped me at the beginning, and continuously provide revisions of my work. I would also thank Jiacheng Yang, in Duhm's group, for his help with the PES measurements. Great thanks to all the proofreaders, especially Dr. Giuliano Duva, Berthold Reisz, Alessandro Greco, Jan Hagenlocher and Matthias Zwadlo for the valuable comments.

The coming thanks to my colleagues in the Soft Matter group, thanks to Dr. Alexander Hinderhofer, Clemen Zeiser, Samuel Struzek, Julian Hausch, and Frau Maurer and Frau Roetschke for their administrative work during the last three years. Thanks to Bernd Hofferberth for the technical support in the local lab. The last thanks goes to Dr. R.-B. Wang and to my family and friends, for their love and care on my way.